UNIVERSITÀ DEGLI STUDI DELLA TUSCIA

Dipartimento di Economia, Ingegneria, Società e Impresa

Ph.D. Program

Engineering for energy and environment

XXXV Cycle

PhD Thesis

Design and improvement of thermo-structural performances of ECRH mirrors of different fusion facilities: DTT, DEMO and ST40

S.S.D. ING-IND/31 ING-IND/14

Ph.D. Candidate
Dott.ssa Alessandra Salvitti

Ph.D. Coordinator
Prof. Ing. Andrea Luigi Facci

Supervisor
Prof. Ing. Giuseppe Calabrò

Co-supervisor
Prof. Ing. Pierluigi Fanelli

Academic Year 2022-2023

Contents

Abstract **2**

1 Introduction **5**
1.1 Global Energy 5
1.2 Nuclear Fusion 7
1.3 Status and Roadmap 9
1.4 Thesis objective 11
1.5 Disseminations of research results 12

2 ECRH and its Mirrors **15**
2.1 Additional Heating Systems 15
2.2 ECRH and its MIRRORS 16
2.2.1 ECRH Mirrors 17

3 Technical approach to FEM analyses **19**
3.1 FEM Tools 19
3.1.1 FLUID116 20
3.2 Heat exchange assumptions 21
3.3 Thermal Load 22

4 Divertor Tokamak Test facility **25**
4.1 DTT ECRH 27
4.1.1 DTT Transmission Line 28
4.1.2 DTT Launcher system 28

5 DTT Launcher mirrors **31**
5.1 Preliminary M2 mirror design 31
5.1.1 Requirements 32
5.1.2 Data and Hypotheses 33

5.1.3 FE Models 36
5.1.4 Geometric configuration analysis 38
5.1.5 Dependency to water parameters analysis 39
5.1.6 Results 40
5.1.7 Dependency to water parameters analysis results . . 42
5.1.8 Preliminary M2 mirror design: first considerations . 45
5.2 M2 mirror design update and preliminary M1 mirror design 47
5.2.1 Assumptions and requirements 47
5.2.2 Geometry of the mirrors 48
5.2.3 Loads 49
5.2.4 Input and Achieved Results 51
5.2.5 Definition of the cooling circuit hydraulic parameters 54
5.2.6 Comparison of Unitus - PoliTO thermal results . . . 55
5.2.7 Preliminary structural analysis for mirror M2 57
5.2.8 M1 and M2 mirrors design: intermediate considerations 60
5.3 M1 mirror design improvement 61
5.3.1 Starting assumptions 62
5.3.2 CAD modification and proposals 62
5.3.3 Thermal analyses 64
5.3.4 Structural results 65
5.3.5 Complete final analysis 68
5.3.6 M1 mirror design improvement: final considerations 69
5.4 Summary and conclusions about DTT Launcher mirrors . . 70

6 DTT MBTL mirrors 73
6.1 MBTL mirrors "Step 0" 74
6.2 MBTL Parabolic mirror design 75
6.2.1 MBTL Parabolic mirror assumptions 76
6.2.2 Numerical modelling 79
6.2.3 Definition of different mirror models 79
6.2.4 Thermo-structural simulations, inputs, and results . 83
6.2.5 Optimization of the mirror performance 93
6.2.6 Non-simultaneous beams 101
6.2.7 MBTL parabolic mirror: summary and first considerations 102
6.3 Update of thermal conditions for Parabolic mirror 103
6.4 MBTL Flat mirrors design 106

6.4.1 Geometry of flat mirrors . . . 107
6.4.2 Thermal load of flat mirrors . . . 110
6.4.3 Thermo-structural analyses of Flat mirrors . . . 110
6.5 Update of thermal load conditions for MBTL mirrors . . . 114
6.6 Design of MBTL mirrors external to the corridor . . . 117
6.6.1 CAD models of the external mirrors . . . 117
6.6.2 Thermal loads of the external mirrors . . . 119
6.6.3 Thermo-structural analyses of the external mirrors . . . 120
6.7 Summary of the MBTL mirror design . . . 125

7 DEMO 127
7.1 DEMO ECRH system . . . 128
7.2 DEMO activity . . . 129
7.3 DEMO ECRH Focusing mirror . . . 130
7.3.1 First structural analysis of the mirror . . . 134
7.3.2 Enclosure for a couple of mirrors . . . 136
7.3.3 Modification of the focusing mirror . . . 137
7.4 Proposals for mirror supporting structure . . . 139
7.4.1 Supporting structure with circular rails . . . 140
7.4.2 Supporting structure with spherical joint . . . 144
7.4.3 Supporting structure with cardan joint . . . 149
7.5 Enclosure with a couple of mirrors . . . 150
7.6 Preliminary thermo-structural analyses of the parabolic mirror . . . 153
7.6.1 FEM Model . . . 153
7.6.2 Thermal Load . . . 153
7.6.3 Steady-state thermal analysis . . . 154
7.6.4 Transient thermal analysis . . . 157
7.6.5 Static structural analysis . . . 160
7.7 Summary of the work on the focusing mirror of the MBTL of DEMO . . . 163

8 ST40 167
8.1 ST40 HFS launcher mirror . . . 168
8.1.1 Transient thermal analysis . . . 170
8.2 Summary for the work on ST40 HFS launcher mirror . . . 175

9 Summary and conclusions 177

Bibliography and sitography **181**

Abstract

In the field of nuclear fusion research, many challenges have yet to be overcome and many others are on the way. Among these, one concerns plasma heating at very high temperatures. In this context, Electron Cyclotron Resonance Heating (ECRH) plays an important role, being one of the first choices among additional heating systems. It generates microwave beams launched directly into the plasma to heat it up. Mirrors are one of the main components of the system, necessary for the transmission and reflection of the microwave beams. Since the reflection is not perfect, a small part of the power transported by the beams is absorbed by the mirror, raising its temperature. This produces deformations of the mirror, causing inefficiencies in its optical performance, resulting in plasma power losses. It is therefore necessary to design mirrors preserving their optical characteristics as much as possible, reducing temperatures and thus deformations. The possibility of applying already known solutions, studying the effects of alternative design choices, cooling systems, materials, geometries, adapting them to new requirements, gave rise to this thesis. It aims to make a contribution to research by finding suitable solutions for the mirrors of the next-generation tokamaks. The technical approach used foresees the definition of CAD models and FEM simulations, using tools based on well-known thermal and structural analysis methodologies. These analyses guide the choices and direct the study that lays the foundations for tomorrow's developments. The methodology is applied to different mirror topologies and tokamaks such as DTT, DEMO and ST40. DTT represents the main part of the work with the mirrors of the launcher and the transmission line. In DEMO, in addition to the preliminary design of the mirror, various mechanical solutions are proposed for the support structures. Finally, in ST40, a preliminary study of the thermal behaviour of a launcher mirror of its new ECRH is carried out.

Chapter 1

Introduction

1.1 Global Energy

The energy is one of the main cornerstone of the world. Its development changed the perspective of the human beings, above all starting from the first industrial revolution. As visible from the graph in fig. 1.1 from 1800 to present days the consumption of the primary energy sources has completely changed, with a vertiginous increase from 1950.

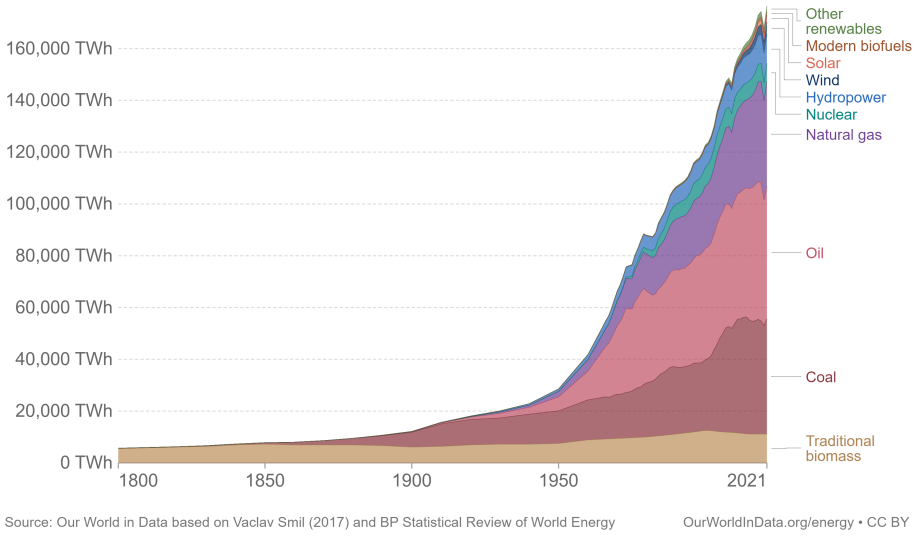

Figure 1.1: *Global primary energy consumption by source (Source: Our World in Data) [1].*

The traditional sources, as coal, oil and gases are still the energy base,

but renewable energy sources, as hydropower, wind, solar, biofuels and nuclear, started to be essential for the modern world. At 2019 $\sim$ 19% of the final energy consumed was Electricity, its production by different sources can be seen in fig. 1.2 from 1980 to 2021 [2].

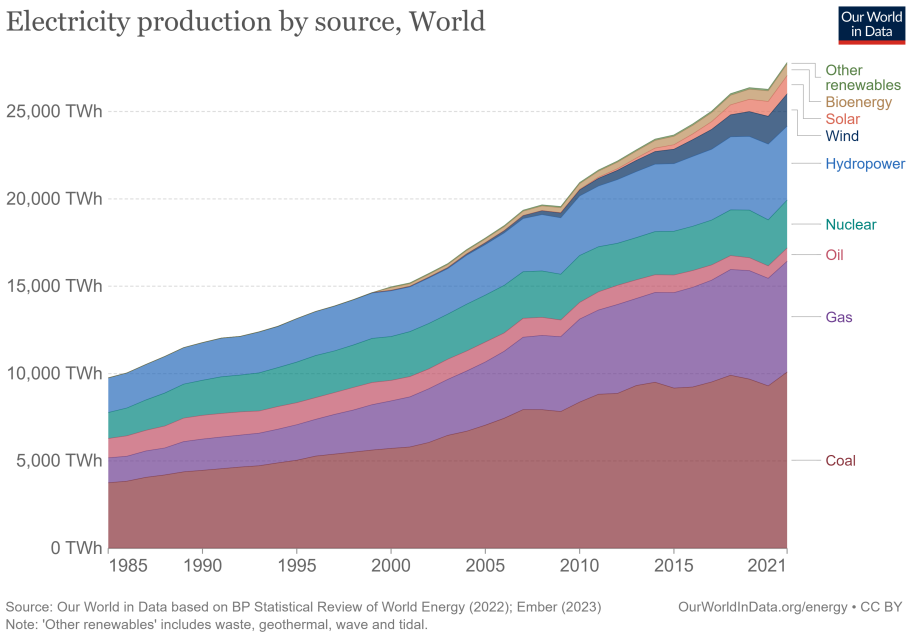

Figure 1.2: *Electricity production by source, World [1].*

Looking to the future, electricity consumption is expected to increase fast, to almost double by 2050 [2], without considering events that can accelerate this phenomenon, or changing the sort of the natural projections. For example the energy crisis of 2022 born after the start of the Russian-Ukrainian conflict.

The increment of the industrialized area leads to the increment of the demand of energy production, with the necessity of a ready response by the sources, that is impossible to have. About the 80% of the energy used on earth comes from fossil fuels. It is known that their reserves are exhaustible, finite and limited, going to exhaust in decades (in 150 years about one half of the available resources will have been exploited) [3].

The exploitation of the fossil fuels gave birth to another problem, cen-

tral now in public discussion: the greenhouse gas emission (in particular CO_2), main cause of the climate changes and the related problems of the global warming, increment of precipitations, glacier retreat etc. So, the world wants to move forward another era. The Paris Agreement's goal is to keep the increase of the global average temperature "to well below 2°C above pre-industrial levels and to pursue efforts to limit the temperature increase to 1.5°C" [4]. The Europe is moving in this direction proposing the "European Green Deal" with the objective to reduce the gas emission by 55% by 2030, investing in renewable energy for the electricity production.

The combined issues of increasing supply while decreasing emissions brought the whole world to develop research and technologies for renewable sources of energy to take the place of fossil fuels [3, 5]. So many alternative energy sources were born, because the solution to the present problems isn't only one. Unfortunately the current alternative sources (solar, wind, geothermal, biofuel) alone cannot completely replace fossil fuels due to limited energy density. For this reason, alternative sources of energy, clean, sustainable and able to sustain the energy demand growth, need to be found. In this context one of the best candidates seems to be the Nuclear Fusion [3, 6].

1.2 Nuclear Fusion

The Sun is somehow the engine that has allowed the development and exploitation of fossil fuels, hydropower, wind or solar energy [7]. In the same way, it is the core of an alternative energy source: the Nuclear Fusion.
The nuclear fusion is the thermonuclear reaction powers the stars, and the Sun. It consists in the union of two light nuclei in a heavier one. The primitive nuclei must win the repulsive electromagnetic force crashing with very elevated kinetic energy and react through strong interaction, to form an unique heavier nucleus, with bigger atomic number.
In these reactions the mass of the products is minor than the mass of the reagents and this is manifested as the release of large amounts of energy. The $0,7\%$ of the mass is transformed in energy, according to Einstein's equation.

Into the stars the temperature and the density of the matter are so elevated to produce a lot of reactions of fusion. The Hydrogen (H) is the main component of the stellar matter and basic element of the process. It is converted into Helium (He), releasing a huge amount of thermal energy, electromagnetic radiation, particle flow (solar wind) and neutrinos.
Thanks to the new technologies, scientists aim to reproduce a little sun on Earth, doing fusion between a nucleus of deuterium ${}^{2}_{1}H$ and a nucleus of tritium ${}^{3}_{1}H$, producing a nucleus of helium ${}^{4}_{2}He$ and a neutron, releasing $17,6MeV$ of energy in the form of kinetic energy of the products: 3.5 MeV and 14.1 MeV respectively for helium and neutron.
Nuclear fusion has enormous potential: from 100 mg of deuterium (contained in about 3 litres of sea water) plus 150 mg of tritium, it is possible to obtain the same energy produced by about 1100 litres of oil (approximately 7 barrels of oil) [3].

First two main difficulties in the feasibility of the fusion are:

- the realization of the state of *"plasma"* with temperature of the order of 10^8K;
- the confinement of the particles of plasma at a density high enough to permit many collisions, essential for the ignition.

In the stars, the plasma is confined by the intense gravitational field generated by its mass. This is not possible in the laboratory, but the need remains for the plasma to be well confined, so that the nuclear reactions can sustain the fusion process. The confinement structure must be kept at reasonably low temperatures unlike the plasma which must be brought to temperatures of hundreds of millions of degrees. Under such conditions the contact would lead to a cooling of the plasma itself and the container walls would be damaged.
For this purpose, the two research lines most pursued are magnetic confinement and inertial confinement.
Magnetic confinement uses strong magnetic fields able to constrain the motion of the charged particles of the plasma to be confined in a limited region. In magnetic confinement machines, the field is generated by flowing electrical currents in coils located around the plasma confinement zone, namely around the chamber containing plasma. An advantageous solution for limiting losses due to the dynamics of the particles exploits a

toroidal-shaped container that has no open ends: inside it the magnetic field lines are bounded to closed surfaces inside the torus. Examples of this configuration are the tokamak and the stellarator [8]. Now the Tokamak is considered as one of the most promising device to generate energy through nuclear fusion.

But, why may **nuclear fusion** look like a **big alternative** to traditional energy sources?

Fusion has got many benefits [6] that lay it among the new frontiers for the energy: it doesn't produce carbon dioxide and it can be a sustainable energy source to complement renewable ones.
The fusion fuel is abundant. The tritium can be produced from lithium, a metal ubiquitous in the Earth's crust and in the seawater. Instead, for the deuterium it is foreseen to be available for tens of thousands of years, because it is dissolved in natural water. This huge quantity can ensure from the risk of shortages or monopoly of supply.
Besides, a fusion power plant is safe: less than a gramme of fuel leads to the ignition of the plasma, which, in case of problems, errors or damages rapidly extinguishes itself.
A factor of risk concerns the radioactive materials: tritium, which has a short half-life of 12 years and neutrons which, impacting against the matter, can activate it. The positive aspect is that the resulting radioactive by-products have half-lives of tens of years rather than thousands of years, as for fission. Furthermore these activated materials remain confined into the machine where the human presence is forbidden.

1.3 Status and Roadmap

In 2012 the European Commission requested EFDA (European Fusion Development Agreement) to prepare a technical roadmap to fusion electricity by 2050 [9]. EUROfusion, [10], a joint research programme, promoted by European Commission Ue and by European research laboratories for the nuclear fusion, published the roadmap update on November 2018: "The European Fusion Roadmap outlines the research and development required to provide the basis for an electricity-generating fusion power plant" [6].

The roadmap to fusion energy was developed to have a structured plan that put together all the requirements coming from the fusion research world. It is composed of three main milestones: ITER (International Thermonuclear Experimental Reactor), DEMO (DEMOnstration Power Reactor) and a fusion materials testing facility (IFMIF-DONES).
ITER project is a worldwide effort, which will demonstrate the scientific and technological feasibility of fusion on Earth. Its main aim is the generation of ten times more fusion power than the power injected to feed the fusion process. The results, obtained from this machine, will be important inputs to refine the DEMO design that goes on in parallel with ITER. DEMO will demonstrate first electricity production by fusion. But compared to ITER, it has two additional goals: electricity production and fuel self-sufficiency. A following chapter will be dedicated to it.

The roadmap covers three periods:

- First period (up to 2030): "Build ITER and Broader Approach projects; Secure ITER success; Lay the foundation of DEMO".
- Second period (2031-2040): "Exploit ITER up to its maximum performance and prepare DEMO construction".
- Third period (beyond 2040): "Complete the ITER exploitation; IFMIF upgrade; Construct and operate DEMO; Lay the foundation for fusion power plants".

The realisation of fusion energy has to face a number of challenges, so EUROfusion defined eight different missions to guide the long-term programme concerning the issues of plasma, heat-exhaust systems, materials, tritium self-sufficiency, safety, integrated systems, cost and stellarator [6]. Inside the mission n.2, to increase the knowledge about the heat exhaust issue, the DTT project was born with the support of Italian government, companies, research centres and universities, including Tuscia University [6]. Main part of this thesis will be concentrated on this facility, so it will be well explained in the following chapters.

Nowadays not only research centres work on nuclear fusion, but private companies are increasingly investing in this field, promoting new alternative compact and fast solutions. One of them, Tokamak Energy Ltd, based in UK, has built a spherical tokamak ST40, banking on the advantages

of this type of facility: compactness, high performance, optimal confinement and high vertical stability for the plasma [11]. This machine will be treated at the end of this thesis.

1.4 Thesis objective

One of the main challenges of nuclear fusion is to reach very high temperature in the plasma. Among the different systems deployed to this purpose there is the Electron Cyclotron Resonance Heating (ECRH). Its description will be made in the next chapter, for now, it is important to know that one of the main components of this systems are the mirrors, apt to reflect microwaves beams. The thesis is focused on these structures, in particular to their design, from thermal and structural point of view. Thanks to the knowledge gained from past projects, new mirror designs were proposed, adapted to different machines and requirements.
The mirrors are different, for locations, for use, for dimension, for requirements, but since they all have the same function, they are all subject to thermal loads, that increase their temperature and produce deformations, undesirable, as the cause of inefficiencies. In order to reduce the temperature and the related deformations, mirror design requires special care, so many different studies can be conducted. They will concern the materials, the geometries, the cooling systems, alternative shapes and so on. A lot of thermal and structural simulations will guide the choices. The technical approach is related to the definition of CAD models and FEM simulations, using tools based on well-known thermal and structural analysis methodologies.
The proposed methodology of study of the thermal and structural behaviour of the mirror will be presented later. It will be applied to different kinds of mirrors: mirrors of the launcher systems (explained in the next chapter) or mirrors of the transmission line. It is also applied to different facilities. DTT will be the main part of the thesis, with the study of its many mirrors. Another application will concern DEMO mirrors. In this case the design of the mirror will cover also another technical part: a proposal of the mechanical design of its supporting structure and its enclosure. The last application will concern a spherical tokamak and the study of the thermal behaviour of one of its launcher mirrors.
The final designs achieved in the various applications of this thesis may not be the final solution that will be adopted in the various tokamaks,

especially since some of them are in the conceptual stage, but they will provide an important basis for improving and constructing the final mirrors that will be mounted in future tokamaks.

This Thesis is articulated as follows. Chapter 2 provides an overview of the ECRH system and describes the mirror function and its design-necessity. Chapter 3 describes the technical approach and general assumptions used along the thesis. Chapter 4 gives an overview of the DTT project. Chapter 5 and 6 describes the design-development of the DTT launcher mirrors and the DTT transmission-line mirrors, respectively. Chapter 7 describes the activity related to a DEMO mirror. Chapter 8 describes the study about a mirror of ST40. Finally, the conclusions are summarized in section 9.

1.5 Disseminations of research results

Some outcomes of these studies are part of presentations at international conferences:

- 31st Symposium on Fusion Technology (SOFT2020):
  S. Garavaglia et al., *Progress of DTT ECRH System Design.*
- 29th IEEE Symposium on Fusion Engineering (SOFE-2021):
  A. Allio et al., *Assessment of the performance of different cooling configurations for the launcher mirrors of the ECRH system of the DTT facility.*
- 21st joint workshop on electron cyclotron emission (ECE) and electron cyclotron resonance heating (ECRH) (2022):
  A. Romano et al., *The design of the ECRH system of DTT.*
- 21st joint workshop on electron cyclotron emission (ECE) and electron cyclotron resonance heating (ECRH) (2022):
  S. Garavaglia et al., *Development of the Multi-Beam Transmission Line for DTT ECRH system.*
- 32nd Symposium on Fusion Technology (SOFT2022):
  A. Bruschi et al., *Conceptual Design of the DTT ECRH Quasi-Optical Transmission Line.*
- FuseNet PhD Event 2022:
  A. Salvitti et al., *Preliminary thermo-structural analyses on parabolic mirror of the Multi Beam Transmission Line of DTT ECH system.*

Moreover, some outcomes of these studies are part of journal publications:

- **A. Salvitti**, A. Bruschi, D. Busi, F. Fanale, F. Giorgetti, G. Granucci, G. Calabrò, P. Fanelli, M. Nobili, *Preliminary design and thermal analyses of the steerable mirror cooling channel of the DTT ECRH*, Fusion Eng. Des., 161, December 2020, 111880
(https://doi.org/10.1016/j.fusengdes.2020.111880)

- S. Garavaglia, B. Baiocchi, A. Bruschi, D. Busi, F. Fanale, L. Figini, G. Granucci, A. Moro, P. Platania, N. Rispoli, A. Romano, **A. Salvitti**, E. Sartori, S. Schmuck, E. Vassallo,*Progress of DTT ECRH System Design*, Fusion Eng. Des., 168, July 2021, 112678
(https://doi.org/10.1016/j.fusengdes.2021.112678)

- A. Allio, A. Bruschi, D. Busi, A. Bussolan, F. Fanale, P. Fanelli, S. Garavaglia, F. Giorgetti, A. Romano, **A. Salvitti**, and Laura Savoldi, Member, IEEE, *Assessment of the performance of different cooling configurations for the launcher mirrors of the ECRH system of the DTT facility*, IEEE Transactions on Plasma Science, June 2022
(https://ieeexplore.ieee.org/document/9806430)

- A. Bruschi, A. Allio, F. Fanale, P. Fanelli, S. Garavaglia, F. Giorgetti, G. Granucci, A. Moro, P. Platania, A. Romano, **A. Salvitti**, L. Savoldi, S. Schmuck, A. Simonetto, *Conceptual Design of the DTT ECRH Quasi-Optical Transmission Line*, Fusion Eng. Des., 194, September 2023, 113727
(https://doi.org/10.1016/j.fusengdes.2023.113727)

One journal publication is in "submission phase":

- **A. Salvitti**, A. Bruschi, G. Calabrò, F. Fanale, P. Fanelli, S. Garavaglia, F. Giorgetti, G. Granucci, A. Moro, P. Platania, A. Romano, *Preliminary Thermal and Structural Analyses on the Parabolic Mirror of the Multi-Beam Transmission Line of the DTT ECRH System*, **submitted** to Fusion Engineering and Design.
(Available at SSRN: http://dx.doi.org/10.2139/ssrn.4464489)

Chapter 2

ECRH and its Mirrors

2.1 Additional Heating Systems

The aim of fusion research is to achieve a "burning plasma": fully ionised gas self-sustained by power released from fusion reactions. For this scope, it is necessary to win two challenges. First: the temperatures inside a tokamak must reach 150 million ^oC - or ten times the temperature at the core of the Sun - so that the gas in the vacuum chamber can reach the plasma state and the fusion reaction can occur. Second: the hot plasma must be sustained at extreme temperatures in a controlled way in order to extract energy and avoid excessive heat losses. Therefore, the plasma must be sufficiently heated, confined and controlled.

Tokamaks utilise a method that works on both challenges at the same time: a huge electric current is induced in the plasma to heat it and to generate the confining magnetic field. The electric current produces heat due to the Joule Effect, but Ohmic heating is ineffective at high plasma temperatures. So, additional methods can be used: Plasma compression, Magnetic induction, Electromagnetic waves, Particle beam injection and Plasma guns [12].
Furthermore, tokamaks cannot maintain a continuous electrical current in the plasma. So an additional 'current drive' has to be provided if the burning plasma must be confined continuously. Electromagnetic wave current drive offers a possible solution.
Another aspect is the control of the performance-parameters that change instantaneously. Neutral beams and resonant electromagnetic waves are,

nowadays, the key tools in optimising the plasma performance.
Finally, the heating and current drive facilities have an even greater mission when applied in the Real Time Control. They can be used to automatically contrast plasma instabilities, vertical displacements of the plasma or disruptions or to safeguard an intended change in plasma parameters.
The main methods used in many facilities are the particle injection and the EM waves. In such context, the Neutral Beam Injection (NBI), and two sources of high-frequency electromagnetic waves, the Ion Cyclotron Resonance Heating (ICRH) and the Electron Cyclotron Resonance Heating (ECRH), play a dominant role. [13].
Facilities as ITER, DTT, DEMO will use the three main systems as exposed in [13, 14, 15]. To cover the total power to be provided at the plasma the systems are set in different way, with different capacities. ECRH has proven to be a useful heating mechanism in present day tokamaks and may play an important role in a next generation experiments. It will provide the most part of the power in DTT, and in DEMO it may be the key system for the plasma heating.
This thesis focuses on the ECRH system.

2.2 ECRH and its MIRRORS

In this section, a general overview of the ECRH system is given, but each ECRH system of the different facilities, considered in this thesis, will be better explained in specific sections.

ECRH is a system that generates microwave beams of the same frequency as the electrons of the plasma moving around the magnetic field lines. These microwaves are absorbed by the resonant electrons and the plasma heats up [16]. It is a very precise and powerful heating tool: it permits to modify the temperature profile in the plasma, depositing heat energy at selected locations, being the cyclotron frequency dependent on the magnetic field, which itself is a function of the location. Moreover, if the microwave beams are launched under an oblique angle with respect to the field-lines, making use of mirrors, local currents may be driven, modifying themselves the confining magnetic field.

The basic configuration consists of a source sending waves along a transmission path to a launching structure at the plasma edge. The source

is driven by a high-voltage power supply. The type of source utilized depends upon the operating frequency. The ECH requires Radio-Frequency (RF) waves at the electron cyclotron frequencies. It uses a source generating typical frequencies of millimetre waves ($\sim$ 100-200 GHz): the gyrotron [5].
The transmission path is usually constituted by waveguides, used to transmit RF power. This is the type used in ITER [17]. But some studies demonstrated the higher efficiency of quasi-optical Transmission Line (TL), able to reduce the losses [18, 19, 20], where the propagation of the microwave beams is realized by sets of mirrors. In the recent applications, for example in DTT [21] or in future in DEMO [22], the line is also evacuated (under vacuum) to reduce the losses due to air and arc risk.
The launcher launches the microwaves beams directly at the plasma. It is a structure that acts as the interface between the transmission circuit and the edge of the plasma. Often a mirroring system is used [5].

2.2.1 ECRH Mirrors

The basic element of a quasi-optical TL and a launcher is the ***Mirror***, core of this thesis. The main function of an ECRH mirror, in both TL and launcher, is to transmit the power to the plasma, reflecting the microwave beams, ensuring the optimal optical performances. It is physically impossible having a perfect reflection: despite there are materials with high performance in optical field, a 100% reflection is impossible. So, during a pulse, a fraction of the incident power, transported by a beam, is absorbed by the mirror, depending on the optical features of its material. The absorbed fraction of the beam power is a thermal load for the mirror. Besides, if the mirror is near the plasma (for example in the luncher), it is subject not only to the beam power, but also to other thermal loads. As a natural consequence, the mirror heats up at each power pulse. Therefore, it is essential to design the mirror in such a way that, despite thermal loads, its optical characteristics are preserved as much as possible.
The temperature is directly connected to the mirror deformation, in particular due to thermal expansion effect. The deformations of the mirror, due to temperature and modes of constraint, could result in high decrement of mirror efficiency of reflection, so it's important to maintain the mirror at a low temperature and to realise a design that reduces deforma-

tions, avoiding excessive overheating and permanent strains.
The most of the mirrors, presented in the thesis, need active cooling to dissipate the heat, but also a preliminary study of thermal behaviour for a particular mirror without active cooling will be presented.

The state of the art concerning the design of ECRH mirrors is mainly based on the R&D activity done for ITER and Wendelstein 7X (W7-X). It represented the guideline for the present work.
The studies of the ITER first mirrors of the optical diagnostics reported in [23], demonstrate that structures, subject to plasma radiation and neutron load, need necessarily an optimized cooling system and that the use of *CuCrZr* alloy is capable to reduce heating and surface deformation .
Other studies were carried out on the mirrors of the ITER Electro Cyclotron Upper Launcher about mirror technology, materials and manufacturing [24], or about a novel water cooled mirror design concept [25]. In [26] a study of the thermal condition and associated deformation is reported.
Also very inspiring was the work done for the mirrors of the transmission line of W7-X reported in articles [27, 28, 29], in which they studied the mirror technology, the materials, the geometry, particular cooling systems, the manufacturing, supporting systems, thermal stresses and related deformations.

The possibility of applying already known solutions to mirrors of new machines, studying the effects of new design choices, cooling systems, materials, geometries, adapting them to the needs of different facilities, or to the requirements of different parts of the system, allowed the birth and evolution of this thesis.

Chapter 3

Technical approach to FEM analyses

3.1 FEM Tools

Thermal analyses and structural analyses are the basis on which the development of the mirrors design is made.
In these studies the software chosen to implement Finite Element (FE) analyses is ANSYS® [30]. The analysis which exploits the Finite Element Method (FEM) is a Computer Aided Engineering (CAE) methodology that permits the numerical simulation of physical phenomena with the identification of results starting from the imposition of constraints and loads [31]. The obtained results are approximate because the calculators can't solve equation in closed form, but only using numerical methods, often because the physical laws that govern phenomena are differential and not linear.
Inside the software environment it is possible to execute a lot of modular analyses with different physics. In this thesis coupled thermal and structural finite element simulations will be carried out.
The design of the mirrors evolves starting from thermal analyses which address the choices of the best thermo-hydraulic parameters. The water is the refrigerant fluid of the mirrors. It has got an important role: it must be able to extract part of the heat impacting on the structure in order to reduce as much as possible the maximum temperature reached on the structures and consequently the mirrors deformation, related to the effects of thermal expansion. Since the water flows in a little duct, with

particular section, it will be characterized by specific dynamic features. So, it is possible to choose tools to perform thermal analyses, exploiting provided fluid-dynamic parameters deriving from input data without conducting fluid-dynamic analyses, which are more time-consuming and computationally intensive.

3.1.1 FLUID116

The environment of ANSYS permits to employ the fluid-thermal element FLUID116 [32] in steady-state and transient analysis. It has got the feature to include mass transport, heat transport and convection effects in 3D models without employing more complex CFD (Computation Fluid Dynamic) models. The fluid is transmitted between the two primary nodes of the element (I and J), as shown in figure 3.1. FLUID116 is a *line element* with two degrees of freedom: pressure and temperature. In the current analyses only the temperature degree of freedom has been adopted. The element is built on the line that indicates in mono-dimensional way the duct where the water flows. When the line is characterized by a cross-section, it represents the channel shape and it is meshed with thermal surface elements (i.e. SURF152 [32]).

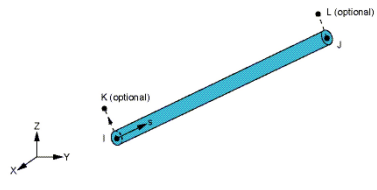

Figure 3.1: *FLUID116 Thermal-Fluid Pipe*

The bulk temperature, needed to define the heat transfer coefficient, will come from FLUID116.
In the master thesis [33], this methodology was tested, in particular the capability of FLUID116 to provide reliable results. For this scope this element was benchmarked against analytic test cases, solved through equations in closed form, for a simple forced-convection heat transfer example. It was considered validated because it provided accurate results, with maximum discrepancy from the analytic expectation of 1.3 %.
This approach simplifies the characterisation of the real fluid, losing detailed information on fluid dynamics (for example, it does not consider centrifugal effects in non-rectilinear pipes). Nevertheless, the technique is reliable; in fact, the temperatures of the structures are estimated to a good approximation, and they are the primary interest in the conceptual design phase in which the project is.

3.2 Heat exchange assumptions

The main heat exchange phenomena that take place inside these mirrors are the conduction and the convection [34]. To simulate the convection between fluid and solid it is necessary have the convection Heat Transfer Coefficient (HTC). It is known that the calculation of this coefficient is not trivial. For the applications presented in this thesis, it was decided to adopt the best known and most classic "Dittus-Boelter" empirical formulation [34], that expresses the Nusselt number as follows:

$$Nu = 0.023 \cdot Re^{0.8} \cdot Pr^{0.4} \tag{3.1}$$

where Re and Pr are respectively the Reynolds number and Prandtl number, dependent on cinematic, geometrical and physical properties of the water. The HTC is:

$$h = \frac{Nu \cdot \lambda}{D_h} \tag{3.2}$$

where λ is the thermal conductivity of the water and D_h is the hydraulic diameter of the duct-section ($D_h = 4 \cdot Section/Perimeter$).
"Dittus-Boelter" correlation in combination with the use of FLUID116 elements was used also by the authors of [35] for the ITER thermal shield analysis.
Following the aforementioned formulation, the convection coefficient needs to be analytically calculated for each individual simulation, due to its dependency on several quantities as flow rate and geometrical and physical properties. Besides, since it is strictly dependent on the water temperature, it would change along the channel both in space and time. Numerically, without recurring to CFD analysis, it isn't possible to simulate the high variability of the HTC, but it is possible, with a little approximation, to use an average HTC between the water inlet and water outlet conditions. But if the outlet condition is unknown, it would be necessary to elaborate an analysis with iterations to individuate firstly the outlet temperature of first iteration and then, with it, calculate the HTC at the water average temperature. It will explained in section 5.1.5.
In case of low water temperature difference between the inlet and outlet, the physical properties do not change significantly, so it will be possible to calculate the HTC at the water inlet temperature, with a negligible error. Furthermore, the HTC increases with temperature, so considering the inlet temperature means considering lower HTC, which worsens the

convection. This means being conservative when estimating the maximum temperature, which will be higher.
For each simulation it will be specified if the HTC will be evaluated with water properties referred to inlet temperature or average temperature, and, in this case, the specific iterative procedure applied will be explained.

3.3 Thermal Load

As already mentioned, the main function of any mirror of an ECRH system is reflecting microwave beams. Different mirrors can reflect only one beam or more beams simultaneously, however always, a fraction of the incident power transported by the beam is absorbed at the mirror surface. In this section it is presented the main thermal load which characterises the most of the ECRH mirrors studied in this thesis.
The power transmission from the gyrotron to the launcher is fully based on the propagation of Gaussian beams [21], and the concept of the transmission is based on quasi-optical propagation laws [18].
The thermal load related to the microwave beam is a surface load, defined considering a Gaussian distribution of power in the beams, with size defined according to the transmission line design.
The incident power density per single beam is calculated as follows:

$$P_{inc} = P_0 \; e^{-2\left[\left(\frac{x_L}{w_x}\right)^2+\left(\frac{y_L}{w_y}\right)^2\right]} \tag{3.3}$$

where the power density peak is:

$$P_0 = \frac{2Q}{(w_x w_y \pi)} \tag{3.4}$$

Q is the total power of a single gyrotron beam. The coordinates x_L and y_L are the coordinates of the local system on the mirror, whilst w_x and w_y are the beam size along the x_L and y_L directions.
The load is the absorbed power density on the mirror surface, calculated as:

$$P_{abs} = P_{inc} A \tag{3.5}$$

A is the absorption coefficient, evaluated as follows [18, 36]:

$$A_\perp = f_{roughness} \cdot (1 - |r_\perp|^2) = f_{roughness} \cdot 4 \; cos(\alpha_i) \; \frac{R_s}{Z_0} \tag{3.6}$$

$$A_{\parallel} = f_{roughness} \cdot (1 - \left|r_{\parallel}\right|^2) = f_{roughness} \cdot (\frac{4}{cos(\alpha_i)}) \frac{R_s}{Z_0} \tag{3.7}$$

$f_{roughness}$ is the roughness factor, r is the reflection coefficient considering the polarization (perpendicular or parallel), α_i is the incidence angle of the beam, R_s is the electrical resistivity of the reflective material at ambient temperature and Z_0 is the impedance of free space.

Chapter 4

Divertor Tokamak Test facility

Before presenting all the activities related to the Divertor Tokamak Test (DTT), the facility is presented.

DTT facility [37, 38, 39, 40, 41] is a new project, born inside the mission two of the Fusion Roadmap [42] to investigate alternative power-exhaust solutions for nuclear fusion reactors. DTT has been proposed by Italian Scientific Community, promoted and funded by the Italian Government and supported by EUROfusion and other contributors, such as the CREATE Consortium, ENEA and ENI. The construction of this machine is starting in the ENEA Site, Frascati, Italy.
It will perform a lot of scaled divertor experiments, under integrated physics and technical conditions that can be reliably extrapolated to DEMO, the future nuclear fusion demonstration power plant [43].
The DTT facility is designed to study several, quite different solutions for the power exhaust problem, such as advanced divertor magnetic configurations and liquid divertor metals, but also to propose innovative solutions. Flexibility is needed for technical and scientific reasons, but it is also required due to its long operative timescale. It is planned to operate to accompany the ITER [6] experiment as well as the DEMO design [44].
It is an up-down symmetric and superconducting tokamak with major radius of 2.19 m, corresponding to a plasma volume of 28 m^3 (fig. 4.1). The on-axis maximum toroidal field is of 6 T, and the maximum discharge duration allowed by the power supplies and the superconducting coils is

100 s. The maximum plasma current in the single null reference scenarios is of 5.5 MA, with an additional auxiliary total power of 45 MW provided by additional heating systems.
In the following list there are the main objectives of DTT, as reported in the roadmap [6]:

- 'test whether the alternative divertor solutions (such as advanced divertor configurations or liquid metals) can be technically integrated and are able to withstand the strong thermal loads in the DEMO device if the fraction of radiated power turns out to be lower than expected';
- 'improve the experimental knowledge in the heat exhaust scientific area for parameter ranges that cannot be addressed by present devices'.

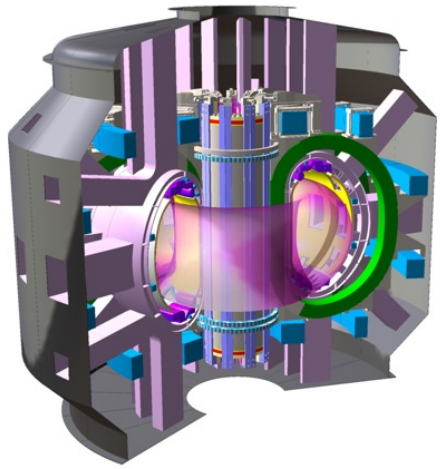

Figure 4.1: *Pictorial design of the future DTT machine [45]*

To be relevant for DEMO [43] exploitation, and to satisfy its requirements, DTT has to be characterized by the following specific ratio [37]:

$$P_{sep}/R = 15\ MW/m \tag{4.1}$$

where P_{sep} is the power crossing the boundary of the plasma and R is the major radius of the machine. In order to guarantee this value, it is necessary to provide to the plasma a supplementary heating power of 45 MW. The additional heating systems [46] can cover different tasks in

addition to the main one [37, 46], such as the H-mode access, the Electron and Ion Heating, the Current Drive, the magneto-hydro-dynamic (MHD) control, the Fast Particle Generation and the Profiles Control. Three specific systems are chosen: the NBI [47] and two sources of high-frequency electromagnetic waves (RF Heating), the Electron Cyclotron Resonance Heating (ECRH) [48] and the Ion Cyclotron Resonance Heating (ICRH) [49].
The full power configuration (45MW - 6T - 5.5MA) will be completed passing through two intermediate steps "day-0" and "day-1" [37] and it will foresee 4 ECRH cluster (28.8 MW at plasma), 2 ICRH antennas (6 MW at plasma) and 1 NNBI injector (9.5 MW at plasma) [37].

4.1 DTT ECRH

The DTT ECRH system (fig. 4.2) will be one of the largest systems in the world.

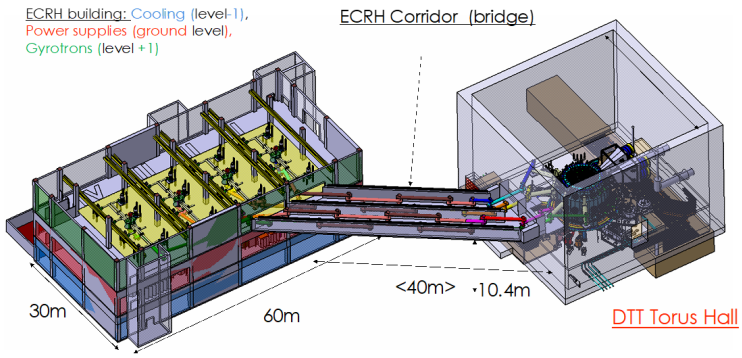

Figure 4.2: *Top view of the ECRH system joint to DTT Torus Hall.*

Its architecture is based on 4 clusters, each one constituted of 8 gyrotrons, the RF source, one Transmission Line (TL) and 8 independent launchers [50]. The power produced by the gyrotrons is transmitted by a series of flat and focusing mirrors, enclosed in an envelope under vacuum, and it is launched into the plasma by a pair of mirrors in the port plug for each launcher.

The gyrotron has a frequency of 170 GHz and produces a millimetre-wave beam of 1 MW of power [46]. The power handling requirements include the flexibility to increase the power up to 1.5 MW, considering a

future upgrade of the gyrotron power [48]. The RF pulse is expected to be active for 100 s continuously with a repetition rate of one pulse per hour [48].

4.1.1 DTT Transmission Line

The TL is ideally divided into three parts: the first and the third parts are Single-Beam Transmission Lines (SBTL), located close to the gyrotrons and just before the launcher. The central part of the TL is a Multi-Beam Transmission Line (MBTL), most of which is located in a corridor between the gyrotron building and the torus hall. It is composed of large focusing and plane Multi-Beam Mirrors (MBMs), each dedicated to the reflection of 8 beams at the same time. 8 MBMs, 4 focusing and 4 flat mirrors constitute the basic unit (Fig. 4.3) in the corridor.

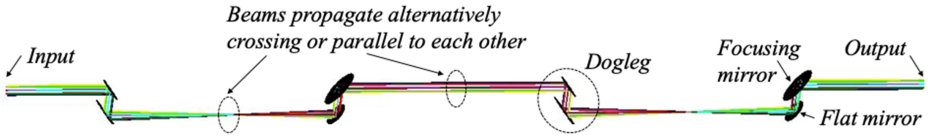

Figure 4.3: *Representation of the basic unit of an MBTL, with 8 reflecting mirrors (4 focusing and 4 flat mirrors). Figure from [48].*

4.1.2 DTT Launcher system

The current ECRH system foresees two launching antennas per DTT cluster, based on the front-steering concept (fig. 4.4). The equatorial antenna is dedicated to plasma heating and current drive and the upper antenna to the stabilization of MHD instabilities. The progress of the design concept of the launcher is shown in the article [51]. The thesis, instead, will show the first passes which brought to the latest configuration in [51]. In particular, the work in thesis was reported in the articles [48] and [52].
The launchers of all the beam lines are identical to each other and include a pair of mirrors to guide the beam in a dog-leg path [51]. The first mirror ($M1$) is fixed and curved (fig. 4.5 left), whilst the other ($M2$), faced to the plasma, is movable and flat (fig. 4.5 right).

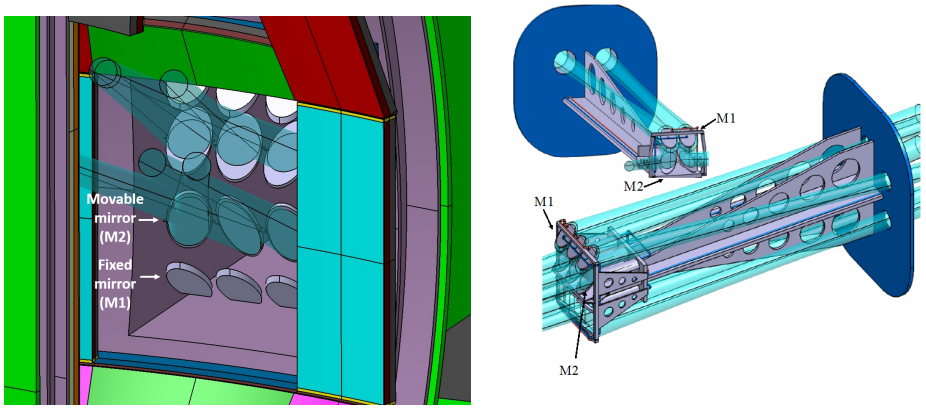

Figure 4.4: *Left: Preliminary CAD design of the equatorial launcher concept, without the mechanical supports of the mirrors [52]. Right: Upper (top) and equatorial (bottom) antennas. In grey the supporting structure, in blue the closure plate and in light cyan the beams [48].*

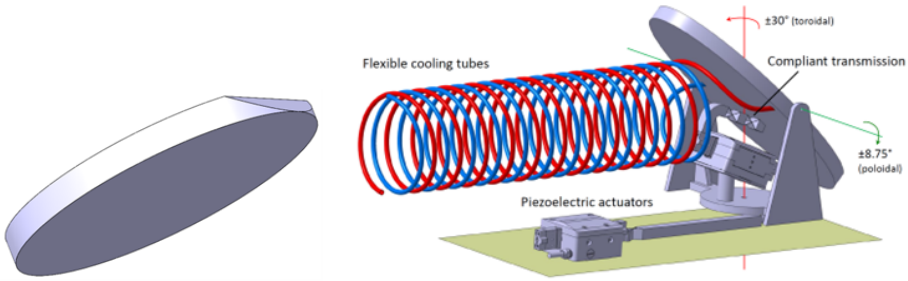

Figure 4.5: *CAD design of the mirrors M1 (left) and M2 (right) [48]*

Chapter 5

DTT Launcher mirrors

5.1 Preliminary M2 mirror design

The scope of this section is studying the thermal behaviour of the movable mirror $M2$ of the DTT ECRH launcher (fig. 5.1), making a preliminary design of the cooling channel, to be realized inside the mirror thickness. Several configurations of the channel are considered with the aim of finding out which one has better performances from a thermal point of view. The best found solution is exploited in an automatic procedure to evaluate the mirror temperature distribution while ranging two input parameters.

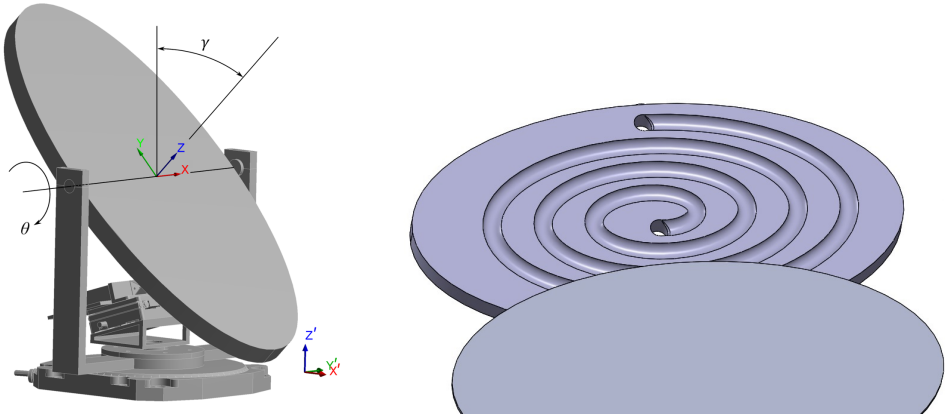

Figure 5.1: *Left: M2 steerable-flat mirror with the hypothetical design of the steering mechanism [53]. Right: CAD representation of the mirror with the dig of the channel and the Copper layer (left).*

This first part of the work has been published in [52].

The conceptual design of the front steering launcher foresees two mirrors for each line, in which a facing plasma one is moved to steer the EC power in different locations of the plasma, whilst other one is fixed and it does not directly see the plasma.
Every mirror transmits 1 MW to the plasma and less than 1% of the power is absorbed by the mirror-surface. The mirrors of the launcher closest to the plasma are also subject to its radiation and to neutron irradiation. To extract the heat coming from this kind of thermal loads the mirror is cooled.
Within a preliminary design, it is important to evaluate the refrigerant fluid (water) capability to extract the heat generated on the mirror surface, while it flows in a duct realized within the mirror itself. In this section dimensional, physical, and thermodynamic aspects will be discussed.

5.1.1 Requirements

The chosen refrigerant at this stage of the design is water [53]. For the first evaluation a pressure of 4 *bar* at the inlet has been considered. This pressure defines the water properties and also the boiling temperature and consequently the maximum allowable temperature for the fluid. Such value was chosen because it is easily obtainable from the primary water circuit, but in case of change of the cooling system this kind of choice can be reconsidered.
The prescribed water temperature at the inlet is $50°C$. This limit comes from the operating conditions of the other cooling systems of the in-vessel structures close to the ECRH launcher. Instead, the Volume flow rate can be a value in the standard range: $[10 \div 15\ l/min]$. The water properties are taken from the databases of the *National Institute of Standards and Technology* (NIST) [54].
In the current design the cooling duct is expected to be dug in the mirror using the milling method. The first proposal is to realize a duct with semicircular section. Once milled, a layer with 2 mm thickness will cover the mirror and close the duct. The first idea for the materials foresees *Copper-Chromium-Zirconium* alloy (CuCrZr) for the mirror-bulk (back-side of the final structure) and pure Copper for the cover layer (front-side of the final structure) [53]. The surface deposition of the copper will be realized with

a process of electro-forming. The mirror with the dug channel and the cover layer are represented through the CAD model of Fig.5.1 right.

The most important requirement that will drive the design choices, is to maintain the structure temperature as low as possible below a threshold temperature. The maximum allowable surface temperature of the mirrors, due to all heat loads in a steady state condition, is 200^oC. This limit concerns mainly the copper, that above this temperature, subject to the pressure of the flowing water, starts to deform significantly. This is the worst case for the system because it affects the capability to correctly reflect the microwave beam.

In Fig. 5.1 left the movable mirror is visible in a preliminary CAD design. The minor semi-axis (located on the X-axis of the local reference system X-Y-Z) is 69 mm, whilst the major semi-axis (on Y-axis) is 132 mm. The mirror-bulk thickness is instead 12 mm, thin to be light and easy to move.

5.1.2 Data and Hypotheses

The mirror $M2$ is placed inside the machine vacuum vessel and its front surface is oriented towards the plasma. This face is subject to three different thermal loads: the radiative power (irradiated from the plasma), the power absorbed by the mirror due to the reflection of the microwave beam (surface loads) and the neutron irradiation (volume load), coming from the plasma and due to D-D reactions.

- The neutron irradiation is uniform all over the mirror volume, with a value of 10 kW/m^3 (~ 3.4 W of total power on the mirror).

The other two kinds of surface loads could change with the orientation of the mirror.
The nominal position, shown in figure 5.1 (left), is obtained by a rotation of $\gamma = 45°$ around the X-local-axis, starting from the horizontal position of the mirror. Each angular variation from the nominal position is defined by the mechanical angle θ. So, the reference case for this study foresees $\theta = 0°$.

At the base of the following values of the loads there is a conservative hypothesis, that considers the mirror surface covered by a very thin layer of tungsten, due to the deposition of the sputtered matters from the tokamak walls by plasma.

- The radiative load depends on the mirror exposition to the plasma. For the nominal position it is 0.177 MW/m^2. It is uniform on the surface of the layer and generates an overall radiative power of 5.06 kW. Its value comes from the maximum radiated power load on the DTT first wall from the plasma (0.5 MW/m^2) [37], considering a conservative absorption coefficient of the tungsten (0.5), based on its spectral emissivity [55], and the incidence angle of the beam (45° in this case).

$$P_{radiative_{absorbed}} = 0.5\ MW/m^2 \cdot 0.5 \cdot cos(\alpha_{incidence}) = 0.177\ MW/m^2 \tag{5.1}$$

- The microwave load is defined as reported in section 3.3 with equations 3.3-3.4-3.5.
  In this case: the total power of the beam $Q = 1$ MW; the absorption coefficient "A" is evaluated with eq. 3.6 considering perpendicular polarization, a $f_{roughness} = 2$ and the surface electrical resistivity R_s of tungsten at $227°C$.

Overall the microwave absorbed power is 7.8 kW. In Tab. 5.1 the parameters for the beam load calculation are summarized. The analytic 3D curve of the absorbed power as a function of the coordinates x and y is represented in Fig. 5.2 right.

Table 5.1: *Beam Load parameters for M2 Case 2 ($\theta = 0°$).*

w_x [m]	w_y [m]	P_0 [MW/m^2]	A
0.043	0.061	242.71	0.78%

The assumptions about the convection and the evaluation of the heat transfer convection coefficient are the same exposed in section 3.2. In the following first simulation, the HTC is evaluated with water properties referred to inlet temperature, because the outlet temperature is unknown.

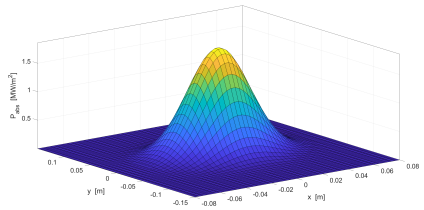

Figure 5.2: *Representation of the absorbed power density on a rectangular surface with the dimensions of the mirror-ellipse (right).*

This approximation, despite the lack of precision, is conservative and allows to establish the best configuration.

5.1.2.1 Channel design

Inside SOLIDWORKS® environment, the steerable mirror was considered without steering mechanisms, being not relevant under thermal point of view. Here the channel was realized in different configurations. Its basic shape follows a spiral, elongated on the major semi-axis [53], whose analytical definition is:

$$\begin{cases} r_i(\varphi) = k_i \varphi \\ x = r_x(\varphi)\ cos(\varphi) \\ y = \dfrac{b}{a}\ r_y(\varphi)\ sin(\varphi) \end{cases} \tag{5.2}$$

where the subscript i indicates x or y coordinates, whilst a and b are the ellipse minor and major semi-axes respectively. Using these parameters the elongation follows the mirror shape. Coefficient k defines the spiral pitch, constant or variable with the angle (φ), is defined as the distance between two passages of the curve in the same angular position.
Six kinds of spiral configurations are considered for the thermal analysis: elongated with constant pitch on y-axis, elongated with variable pitch on y-axis and the arithmetic spiral. For each kind there are a configuration with the inlet centred in origin and a configuration with the inlet not centred (x_0 parameter). The coefficients to be inserted in Eq.5.2 that allow to obtain the aforementioned configurations, are resumed in Tab.5.2.

The ratio $b/a = 1.9$ (i.e. major divided minor semi-axes) is the value that allows to better represent the elliptical shape of the mirror in the

Table 5.2: *Coefficients of the configurations.*

Configuration	k_x $[mm]$	k_y $[mm]$	φ *domain*	x_0 $[mm]$	b/a
a	2.3	2.3	$\pi < \varphi < 8\pi$	0	1.9
b	2.3	2.3	$\pi < \varphi < 7\pi$	7.2	1.9
c	2.3	$(0.02\ \varphi + 1.4)$	$\pi < \varphi < 8\pi$	0	1.9
d	2.3	$(0.02\ \varphi + 1.4)$	$\pi < \varphi < 7\pi$	7.2	1.9
e	2.0	2.0	$\pi < \varphi < 10\pi$	0	1
f	2.0	2.0	$\pi < \varphi < 9\pi$	6.3	1

elongated spirals. It analytically becomes equal to 1 in the arithmetic spiral.
The coefficients k_x and k_y come from evaluations of optimization of the shape, considering the possible technological realization limits. The values of 2.3 mm and 2.0 mm, for elongated and arithmetic spirals respectively, and the variable k_y for the configurations c and d permit to have a well distributed circuit upon the mirror surface, concentrated near the centre and to maximize the number of the spiral turns.
The dug mirror CAD models with all the different channel configurations are shown in Fig. 5.3.
As it is possible to notice from Fig. 5.3, the centred configurations lose a half-turn with respect to the not centred configurations, as also observable from domain angle of Tab. 5.2.
Furthermore, the constant pitch configuration is the most uniform over the mirror, while the variable pitch and arithmetic configurations exhibit a channel more concentrated in the central zone, where the RF load peak is expected.

The diameter of the channel chosen in this phase of the design, without considering the stresses and strains of the structure, is 10 mm, as trade-off between the dimensions of the mirror and pressure drops considerations.

5.1.3 FE Models

All the thermal simulations were performed considering the FEM tools exposed in section 3.1.
The CAD geometry was modified with the addition of a line body that defines the path of the water in the mirror, characterized by a specific

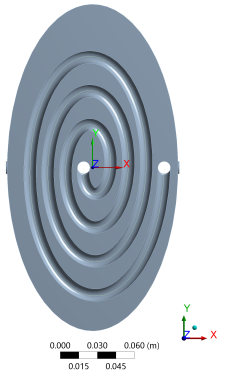

(a) *Elongated spiral with constant pitch.*

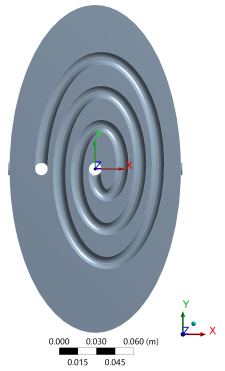

(b) *Centred elongated spiral with constant pitch.*

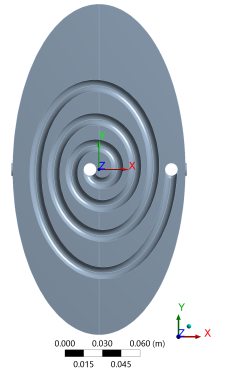

(c) *Elongated spiral with variable pitch.*

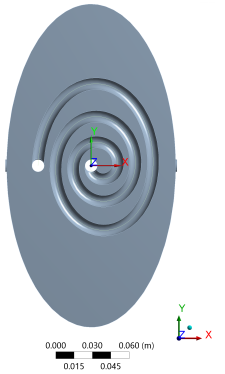

(d) *Centred elongated spiral with variable pitch.*

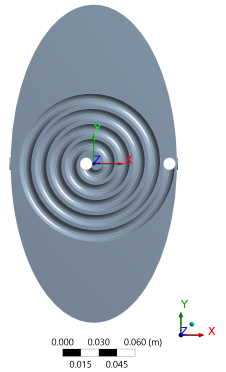

(e) *Arithmetic spiral.*

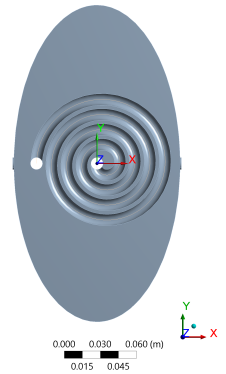

(f) *Centred arithmetic spiral.*

Figure 5.3: *Channel configurations with chosen spiral shapes.*

semi-circular cross-section. The *FLUID116* element was then assigned on the created line that indicates, in mono-dimensional way, the duct in which the water flows. Clearly, a different line body was created for each channel configuration.

The mirror thermal analysis is in a steady-state condition, because the flow of the water in the channel is in operative condition and also the loads during the plasma shot (pulse length of 100 s).
All models' mesh size was controlled using three specific "body sizing" on

the Copper layer, on the mirror-bulk and the line body. A mesh sensitivity analysis was carried out and brought to definitive parameters of meshing, with a total of 88189 nodes and 56690 elements. In Fig.5.4 left is shown the mesh of the mirror; the green edge shows the division of the two bodies (layer and mirror-bulk). Instead, in Fig.5.4 right is visible the detail of the mesh of the *FLUID116* "water" elements.

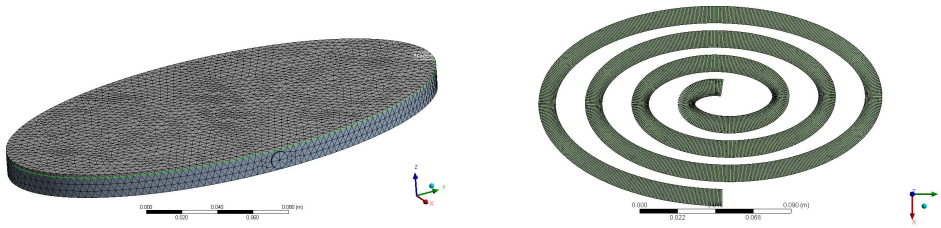

Figure 5.4: *Detail of the obtained mirror mesh (left) and of water mesh (right).*

5.1.4 Geometric configuration analysis

The first simulation features constant input parameters and aims to define the best geometric configuration for the channel.
The parameters to be set are: the temperature of the water at the inlet, the mass flow rate and the convection heat transfer coefficient. In particular the boundary conditions are:

- $T_{water_{inlet}} = 15°C$.
- $\dot{V} = 10\ l/min$. It is the minimum value of the range, chosen to minimize the pressure drops.
- $h \cong 16000\ W/m^2K$ calculated with the Eq. 3.2, considering the water properties at the $T_{water\ inlet}$.
- Microwave beam power density, not uniform on the layer front surface, depending on the incident beam and previous Eq. 3.5.
- Radiative Power density, uniform on the layer front surface, 0.177 MW/m^2.
- Neutron Power density, uniform on all the volume of the layer of coverage and the mirror, 10 kW/m^3.

5.1.5 Dependency to water parameters analysis

The second simulation is aimed to determine how the mirror behaves, in terms of temperature distributions, when inlet water temperature and mass flow rate change. This task is accomplished through an automatic convergence tool developed inside ANSYS Mechanical.
The automatic iteration, pre-announced in section 3.2, has two objectives. The main one concerns the identification of the maximum surface temperatures as a function of the input parameters, namely the inlet temperature and volume flow rate of the water.
The second scope of the automatic iteration allows to overcome the approximation on the convection heat transfer coefficient calculation, up to now evaluated considering the water properties at the inlet temperature. The iterative procedure hereinafter proposed calculates the convection coefficient at the average water temperature between inlet and outlet. The iteration is necessary to find the initially unknown water outlet temperature. Once its value is found, the physical water properties can be calculated at the average temperature and the heat transfer convection coefficient will be calculated with reduced approximation.

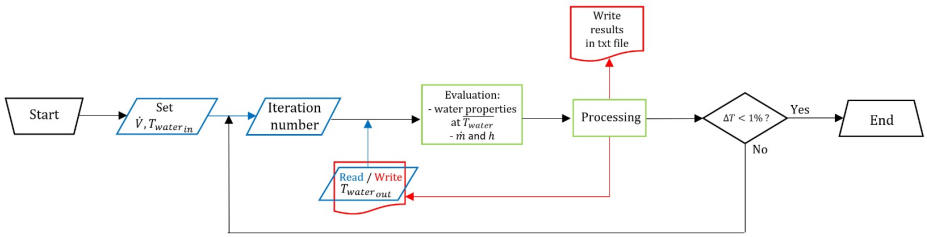

Figure 5.5: *Flow chart of the iterative process for the simulations with reduced approximations on the convection heat transfer coefficient (HTC).*

In Fig. 5.5 the flow chart of the iterative process is shown. The convergence is reached when the discrepancy between the last value of the temperature and the one of the previous iteration is less or equal to 1 %. When this circumstance occurs, the input parameters are changed and the iteration process is repeated until the new convergence.

Two different analyses were pursued: one in which the variable input is the inlet temperature of the water and a second one in which the variability

is related to the volume flow rate.

5.1.6 Results

In the Tab. 5.3 all the results of the thermal simulations for each channel configuration are reported. The results are related to the simulation with fixed inputs. The second column reports the value of the water temperature at the outlet and is approximately $33°C$ for all the configurations. The water heats up of $\sim 18°C$. The fact that all the configurations give the same outlet temperature was expected, since in this analysis the properties of the water don't change and the loads are always the same. So this result confirms the validity of the model.

Table 5.3: *Temperature results of six channel configurations.*

Configuration	$T_{out\ water}$ $[°C]$	$T_{max\ layer}$ $[°C]$	$T_{max\ bulk-side}$ $[°C]$	$T_{max\ layer-side}$ $[°C]$
a	33.01	122.1	108.9	107.7
b	32.98	139.5	110.6	107.7
c	33.04	154.1	100.8	104.8
d	33.01	220.1	117.9	117.9
e	33.08	183.8	97.32	94.32
f	33.07	220.1	111.1	111.1

In the third column the maximum surface temperature of the mirror is listed. In all the cases Copper layer is the part in which the highest temperatures are recorded, because directly exposed to the load. The highest values, over the allowable limit, is encountered in the configurations *d* and *f*. Consequently, such configurations don't respect the mirror requirements. The other ones are in the threshold value, even if the configuration *e* presents temperatures next to the imposed limit. The best results are obtained with elongated spiral configurations with constant pitch on the y-axis and, in particular, for the configuration with the inlet not centred in the origin (a), that provides the lowest layer temperature. It can be seen that the centred configurations show the highest values for each case because they lose a half-turn of the spiral.
The last two columns report the maximum surface temperatures of the channel on the mirror-bulk side and the layer side, relevant to avoid the formation of vapour. Although this eventuality would have increased the

heat transfer efficiency, however it is not recommended to exceed the onset nucleate boiling temperature. Indeed, it means necessarily to have an increment of the wall temperature, event opposite to the criteria of the design, for which the surface temperature of the mirror should be as low as possible, to reduce the strains of the structure, that negatively affects the efficiency of the beam transmission. Hence, in this kind of application it is preferable to remain in the turbulent flow, without entering the subcooled boiling.
So, surface channel temperatures must be lower than the boiling temperature of the water at a prescribed pressure. For the water at 4 bar, the limit of the surface channel temperature is $143.62°C$ and all the reported values are below this threshold value. It must be said that this is not constant all over the channel, because its value is necessarily affected by the pressure drops inside the channel. An accurate analysis of the pressure drop will allow to have a better estimation of the boiling temperature within the channel.

In Fig. 5.6 the contour plots of the surface temperature are visible for the configuration of the elongated spiral with constant pitch with inlet not in the origin (configuration a).
Figures 5.6a and 5.6b show respectively the contour plot of the surface temperature on the mirror-bulk not covered and on the layer of coverage. It is visible as the peak of the temperature occurs at the centre, where the beam load is maximum. In figures 5.6c and 5.6d the surface temperature of the channel is visible in both mirror-bulk and layer sides.

Fig. 5.7 presents the contour plots of the surface temperature of the mirror-bulk for all the analysed configurations. The first evidence concerns the position of the temperature peak. Only in configuration a, with the lowest temperature, the peak is located at the centre of the mirror. For the other ones, it is at the top and bottom edges of the mirror. The lowest recorded temperature on the Copper layer is $122.14°C$ for configuration a.

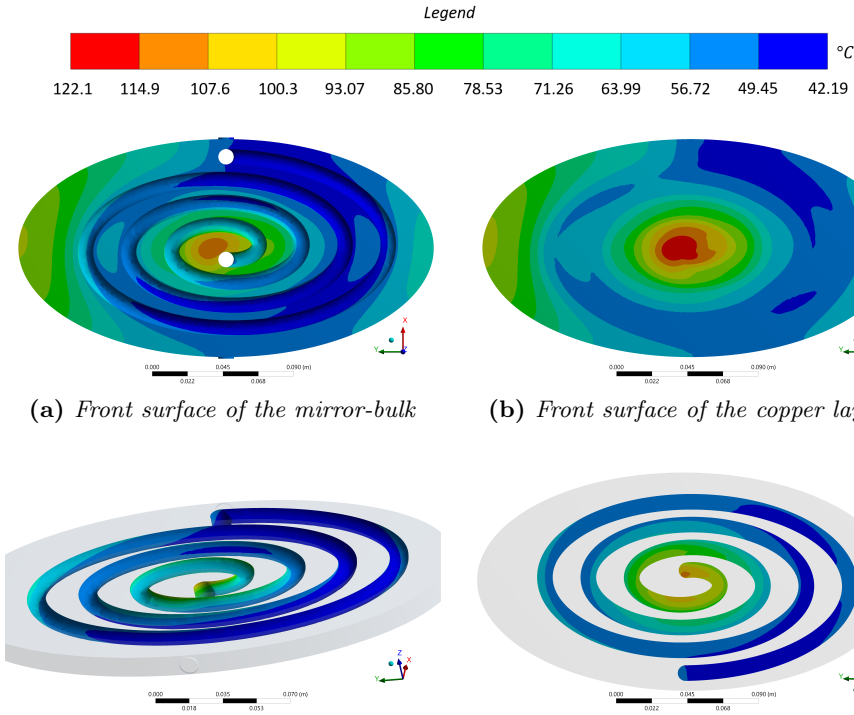

(a) *Front surface of the mirror-bulk*

(b) *Front surface of the copper layer*

(c) *Surface of the channel mirror-bulk side*

(d) *Surface of the channel layer side*

Figure 5.6: *Contour plot of the surface temperature for the configuration (a) with constant pitch with inlet not in the origin.*

5.1.7 Dependency to water parameters analysis results

The results of the automatic iteration are given in Tab.5.4 for the iterative analysis of the inlet water temperature, with a constant volume flow rate of 10 l/min.

As expected and known from a theoretical point of view, the results of the table show that the maximum temperatures of the mirror increase if the inlet water temperature arises. Besides, it is visible that the maximum temperatures remain lower than the threshold value ($200°C$) for each tested water inlet temperature.

To reach the results convergence, in this case, only three iterations must be carried out. Furthermore, the simulations performed with a convection heat transfer coefficient calculated at water average temperature between inlet and outlet (starting from iteration 2), lead to lower mirror temperatures than in the case in which HTC is evaluated at T_{inlet} (iteration

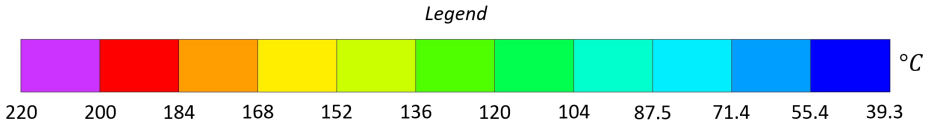

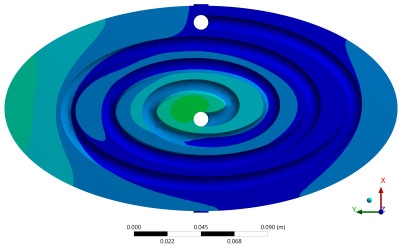

(a) *Elongated spiral with constant pitch.*

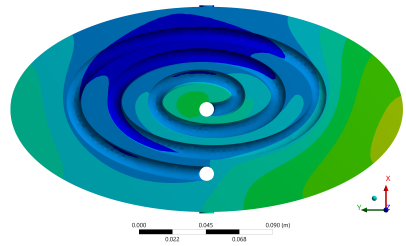

(b) *Centred elongated spiral with constant pitch.*

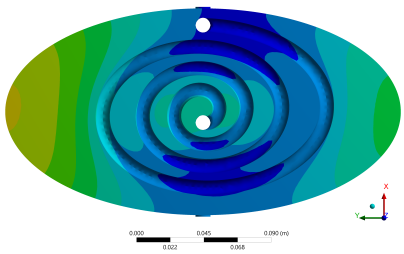

(c) *Elongated spiral with variable pitch.*

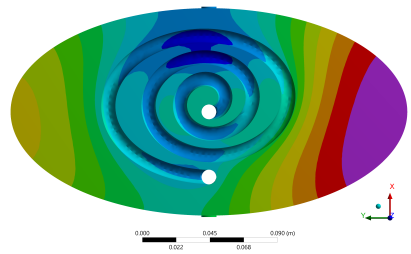

(d) *Centred elongated spiral with variable pitch.*

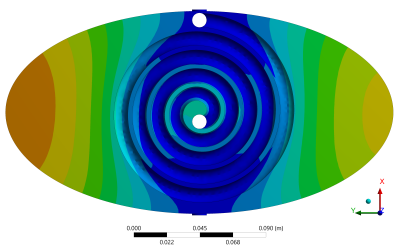

(e) *Arithmetic spiral.*

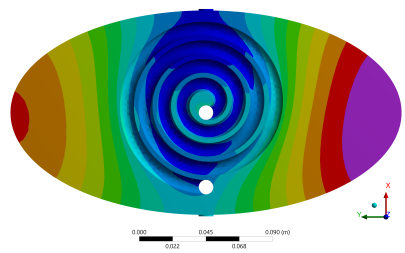

(f) *Centred arithmetic spiral.*

Figure 5.7: *Contour plots of the mirror-bulk surface temperature of all the configurations.*

number 1). Therefore the procedure avoids an overestimation of the simulated temperatures.

The same procedure is exploited for the analysis with the variation of

Table 5.4: *Analysis of the variation of the inlet water temperature with the right calculation of convection coefficient with all the thermal loads and a volume flow rate of* 10 l/min. *The yellow design points represent the last iteration for each chosen temperature.*

T_{in_W}	Iteration	$\dot{m}$	h	T_{out_W}	T_{max} Layer	T_{max} Mirr. chan.	T_{max} Layer chan.
$[°C]$		$[kg/s]$	$[\frac{W}{m^2K}]$	$[°C]$	$[°C]$	$[°C]$	$[°C]$
	1	0.1665	15675	32.98	121.7	106.8	107.2
15	2	0.1662	17374	33.01	116.5	101.1	101.2
	3	0.1662	17376	33.01	116.4	101.1	101.2
	1	0.1664	16626	38.00	123.6	108.4	108.7
20	2	0.1660	18296	38.04	118.9	103.3	103.3
	3	0.1660	18299	38.04	118.9	103.3	103.3
	1	0.1660	18478	48.05	128.3	112.7	112.7
30	2	0.1655	20082	48.09	124.6	108.6	108.6
	3	0.1655	20086	48.09	124.6	108.6	108.6
	1	0.1654	20251	58.09	134.1	118.1	118.1
40	2	0.1648	21780	58.16	131.0	114.6	114.6
	3	0.1648	21785	58.16	131.0	114.6	114.6
	1	0.1647	21937	68.15	140.6	124.2	124.2
50	2	0.1640	23385	68.22	138.1	121.3	121.3
	3	0.1640	23390	68.22	138.1	121.3	121.3

the volume flow rate. In this case the input parameters of each design point is the volume flow rate, whilst the temperature is kept constant and equal to $15°C$ (Tab. 5.5).

The results show that, increasing the volume flow rate, the maximum temperatures of the mirror decrease. The surface temperatures of the channel decrease, too. Such evidence was expected, because known from the theory, but it is relevant to confirm the correctness of the simulations.

The developed procedure also permits to vary simultaneously the flow rate and the inlet temperature, but this kind of analysis was not developed. However, it is known and it was found that the maximum temperature comes from the maximum T_{inlet} and the minimum volume flow rate. Considering the first one equal to $50°C$ and the second one equal to 10 l/min, the maximum mirror temperature is $138.09°C$.

Table 5.5: *Analysis of the variation of the volume flow rate with the right calculation of convection coefficient with all the thermal loads and an inlet temperature of* $15°C$*. The yellow design points represent the last iteration for each chosen volume flow rate.*

$\dot{V}$	$\dot{m}$	Iteration	h	T_{out_W}	T_{max} Layer	T_{max} Mirr. chan.	T_{max} Layer chan.
$[l/min]$	$[kg/s]$		$[\frac{W}{m^2K}]$	$[°C]$	$[°C]$	$[°C]$	$[°C]$
	0.1665	1	15675	32.98	121.7	106.8	107.2
10	0.1662	2	17374	33.01	116.5	101.1	101.2
	0.1662	3	17376	33.01	116.4	101.1	101.2
	0.1998	1	18136	29.98	113.7	98.27	98.28
12	0.1996	2	19777	29.99	109.7	93.91	93.91
	0.1996	3	19779	29.99	109.7	93.90	93.90
	0.2332	1	20517	27.83	107.6	91.74	91.74
14	0.2329	2	22110	27.84	104.5	88.26	88.26
	0.2329	3	22111	27.84	104.5	88.26	88.26

5.1.8 Preliminary M2 mirror design: first considerations

A preliminary study of the movable mirror M2 of the DTT ECRH launcher was conducted. The analyses aimed to find the first design of the cooling channel, to be dug in the mirror, with good performances from a thermal point of view. Six different configurations were proposed and the most promising one, with the lowest maximum surface temperature of the mirror ($122°$ C), is the elongated spiral with constant pitch on y-axis. Such configuration is efficient to dissipate the heat coming from both microwave and radiative loads, which are the greatest ones. This channel is concentrated in the centre to dissipate the maximum heat of the microwave load, but it is also extended on all over the mirror surface and manages to dissipate main part of the heat due to the radiative load that is uniform.

On the chosen design, other analyses put in evidence the trends of the maximum temperature of the mirror, as function of the inlet temperature and the volume flow rate, with properties of the water calculated at the average temperature. From obtained results it can be stated that in the worst studied scenario, namely $50°C$ of inlet temperature and 10 l/min of volume flow rate, the imposed temperature limit for the mirror is not

exceeded. In fact, the maximum found value (i.e. about $138°C$) on the mirror is well below the threshold (i.e. $200°C$). This result indicates a wide margin to improve the design of the structure considering new implications. The surface temperature of the channel increases until a value of $\sim 121°C$ and this means that, in order not to exceed the boiling temperature of the water, the maximum acceptable pressure drop between inlet and outlet is less than 2 *bar*, with a inlet pressure of 4 *bar*.

Next analyses will improve the design according to the variation of the requirements. Also structural simulations will be necessary to test the capability of the mirror to withstand the temperatures and bulk gradients, as well as to highlight critical locations, if any.
The herein proposed procedure will be also applied to test the other two M2 mirror orientations, as well as the fixed mirror M1.

5.2 M2 mirror design update and preliminary M1 mirror design

In this section, the other two orientations of the M2 mirror and the fixed mirror M1 are analysed. The acquisition of a lot of information on the behaviour of a launch mirror, thanks to the study on M2, can be used to continue the design of launch mirrors in parallel, now also considering mirror M1. This will lead to improve the design of M2 and to realize the preliminary design of M1, based on the knowledge already acquired.
M1 is a launcher mirror, fixed with a focalising surface (fig. 5.8).

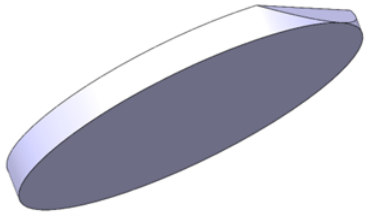

Figure 5.8: *CAD design of the mirror M1.*

5.2.1 Assumptions and requirements

About the requirements some variations were born:

- The **pressure of the water** has been reconsidered. In particular, the values which will be considered in the following simulations will be explained in section 5.2.5, in which the pressure inlet will be studied in function of the circuit.
  However this datum has not influence in the simulation. Indeed, a parametric analysis was performed in order to study how the pressure influence the maximum temperature of the mirror. Whereas the range of the water temperature is not much wide, the pressure hasn't a big influence on the water physical properties and consequently in the heat transfer coefficient. So the mirror temperature do not change significantly with the pressure of the water.

- The **water inlet temperature**. In the preliminary design a parametric analysis was done, changing this value. Now, it was decided to continue the project using a reference value. The research group

evaluated to set the datum at $50°C$. Indeed, from different studies they saw that the environment temperature inside the launcher is around this value and therefore, in order to avoid the condensation of the gas over the structures, it is important to not create cold points.

- The **volume flow rate** was optimized by a PhD student of the Politecnico di Milano with a 1D thermodynamic model [53]. The model foresees the minimization of the volume flow rate considering the constraints of the maximum admissible mirror temperature, pressure drops and outlet water temperature. So, the volume flow rate is 4 l/min. In accordance with the criteria used in the model, the optimal **diameter** of the semi-circular section of the cooling channel is 7 mm.

About the simulations instruments, there aren't variations. The used FEM tools are widely explained in section 3.1. The use of convection and the choices associated with it are explained in section 3.2.
The iterative procedure to calculate the HTC at the average water temperature between inlet and outlet, reducing the approximations, is the same used in section 5.1.5.

5.2.2 Geometry of the mirrors

Considering a new cross-section diameter (from 10 mm to 7 mm), the channel design is modified. By reducing the cross-sectional area, the number of revolutions of the spiral path can be increased and the pitch reduced. In the "elongated spiral with constant pitch" configuration (a), the pitch is $2.3mm \cdot 2\pi \cong 14.5mm$ (tab. 5.2). The pitch of the spiral is then reduced by the same value by which the diameter is reduced: 3 mm. It becomes 11.5 mm. The increment of the revolutions leads to a wider angular range that becomes of $\pi - 10\pi$.
Now the configuration of mirror M2 presents an elongated spiral that follows the elliptical shape of the mirror, with a pitch of 11.5 mm for the minor axis and for the major axis 11.5 mm multiplied by the ratio between the ellipse radii. The new configuration of M2 and the detail of its dimensions are reported in fig. 5.9.

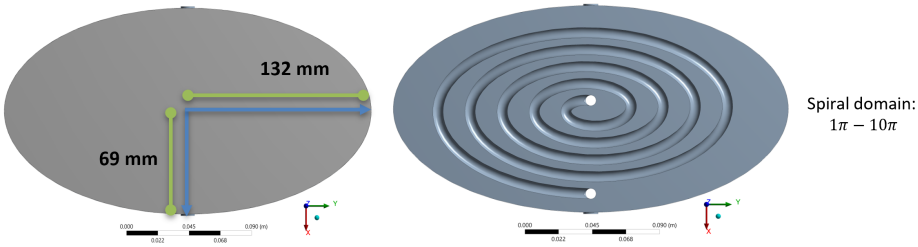

Figure 5.9: *Geometry details of the mirror M2.*

Found the best spiral configuration for the cooling channel of the mirror M2, the same path has been realized for the mirror M1, with the difference about the spiral domain of $\pi - 10.25\pi$. The configuration of M1 and the detail of its dimensions are reported in fig. 5.10.
The mirror M1 is thought having the same materials of M2: a bulk (thickness 13 mm) of CuCrZr alloy covered with a 2 mm Pure Copper layer on the surface.

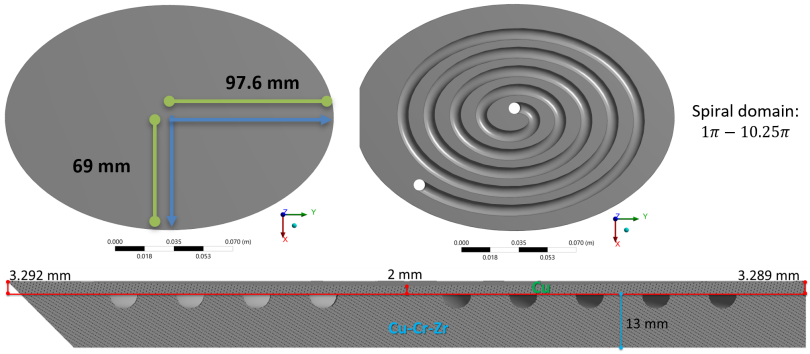

Figure 5.10: *Geometry details of the mirror M1.*

5.2.3 Loads

The position of the mirror M2 has been seen in the previous section, but in the next one the other orientations are presented. Being M2 movable, the load varies depending on the orientations. Being M1 fixed, there is only a set of loads for it. It is located specular to M2 (fig. 4.4), so its front surface is subject to the power absorbed by the beam, instead its back surface is subject to the power irradiated by the plasma. In addition, also the mirror M1 is subject to the neutron irradiation: uniform all over

the mirror volume, with a value of 10 kW/m^3.
The other two kinds of surface loads are reported in the figure 5.6.
The radiative load depends on the mirror exposition to the plasma, as exposed in section 5.1.2 and evaluated with the equation 5.1. The final values depend on the inclination of the mirror respect to the plasma. The nominal position of $\theta = 0°$ corresponds to $\alpha_{incidence} = 45°$, $\theta = 5°$ to $40°$ and $\theta = -12.5°$ to $57.5°$.
The microwave beam load is evaluated as shown in section 3.3. As visible in tables 5.6, the absorption coefficient A of the M2 ($\theta = 0°$) is 0.01% different from the previous section. This is because the physic research group of DTT, in the meanwhile, did some improvements to the provided data, that of course, due to different technical reasons can change during the project. In this case the change concerns the polarization considered in the calculation of the absorption coefficient, not more perpendicular, but parallel as in formulation 3.7.

The beam load is defined as reported in 3.3. Also the total power of a single gyrotron beam "Q" is a parameter that will change in the course of the thesis due to refinements made in the years by the DTT researchers. So, for each configuration it will be declared. In this case, it is considered a maximum gyrotron power of 1.2 MW. Due to the ohmic losses during the transmission (estimated by the researchers of $\sim 10\%$), the total Q arrives at the launcher with a value of 1.1 MW.

Table 5.6: *M1, M2 loads features.*

	Beam Power					
	w_x **[m]**	w_y **[m]**	$\dot{P}_0$ $[MW/m^2]$	**A%**	Q $[MW]$	$P_{tot} = Q \cdot A$ $[kW]$
M1 ($\theta = 0^o$)	0.046	0.065	234.2	0.79	1.100	8.690
M2 ($\theta = 5^o$)	0.043	0.067	243.1	0.87	1.100	9.570
M2 ($\theta = 0^o$)	0.043	0.061	266.9	0.79	1.100	8.690
M2 ($\theta = -12.5^o$)	0.043	0.051	319.3	0.66	1.100	7.260

	Radiative Power		
	$\dot{P}_{rad}$ $[MW/m^2]$	$P_{tot}rad$ $[kW]$	P_{tot} $beam + rad$ $[kW]$
M1 ($\theta = 0^o$)	0.177	3.74	12.43
M2 ($\theta = 5^o$)	0.192	5.49	15.06
M2 ($\theta = 0^o$)	0.177	5.07	13.75
M2 ($\theta = -12.5^o$)	0.134	3.83	11.09

5.2.4 Input and Achieved Results

The thermal analysis concerning the mirror M1 foresees the following inputs:

- Volume flow rate: $\dot{V} = 4l/min$.
- Water inlet temperature $T_{water\ inlet} = 50°C$.
- Water inlet pressure: $p_{water\ inlet} = 6\ bar$ (value explained in the section 5.2.5).
- Heat transfer coefficient: $h = 23000\ W/(m^2K)$, constant, calculated considering the water properties at $T_{water\ average}$.

The thermal analysis concerning the mirror M2 foresees the following inputs:

- Volume flow rate: $\dot{V} = 4l/min$.
- Water inlet temperature $T_{water\ inlet} = 50°C$.
- Water inlet pressure: $p_{water\ inlet} = 14\ bar$ (value explained in the section 5.2.5).
- Heat transfer coefficient: $h = 24000\ W/(m^2K)$, constant, calculated considering the water properties at $T_{water\ average}$.

In table 5.7 the main thermal results are reported.

Table 5.7: *M1 M2 thermal results*

	$P_{W_{in}}$ [bar]	$T_{W_{in}}$ [°C]	$T_{W_{out}}$ [°C]	$T_{max_{mir}}$ [°C]	$T_{max_{chan}}$ [°C]
M1 ($\theta = 0°$)	6	50	93.8	136	121
M2 ($\theta = 5°$)	14	50	104.4	157	136
M2 ($\theta = 0°$)	14	50	99.6	152	134
M2 ($\theta = -12.5°$)	14	50	89.8	146	130

The images in fig. (5.11, 5.12) show the contour plots of the surface temperature at the end of simulation for the mirror M1.

The water temperature increases by 44°C and permits to obtain a maximum temperature on the mirror of 136°C, recorded in the centre of

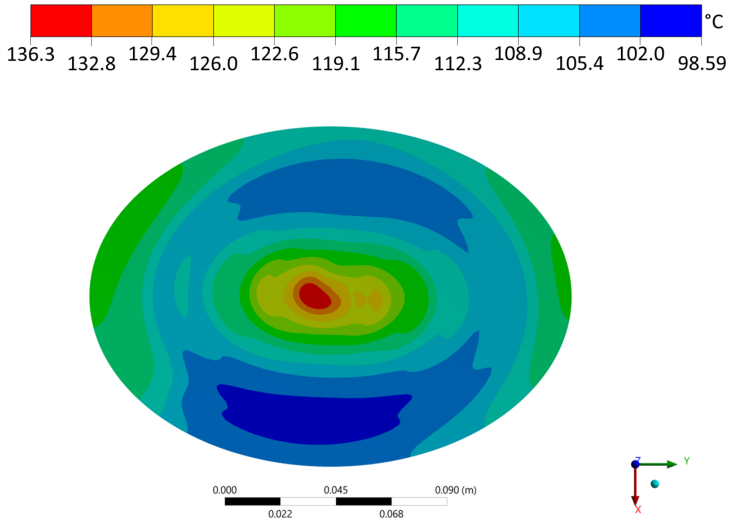

Figure 5.11: *Contour plot of the temperature on the mirror M1 front surface.*

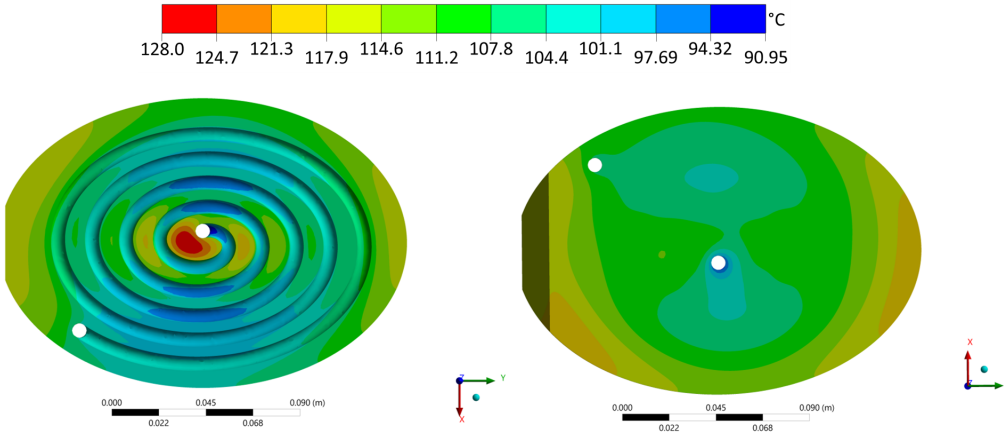

Figure 5.12: *Contour plot of mirror M1 temperature, interlayer view (left) and back view (right).*

the mirror (the most loaded zone of the structure). The maximum temperature over the channel walls is 121.4 °C. This value is highlighted because is relevant to evaluate the required pressure of the water, in order to avoid the evaporation of the fluid near the wall, for the reason explained in section 5.1.6. Subsequently it will be used.

Concerning the mirror M2, as visible in tab. 5.7, the worst orientation is $\theta = 5°$, in which the maximum mirror temperature is observed. This result was expected, because this orientation presents the maximum thermal power to be disposed of (table in fig. 5.6).
The images in fig. (5.13, 5.14) show the contour plots of the surface temperature at the end of simulation for the mirror M2 ($\theta = 5°$).

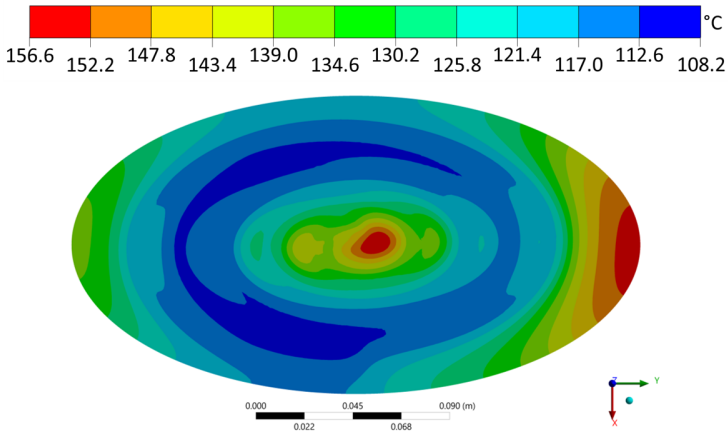

Figure 5.13: *Contour plot of the temperature on the mirror M2 ($\theta = 5°$) front surface.*

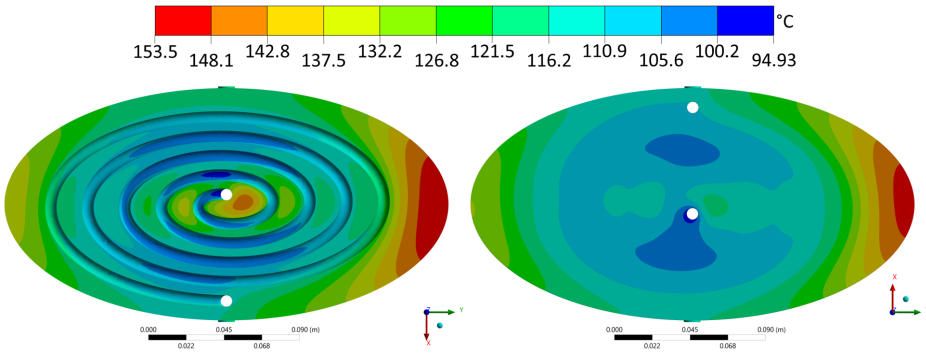

Figure 5.14: *Contour plot of mirror M2 ($\theta = 5°$) temperature, interlayer view (left) and back view (right).*

For the mirror M2 the thermal stresses are higher. The total power to be disposed of is higher than the power of M1 and the distribution of the heat is different, because the heat fluxes of the beam and irradiated

by the plasma hit different surfaces.

The water temperature increases by ∼54°C and the maximum temperature on the mirror is ∼157°C, recorded in the centre of the mirror (the most loaded zone of the structure) and also near the right edge. The maximum temperature over the channel walls is 136 °C, important value for the subsequent evaluations about the pressures.

5.2.5 Definition of the cooling circuit hydraulic parameters

Considering the previous results and the data of the ECRH design group, it has been possible to draw the preliminary conceptual design of the external cooling circuit of the launcher.
The definition of the new cooling circuit hydraulic parameters is the result of an intensive collaboration with the ISTP-CNR ECRH group of Milano.
First of all it is necessary to explain that the preliminary conceptual design of the feeding of M2 is operated by 2 helical pipes for inlet and outlet (fig. 4.5 right). They are necessary to allow to change the orientation of the mirror with minor torques and forces on the mirror drive and the helical pipes. This is why they are so long. The pressure drop inside the pipes is $\sim 7.5\ bar$.
A conservative evaluation the pressure drop in the mirror is done considering a straight tube with equivalent length of the spiral circuit, considering an over-estimation coefficient derived by a comparison with an equivalent "serpentine circuit". The value considered at this stage is 2 *bar* for M2 and M1.
A first estimation of the needed pressure along the feeding circuit has been done.
In M1, considering that the maximum channel temperature is $\sim 120^oC$, in order to avoid formation of steam, the pressure chosen for the outlet is 4 *bar*, with 2 *bar* of margin from the absolute pressure (2 bar) in which the saturation temperature is 120^oC.
The same pressure was chosen for the outlet of the output spiral of M2.
Therefore, considering the pressure drops of the mirrors (inner circuit 2 *bar*) and the pressure drops of the M2 external helical pipes (7.5 *bar* in outlet feeding spiral), the pressure of the water in inlet for M2 is about 14 *bar* and for M1 is about 6 *bar*. Such inlet pressures have been selected to do the thermal simulations shown before.

In figure 5.15 it is possible to see the thermodynamic features of the external circuit.

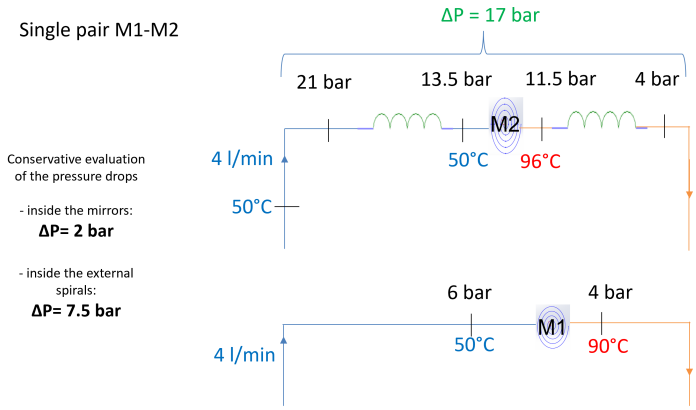

Figure 5.15: *Schematic features of the mirrors cooling circuits.*

5.2.6 Comparison of Unitus - PoliTO thermal results

In chapter 3, FEM tools, the use of FLUID116, convection assumptions and HTC evaluation were presented. It was amply explained that the use of this methodology is very practical and useful in this type of application, especially considering the preliminary design phase the system is in. However, at this stage of the project, a comparison with more accurate CFD analyses, which obviously do not exclude important fluid characteristics, is useful.
So, the following section concerns an activity realized in close collaboration with Politecnico of Torino (PoliTO). In particular, the temperature maps obtained with herein presented thermal simulations, will be confirmed by CFD simulations carried out by PoliTO, the results of which are included in the article [56].
In fig. 5.16 the comparison of the main contour plot results are shown, beyond a comparison of the mesh of M2.

The main result is that the temperatures resulting from Unitus simulations are higher. In the mirror M2 the maximum one is higher by $\sim 4°C$, the minimum ones by $\sim 6°C$ in the top surface and $\sim 9°C$ in the bottom surface. In the mirror M1 the discrepancy of the maximum temperature values is $\sim 6°C$ and the minimum one $\sim 3°C$. The percentage discrepancies are reported in tab. 5.8. Such values show the robustness of thermal

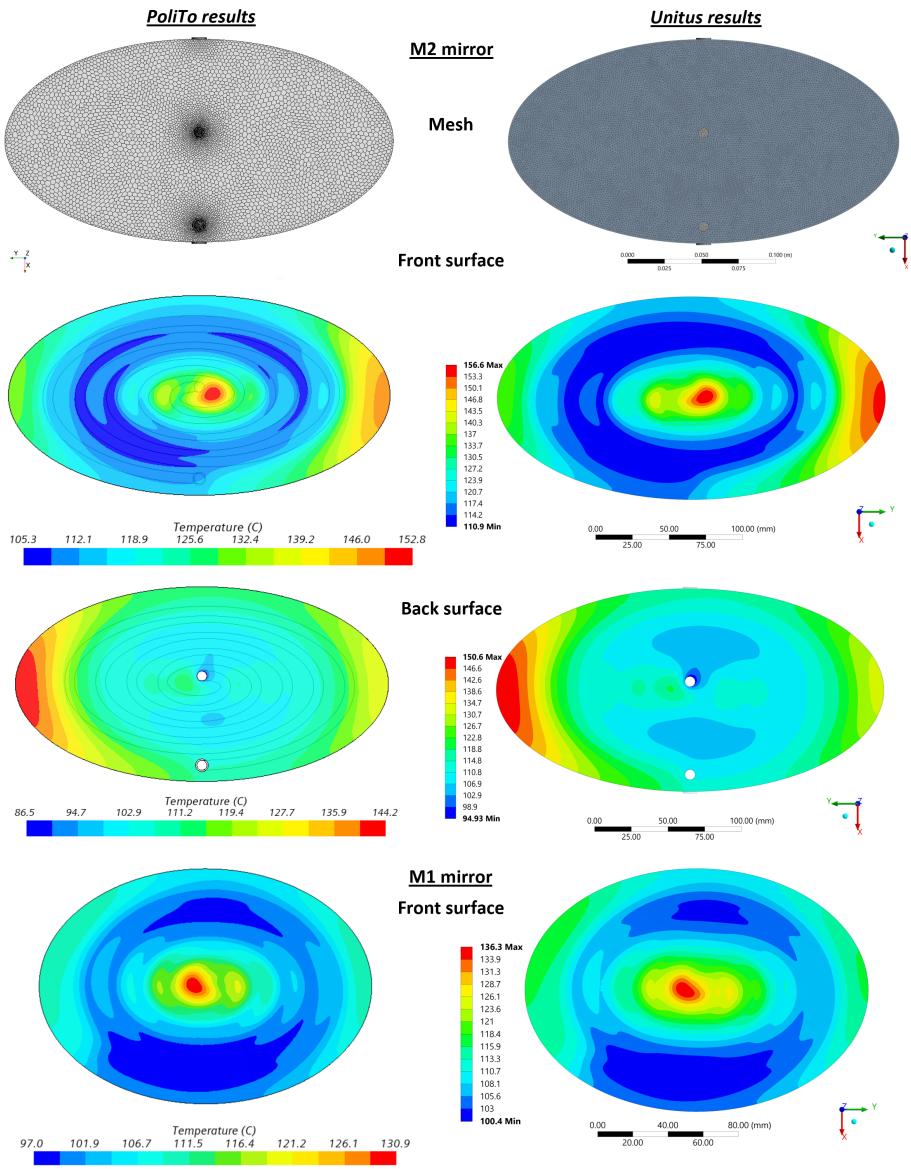

Figure 5.16: *M2 and M1 mirrors: comparison between PoliTO results (left column) and Unitus results (right column).*

results, with percentages within the acceptable engineering limit, not beyond $\sim 5\%$. Besides, the fact that the approximations lead to higher temperatures is good, because produce conservative results.

Table 5.8: *Discrepancy Unitus-PoliTO temperature results.*

$\Delta T_{max}M2$	$\Delta T_{min}M2$	$\Delta T_{max}M1$	$\Delta T_{min}M1$
Front surface			
2.5%	5.3%	4.1%	3.5%

5.2.7 Preliminary structural analysis for mirror M2

The thermal analyses, carried out for the mirrors, had different objectives. First of all the aim to calculate the maximum temperatures reached on the mirrors to ensure to be below the threshold temperature of $200°C$, secondly the aim to establish the features of the water that permits such kind of cooling inside the mirror. But there is another important objective: to ensure that, with the proposed cooling, the mirror strain-induced deformations produce a negligible variation of the beam characteristics.
For this aim, two preliminary thermo-mechanical simulations have been carried out on the mirror M2 ($\theta = 5°$), comparing the Unitus and PoliTO thermal inputs.
The first idea of the mirror support is shown in fig. (5.17). Its material is 316L (N)-IG Stainless steel.

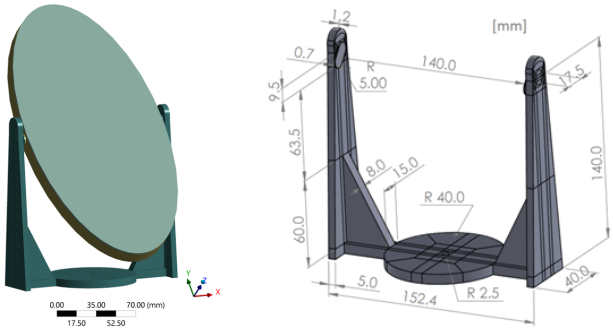

Figure 5.17: *Mirror M2 ($\theta = 5°$) and the first proposal of support (left). Dimensional details of the mirror support structure (right).*

A steady-state thermal analysis has been carried out, in which the thermal constraint is the steady temperature distribution on the mirror. Only conduction between mirror and support-structure is active.
The image in fig. (5.18) shows the thermal results, considering the PoliTO temperature map. The steel structure is well heated and reach an average temperature of 112.4 °C. This temperature will contribute to the support

deformations, in addition to the mirror expansion effect.

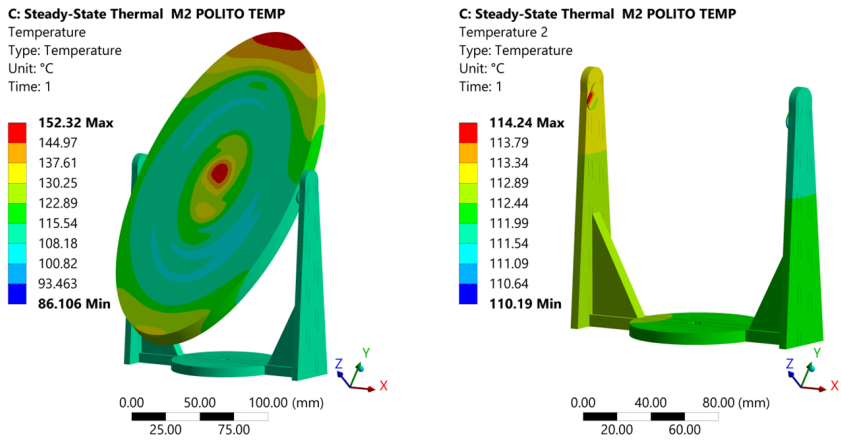

Figure 5.18: *Mirror and support temperature distribution.*

The objective of the structural analysis is to evaluate the mirror deformations. They must produce acceptable variation of the beam characteristics, with a beam deflection as low as possible.
The loads for the structural analyses are:

- Temperatures on the whole structure (mirror + support), coming from:

  A. Unitus mirror temperature maps

  B. PoliTO mirror temperature maps.

- Inner pressure of the water: 14 bar (without considering the pressure drops).

- Continuity of the flow in inlet and outlet.

The structural constraint is:

- Fixed support on the bottom surface of the support-structure of the mirror. (Approximation: The support is simulated bonded with the mirror).

In total, two analyses have been executed, considering the different input temperature map (A. and B.). The results are visible in fig. (5.19) in which the total deformation is shown, with a scale factor of x80.

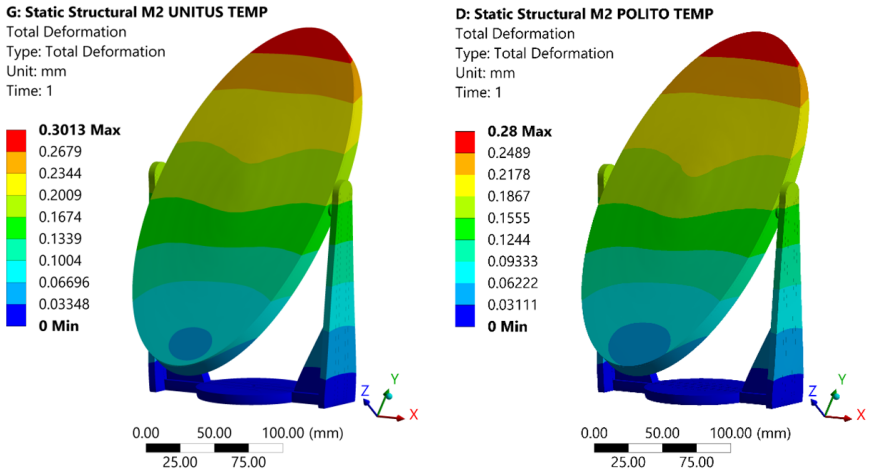

Figure 5.19: *Total deformation (x80) contour map on M2 mirror. (Left) Unitus Temp, fixed base (A). (Right) PoliTO Temp, fixed base (B).*

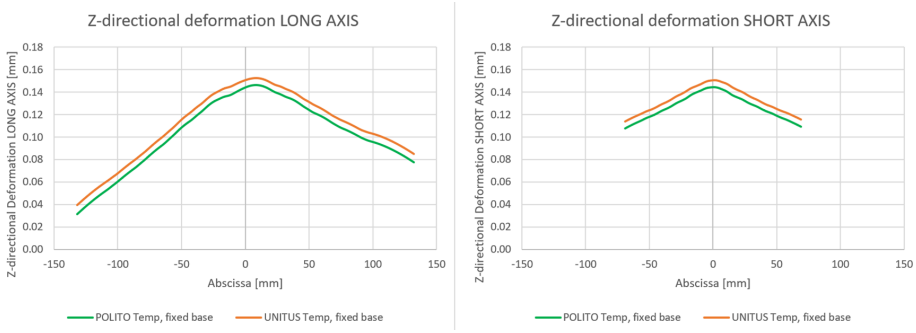

Figure 5.20: *Trends of Z-directional deformation on the long (left) and the short (right) axis of the mirror.*

In fig. (5.20) Z-directional deformations are plotted along the major and minor axes (y and x) of the mirror.

Table 5.9: *Comparison of the values of the maximum total deformation and the Z directional deformation for the cases A and B.*

	Unitus Temp (A)	**PoliTO Temp (B)**
Max Tot Def [mm]	0.301	0.280
Max Z Def [mm]	0.152	0.146

The graphs show the consistence of the results between the input temperature maps. The percentage discrepancy of the maximum total deformation is $\sim 7.5\%$ and of the Z directional deformation is $\sim 4\%$.

The trends of the deformation along the axes are used to extrapolate the curvature radius near the central zone of the mirror, the part in which the beam hits the mirror. The curvature radius is calculated as the radius of the circumference that well fits the trend of the deformation in proximity of the centre.
From the radius and the deformed geometry obtained in this analysis, the ECRH group extrapolated the variation of the beam characteristic, considered negligible. The percentage variation of the minimum beam waist is 4.3% and the variation of the tilt (the angle of incidence of the beam on the surface) is 0.04°.

5.2.8 M1 and M2 mirrors design: intermediate considerations

An update of the mirror M2 cooling circuit design was analysed, and used as inspiration to define the design of the cooling for mirror M1.
Defined the requirements for the cooling of the mirrors (a water inlet temperature of 50°, a volume flow rate of $4l/min$ and a diameter of the cross-section of 7 mm), the cooling channel shape of the mirror M2 was improved and adapted also for the mirror M1. The new conditions brought to the following results. In the mirror M1 the water reaches the maximum temperature of ∼94°C, with a maximum mirror temperature of ∼136°C; the mirror M2 with an outlet water temperature of ∼104°C reaches a maximum temperature of ∼157°C.
Furthermore, thanks to a collaboration with PoliTo, a comparison analysis has been carried out. PoliTo elaborated CFD simulations, starting from the same inputs, on the base of the provided data. The CFD results are consistent with the Unitus thermal analyses, demonstrating that the simplified analyses, with the methodology presented in this thesis, are less accurate, but good, with a percentage discrepancy between the extremal temperatures not higher than 5%. Both temperature maps, Unitus and PoliTO, were used as input for preliminary structural simulations on the mirror M2. The results showed very similar deformation trends between

the two input temperature cases, and for now negligible variation of the beam characteristics after the mirror deformation.

Mirror M2 will be no more treated in this thesis, but the reached results this far are the base of its development, now under investigation, after the arising of some problems. Being a steering and movable mirror, piezoelectric walking drives are foreseen for its movement [57]. The drives have got a low driving force. This is a problem in the environment in which the mirror is, with very high magnetic fields and torques due to the their interaction with the currents induced on the conductive surface of the mirror because of variable magnetic fields, as those induced for plasma control, and especially in case of disruption events. Studies, reported in [58], have proven the currently proposed Cu-Cr-Zr mirror could be critical for its low electrical resistivity. Therefore different solutions are under evaluation as that ones proposed in [58] and analysed and reported in [56].

The mirror M1, instead, being fixed, doesn't present the same problems of M2. Other configuration, in parallel with M2, are studied in [56], but an evolution of the spiral design seems to be the most promising solution. For this reason the next section presents an improvement of its design.

5.3 M1 mirror design improvement

The evolution of the mirror M1 design comes from the necessity to improve the thermal condition obtained with the preliminary design. The geometry and the channel shape are now being studied.

The requirement driving the new design choices is to decrease the maximum temperature reached on the mirror. The way to achieve this objective is to improve the cooling performance by re-arranging the cooling channel shape to better cover the entire mirror surface.

The activity was performed using the CAD software SolidWorks to realize different CAD models to be compared. The methods are the same as those used so far: the FEM tools explained in section 3.1, the assumption about the heat exchange in section 3.2, and the loads reported in section 3.3 and 5.2.3.

5.3.1 Starting assumptions

As visible in section 5.2.4, in fig. 5.11, the edges of the mirror M1 (both left and right) present higher temperatures because the cooling channel does not cover the whole mirror area as well as it could. In addition, the central area records the maximum temperature. Both situations can be improved by ensuring that cooling water flows through a larger area of the mirror (even in the centre). So, it is possible to improve the spiral sketch, increasing the pitch along the major axis and better cooling the central area, where the temperature peak is recorded.

5.3.2 CAD modification and proposals

Three configurations have been realized and compared to individuate the best one from the thermo-structural point of view.

5.3.2.1 Modification of the central area

The first step concerns the change of the central area, chosen from three different possibilities:

- Continue the spiral shape: the current range of the spiral is $\pi < \theta < 10.25\pi$. A new range can be considered: $\frac{3}{4}\pi < \theta < 10.25\pi$. But in this case a problem immediately arises: the extruded cut overlaps itself, so such option has to be discarded.

- Continue with the sketch of a straight segment of length 0.01 m inclined by $\pi/6$ *rad* with respect to the long axis. Here too, a problem immediately arises: the junction between spiral and segment is too severe.

- Continue with an arc of circumference of $\pi/2$ *rad*: it is enough long, and the junction is soft.

The final choice is the spiral elongated towards the centre by an arc of circumference with a 90° angle.

5.3.2.2 Modification of the spiral equation

The second step concerns the change of the spiral equation. The three different solutions are:

a) The y standard pitch of the spiral is increased from 11.50 mm to 12.55 mm. This new value of pitch is obtained drawing a new channel tangential to the old one in the point with $\theta = 9.5\pi$ (the highlighted black circle in fig. **??**). The first new configuration has a constant pitch and is zoomed on the y-axis. It is called $P_{y_{Zoom}}$.

b) The x-pitch is decreased from 11.5 mm to 10 mm. The y-pitch is changed from constant to variable. It allows an increase in standard pitch of 1.78 mm per revolution. The second new configuration is called P_{y_V}.

c) The spiral is the same as in the P_{y_V} configuration but translated. This produces a more symmetrical channel. The third new configuration is called $P_{y_{VT}}$.

The three configurations are reported in fig. (5.21).

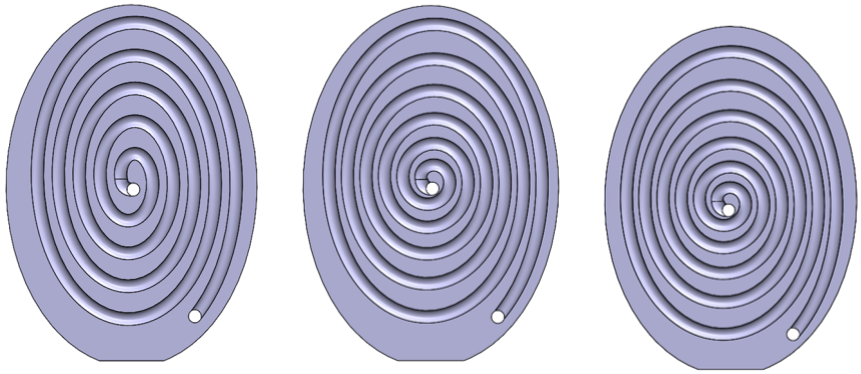

(a) $P_{y_{Zoom}}$ **(b)** P_{y_V} **(c)** $P_{y_{VT}}$

Figure 5.21: *a) Configuration Constant and zoomed pitch ($P_{y_{Zoom}}$). b) Configuration Variable pitch (P_{y_V}). c) Configuration variable pitch and translated spiral ($P_{y_{VT}}$)*

In configuration a) Py_{Zoom}, the external parts of the mirror are more covered by the cooling channel, but the new pitch makes spiral turns more distant from each other, especially near the centre, which is the most loaded zone. So, configuration b) is created to solve the problem: if the spiral shape has to be "wider" on the long axis and denser in the middle (where the heat flux is higher), a variable y-pitch can be used to cover the entire area of the mirror and a lower x-pitch to thicken the channel in

the central area. The configuration c) provides a spiral as symmetrical as possible on the mirror area, through a translation of the configuration b). These configurations have been tested in steady-state thermal and static structural analyses to determine, through a comparison analysis, which would be the best in terms of temperature (first) and deformation.

5.3.3 Thermal analyses

Preliminary thermal analyses have been performed to provide a general comparison. The purpose is to individuate which configuration guarantees the lowest temperature of the mirror (average and maximum).
A preliminary mesh sensitivity analysis has been carried out. The elements number of the final mesh is 992367 with a maximum element size of 1.3 mm for the cover layer and 1.4 mm for the mirror bulk.
Thermal conditions of the first analysis foresee the following inputs:

- Heat loads presented before: neutronics irradiation, radiative irradiation and microwave power absorption.
- Volume flow rate: $\dot{V} = 4l/min.$
- Water inlet temperature $T_{water\ inlet} = 50°C.$
- Water inlet pressure: $p_{water\ inlet} = 6\ bar.$
- Heat transfer coefficient: $h \cong 20000\ W/(m^2K)$, constant, calculated considering the water properties at $T_{water\ intel}$.

In this phase of comparison among configurations, it is sufficient to conduct analyses with only one iteration, in which the HTC is evaluated considering the water properties at the initial condition of the water. Once the final configuration will be found, an analysis with iteration will be carried out.

In fig. (5.22) the contour plots of the temperatures are shown for all the configurations. In tab. (5.10) the maximum temperature and the average temperature are reported. Regarding the maximum temperature, the best result is that one with a variable pitch along the y axis but not translated. However, as foreseen, a better distribution of temperature is found for the mirror with translated spiral; in fact, the mirror without translation shows a higher temperature in the area far from the cooling

channel and the average temperature is lower in $P_{y_{VT}}$ configuration. It is visible that the first configuration $P_{y_{Zoom}}$, the one with the y zoomed pitch cooling channel, is not suitable.
However, only the thermal results are not enough to choose a better configuration, so the next step is to use the thermal solutions to assess the structural deformation.

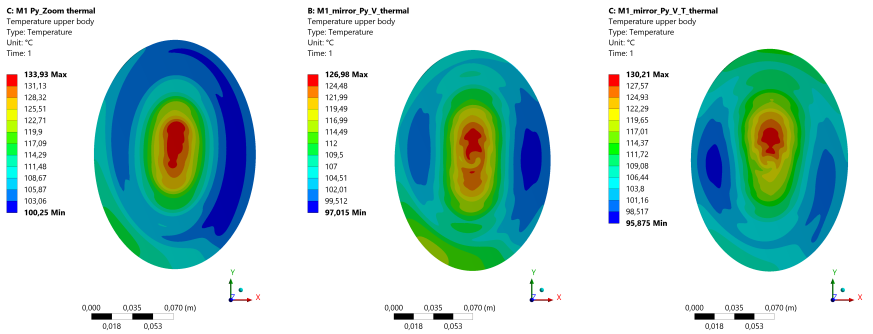

(a) $P_{y_{Zoom}}$ **(b)** P_{y_V} **(c)** $P_{y_{VT}}$

Figure 5.22: *Comparison of thermal results on the upper surface.*

Table 5.10: *Results of maximum and average temperatures in the comparison among M1 different configurations.*

	$P_{y_{Zoom}}$	P_{y_V}	$P_{y_{VT}}$
T max [°C]	134	127	130
T average [°C]	108	106	105

5.3.4 Structural results

Concerning the structural support, in this phase, in which the realistic one is not defined, it was decided to implement a very simple support in simulation. Two discs were modelled at the edges of the mirror, at the short axis. This solution will not be the definitive one, but it is functional for comparing the configurations. The external faces of the discs have been completely fixed in all directions.
The other inputs for the structural analyses are:

- Imported thermal load, every mirror has its own temperature distribution.

- Pressure: flowing water inside the cooling channel: 6 bar.

- Continuity of the flow in the inlet and outlet.

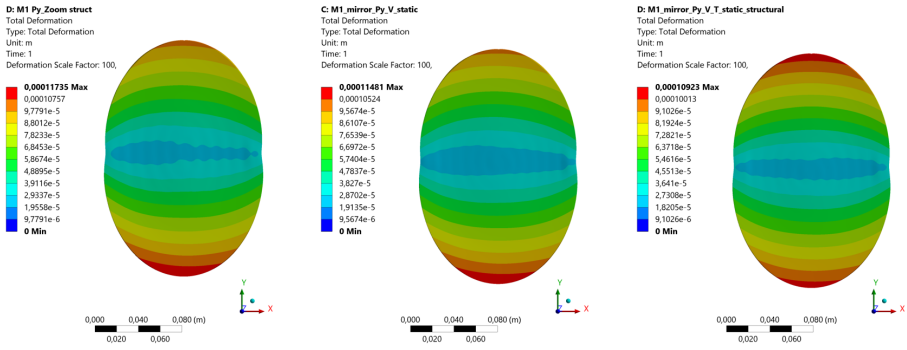

(a) $P_{y_{Zoom}}$ **(b)** P_{y_V} **(c)** $P_{y_{VT}}$

Figure 5.23: *Comparison of contour plots of total deformations.*

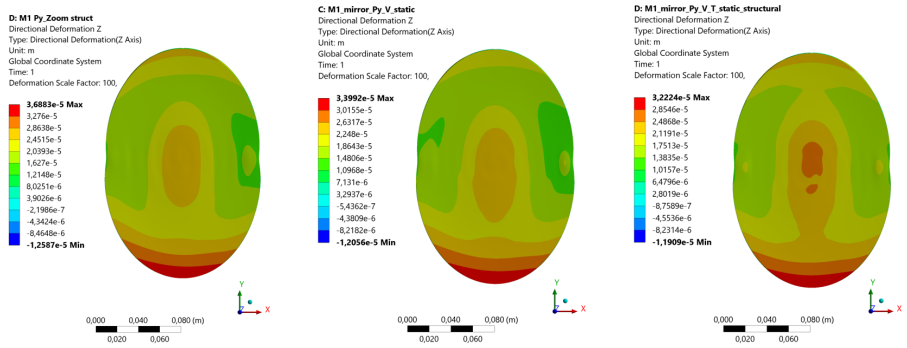

(a) $P_{y_{Zoom}}$ **(b)** P_{y_V} **(c)** $P_{y_{VT}}$

Figure 5.24: *Comparison of contour plots of Z directional deformations.*

Table 5.11: *Results of Max Total deformation and Z deformation for three configurations.*

	$P_{y_{Zoom}}$	P_{y_V}	$P_{y_{VT}}$
Max Tot Def [mm]	0.117	0.115	0.109
Max Z Def [mm]	0.037	0.034	0.032

As visible from the tab. (5.11) and the figures in fig. (5.23- 5.24) the lowest deformations (total and Z directional) are recorded in the $P_{y_{VT}}$ configuration. Besides, as shown in fig. (5.23 c) the total deformation is more symmetrical in the third configuration.

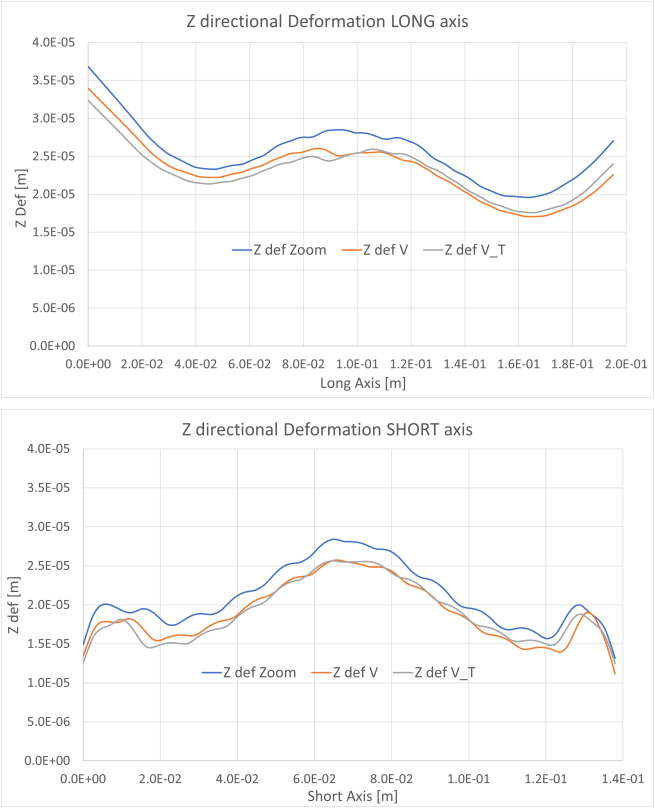

Figure 5.25: *Comparison of the Z deformations on the long and short axes for all the configurations.*

Looking fig. (5.25), reporting the trends of the Z directional deformation along the major and minor axes, it can be noticed that "$P_{y_{Zoom}}$" configuration isn't suitable, the Z-deformation is always higher than the other configurations. Instead, the "P_{y_V}" and "$P_{y_{VT}}$" configurations show a similar trend, but the variable pitch and translated configuration presents the absolute minimum values of Z-deformation.

Interesting to note that the graphics, especially the short axis one (fig. 5.25 right), are really "indented"; the only pressure inside the channel is

not enough to explain this behaviour, because the pressure contribution to the deformation is two orders of magnitude lower than the temperature one ($10^{-7}m$). This is caused by the interaction between temperature stress and fixed support. Yet, as previously said, the fixed support is not definitive but only the same one for all configurations for a comparative analysis.
Considering these results, the final choice about the configuration is the third one: $P_{y_{VT}}$ variable pitch and translated. The geometrical details of the cooling channel shape are now reported. The path has the following geometrical definitions:

$$\begin{cases} x(\theta) = 5cos(\theta) - 2 \ \ [mm] \\ y(\theta) = -5sin(\theta) - 0.3 \ \ [mm] \\ \pi/2 < \theta < \pi \ \ [rad] \end{cases} \tag{5.3}$$

$$\begin{cases} x(\theta) = \frac{10}{2\pi} \cdot \theta cos(\theta) - 2 \ \ [mm] \\ y(\theta) = -\frac{(97.6)}{69} \cdot \frac{0.1 \cdot (\theta - pi) + 7}{2\pi} \cdot \theta sin(\theta) - 0.3 \ \ [mm] \\ \pi < \theta < 12.3\pi \ \ [rad] \end{cases} \tag{5.4}$$

The equation 5.3 is for the circular path in the centre of the mirror.
The equation 5.4 is for the spiral path.
Now, with the best configuration, it is possible to elaborate an iterative analysis to individuate the outlet temperature of the first iteration and then, with it, calculate the HTC at an average water temperature.

5.3.5 Complete final analysis

Only three iterations are sufficient to reach the convergence on the maximum temperature and on the outlet water temperature values. The final analysis is equal to the previous one, with the only difference about the HTC:

- Heat transfer coefficient (HTC): $h \cong 23000 W/(m^2 K)$, constant, calculated considering the water properties at $T_{water\ average}$.

As visible in Fig. (5.26) and tab. (5.12), all the results of the third iteration are in line with what is expected: temperatures and deformations are lower than the first iteration.
Thermal conditions were improved compared to the starting configuration of the cooling channel. In particular, the maximum temperature decreases from 136 $°C$ to 124$°C$, more than 12$°C$ with $\sim 9\%$ of improvement.

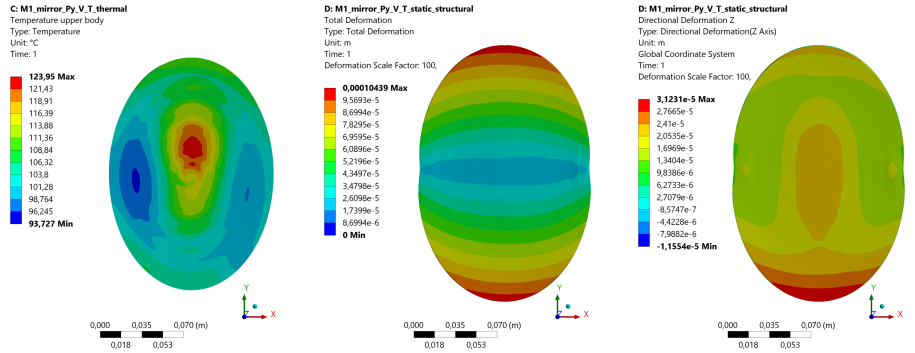

(a) $P_{y_{Zoom}}$ **(b)** P_{y_V} **(c)** $P_{y_{VT}}$

Figure 5.26: *Thermal and structural results of the last iteration, for the configuration* $P_{y_{VT}}$.

Table 5.12: *Thermo-structural results of the last iteration, for the configuration* $P_{y_{VT}}$.

Max T all	T water out	Max Tot Def	Max Z Def
$124°C$	$94°C$	0.104 mm	0.031 mm

5.3.6 M1 mirror design improvement: final considerations

The last activity about the launcher mirrors concerned the improvement of the mirror M1 design. Three different configurations of the cooling channel have been studied with thermo-structural analysis, to individuate a solution good to decrease the maximum temperature of the mirror and produce a more uniform cooling. First thermal analyses showed that two solutions were better than the other one. Structural analyses, instead, permitted to individuate the best one. The cooling channel was improved with an extension of the channel in the central zone and with a modification of the spiral path, built no more with a constant pitch, but variable, that permits to have thicker turns in the central zone, but at the same time a wider extension on the mirror surface.
The maximum temperature recorded on the mirror with the new configuration is $\sim 124°C$, with an improvement of $\sim 12°C$.

5.4 Summary and conclusions about DTT Launcher mirrors

In this chapter the DTT launcher mirrors M1 and M2 were studied. The project started with a preliminary study of the movable mirror M2. Different configurations of its cooling channel were compared through thermal simulations, analysing the maximum temperatures reached on the mirror. A channel with the shape of an elongated spiral with constant pitch on y-axis resulted the most efficient to dissipate the heat coming from the thermal loads, to which the mirror is subjected. On the first design a study of the trends of the temperatures as function of the cooling parameters (as water inlet temperature and volume flow rate) was elaborated. The worst studied scenario brought to a maximum mirror temperature of $138°C$.
Then, an update of the mirror M2 cooling circuit design was analysed, and used as inspiration to define the design of the cooling for mirror M1. Defined the requirements for the cooling of the mirrors, thanks to the work of the DTT researchers, considering a new water inlet temperature of 50°, a volume flow rate of $4l/min$ and a diameter of the cross-section of 7 mm, the cooling channel shape of the mirror M2 was improved and adapted also for the mirror M1.
The new conditions brought to the following results. In the mirror M1 the water reaches the maximum temperature of $\sim 94°$, with a maximum mirror temperature of $\sim 136°$; the mirror M2 with an outlet water temperature of $\sim 104°$ reaches a maximum temperature of $\sim 157°$.
Thanks to a collaboration with PoliTO, a comparison between thermal simulations and their CFD simulations has been executed. It demonstrated that the simplified analyses, with the methodology presented in this thesis, are less accurate, but good, with a percentage discrepancy between the extremal temperatures not higher than 5%.
Instead, preliminary structural analyses on the mirror M2 confirmed negligible variation of the beam characteristics after the mirror deformation. Such design of the mirror M2 became the base of its new development.
The mirror M1, instead, was developed with an evolution of the spiral channel design. The cooling channel was improved with an extension of the channel in the central zone and with a modification of the spiral path, built no more with a constant pitch, but variable, that permits to have thicker turns in the central zone, but at the same time a wider extension

on the mirror surface. The maximum temperature recorded on the mirror M1 with the new configuration is $\sim 124°C$, with an improvement of $\sim 12°C$.

The studies herein presented are reported totally or in part in the journal publications [52], [48] and [56].

Chapter 6

DTT MBTL mirrors

The studies about the ECRH mirrors continue with the conceptual design of the mirrors of the Transmission Line. So, going backwards in the ECRH system, now the focus shifts to the central part: the line. The first part of the work will concern the MBTL internal to the corridor (nearest to the torus hall), whilst the second one external to the corridor (nearest to the ECRH building) (fig. 4.2).
At this stage, two important steps are taken, which move the design to a more detailed level.
The first one concerns the implementation of transient analyses, so as to study the evolution of the mirror behaviour during the RF pulse and the dwell time between two pulses.
The second one concerns the structural analyses that now, assume an important role in the development of the mirror design. The study of the mirror deformation it is more important in the line. Here, indeed, the mirrors have to be more efficient in terms of optical performance, because a deflection of the microwave beams in this area has more severe consequences at the end of the line. The beams deflection produces power losses (spillover and coupling [21]), that repeated in each mirror of the line (a line in DTT can count also 80 mirrors [59]), could overcome the acceptable limit on losses.
In the MBTL the reflection of the eight microwave beams on the mirror surface leads to heating of its whole structure due to the absorbed fraction of the beam power (0.21% – 0.27%) due to ohmic heating at the mirror surface. During the radio-frequency power pulse, the mirror temperature increases, generating deformations, that could result in a loss of beam

transmission efficiency. For this reason, these mirrors need to be carefully designed from thermal and structural points of view, to guarantee the required optical performances.

6.1 MBTL mirrors "Step 0"

The mirrors of the multi beam transmission line are similar to the launcher mirrors, but bigger and above all they are subject to higher beam power, but, being out of the machine, not subjected to the irradiation from the plasma.
The "step 0" is a preliminary step that permitted to give a first indication to the new part of the project. It foresees a study of the new thermal load applied to a new kind of structure. In order to have an idea of the effect of the load in time, some simulations have been carried out. They didn't foresee an active cooling in the mirror bulk and the only way to distribute the heat was the conduction inside the mirror and the support. A support structure with a fixed ambient temperature was included in the simulation to study the effect of a cooled external element to extract heat from the front surface. Fig. 6.1 and 6.2 show the results of a transient thermal analysis of a mirror in Copper and Stainless Steel and a mirror in Aluminium at an initial temperature of $30°C$ subjected to 3 pulses of microwave beams in 3 hours. The thermal load is characterized by 8 beams, each one transmitting 1MW of power to the plasma. The total absorbed power by the mirror is 25.2 kW in the case of reflection on copper and 32.4 kW in the case of aluminium.

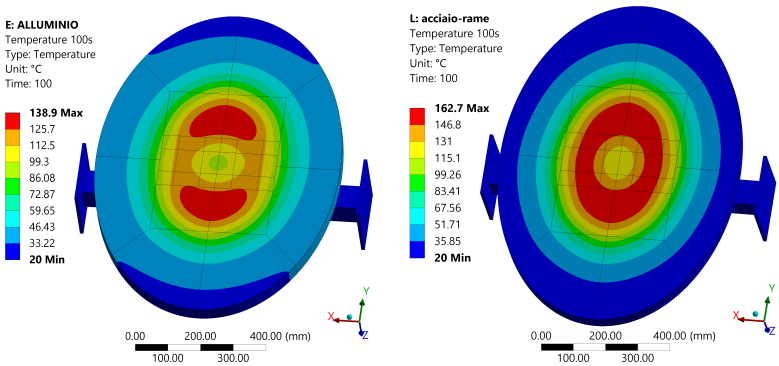

Figure 6.1: *Contour plots of the temperature on two different mirrors at time of 100 s for two "step 0" configurations.*

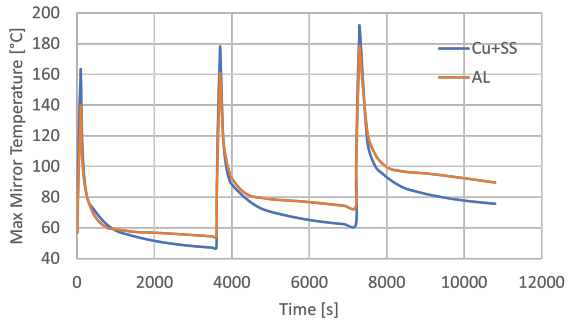

Figure 6.2: *Graph of the trend of the temperature during 3 shots for two "step 0" configurations.*

The most important result of the step 0 is that an active cooling is necessary, because although the maximum temperature after the first shot was acceptable (it is very high anyway), its increase with each subsequent pulse would be unacceptable. After only three pulses, the maximum temperature reaches about 200°C.

6.2 MBTL Parabolic mirror design

After the first indications given by the "step 0" analysis, the design of the first mirror of the MBTL could start. This work was at the basis of an article submitted to the journal *Fusion Engineering and Design*.

The TL power handling requirements include the flexibility to increase the power up to 1.5 MW, considering a future upgrade of the gyrotron power [48]. The RF pulse is expected to be active for 100 s continuously with a repetition rate of one pulse per hour [48]. As already seen in "step 0", the mirrors must be cooled.
The following sections will describe the preliminary design of the MBTL parabolic mirror and its cooling channel, resorting to a coupled thermal and structural finite element (FE) simulation. The presented preliminary analyses will concern the choice of materials, the design of geometries of both mirror and cooling channel, and the thermo-fluid dynamic water parameters.
The design will be driven by the minimization of the mirror deformations, which is strictly related to the minimization of temperature values and

gradients as well. This is important to guarantee high efficiency of beam reflection, reducing power coupling losses as much as possible. Before explaining the activities and the achieved results, it is important to point out the initial assumptions, coming from the system requirements and the work performed by the DTT ECH design group of ISTP-CNR.

6.2.1 MBTL Parabolic mirror assumptions

The mirror under analysis has an elliptical shape, it is a focusing mirror, with a parabolic curvature.
The elliptical dimensions come from optical requirements. In particular, the minimum radius depends on the beam size, the wavelength, the distance between the beams, and the distance between the focusing mirrors, as explained in [50].
Fig. 6.3 shows the geometric configuration with the minor and major radii calculated in 380.0 mm and 537.4 mm respectively. It is rotated 45° with respect to the direction of incidence of the beams (incidence angle $\theta_i = 45°$). The parabolic curvature is given by a cut of the flat mirror with a paraboloid that has the revolution axis rotated by 45° with respect to the major radius of the mirror (fig. 6.3 right).

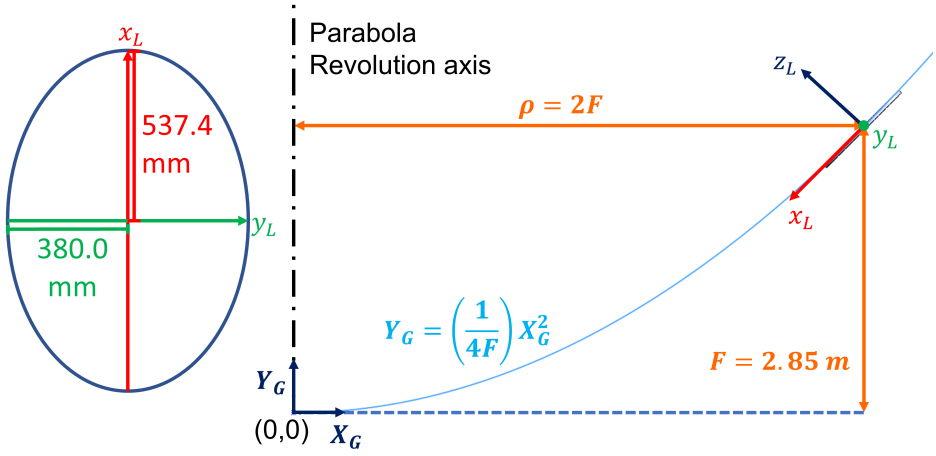

Figure 6.3: *Representation of the parabolic mirror features. On the left the elliptical shape with radii dimensions. On the right the representation of the parabola generating the mirror paraboloid surface. F is the focal length. Subscripts L and G on the reference systems stand for "Local" and "Global".*

The planar distances between the paraboloid vertex and the centre of the mirror are the focal length (F = 2.85 m) on the vertical and a length of $\rho = \frac{F}{cos^2(\theta_i)} = 2F$ on the horizontal [18]. The generatrix parabola has the following formulation:

$$y_G = \frac{1}{4F} x_G^2 \tag{6.1}$$

with the vertex on the origin of the global (G) reference system. If the vertical distance of the mirror centre from the origin is F, the horizontal distance is 2F.

During the 100 s of the pulse length, a MBM must simultaneously reflect on its surface 8 beams. Ideally, at the input plane of the MBTL, the centres of the beams are disposed on the vertices of an octagon (as shown in Fig. 6.4 left). Being the mirror non-planar but inclined at 45° and placed 5.7 m (2F) away from the input plane, the reflected beams are not covering an octagonal area, but rather a quasi-elliptical area, as shown in Fig. (6.4) right.

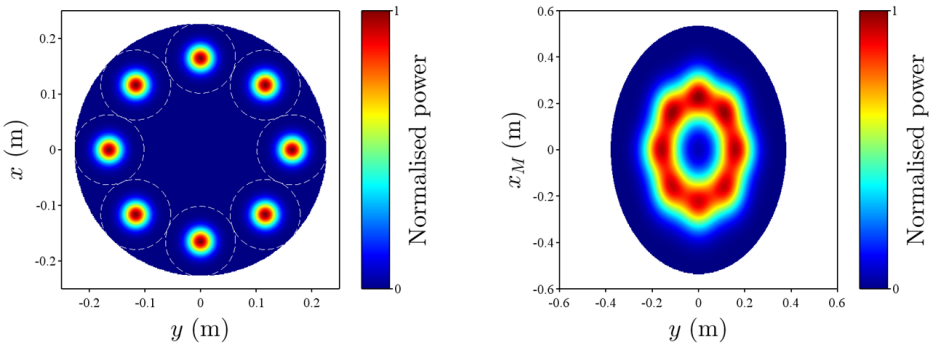

Figure 6.4: *Left: Power distribution of 8 Gaussian beams at the theoretical input plane of MBTL. Right: Power distribution of 8 beams at first non-planar mirror inclined by 45° and placed 5.7 m away from input plane. The power distribution is largest for the topmost beam, because this beam has the shortest path from the input plane. The figures are from [48].*

Being inside a vacuum envelope, far from the plasma, the only load incident on the mirror is the absorbed fraction of the microwave beams power. It is a surface load, defined considering a Gaussian distribution as described in section 3.3. The absorbed power density per single beam is

calculated with equation 3.3 and 3.5.
In this case, the total power of a single gyrotron beam is chosen considering the maximum possible power unit Q=1.5 MW. In these mirrors the coordinates x_L and y_L of the local system on the mirror (Fig. 6.3, left)) are aligned with the major and minor mirror semi-axes respectively. The absorption coefficient is evaluated considering parallel polarization on the reflective materials (eq. 3.7), material resistivity calculated at ambient temperature, and a roughness factor of 1.3 [36].

Overall, the microwave absorbed power is 25.2 kW in the case of copper and 32.4 kW in the case of aluminium reflection. In Tab. 6.1 the parameters for the load calculation are reported, whilst the image in Fig. 6.5 shows the 3D representation of the absorbed power as a function of the coordinates x_L and y_L.

Table 6.1: *Microwave load parameters.*

	$w_x[m]$	$w_y[m]$	$P_{abs\ MAX}[MW/m^2]$	**A**
Cu	0.15040	0.10635	0.14329	0.21%
Al	0.15040	0.10635	0.18422	0.27%

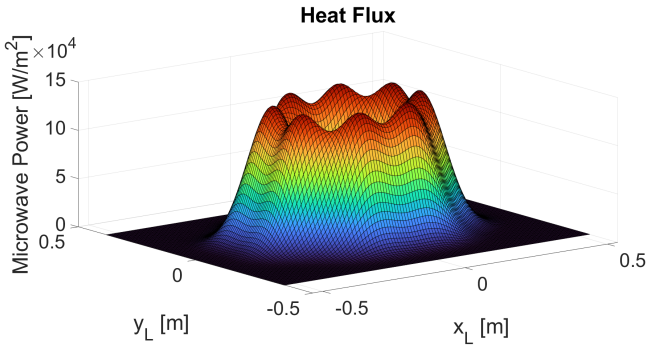

Figure 6.5: *3D Representation of the absorbed power density distribution.*

The fig. 6.6 show the beams centres coordinates.

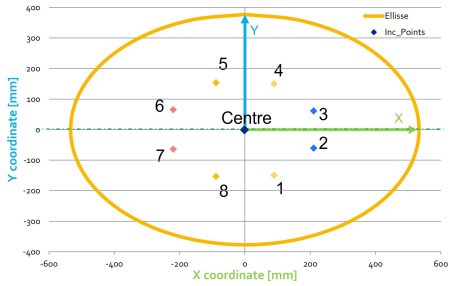

Beam	x [mm]	y [mm]	z [mm]
b1	89.706	-150.308	1.660
b2	210.969	-61.310	1.635
b3	210.969	61.310	1.635
b4	89.706	150.308	1.660
b5	-88.314	153.665	1.697
b6	-219.077	64.669	1.725
b7	-219.077	-64.669	1.725
b8	-88.314	-153.665	1.697
Centre	0.00	0.00	0.00

Figure 6.6: *Beams Centres Coordinates, graph (left) and table (right).*

6.2.2 Numerical modelling

The transient thermal analyses are aimed to simulate the variation of the temperature on the mirror during the RF pulse, but also between two pulses (time interval 3600 s), in which the mirror should return close to the initial temperature. The theoretical approach for the thermal analysis is always the same used so for (section 3.1). Software ANSYS was used using both interfaces Workbench and M-APDL, the second one, to have more accurate results in specific conditions.
The use of convection and the choices associated with it are explained in section 3.2. But, in these new analyses, the HTC is considered constant not only in space, but also in time, despite the performed analyses are transient. Nevertheless, this is a conservative approximation resulting in a small overestimation of the maximum temperature. Moreover, from the results it will be shown that the range of the water temperature is not too large, so the variability of the HTC, caused by the transient condition of the water, is limited. For the same reason, the HTC will be evaluated with water properties referred to inlet temperature.

6.2.3 Definition of different mirror models

To find the best configuration that limits as much as possible the deformations, a comparison among different designs has been firstly performed. The models differ in both geometry and material.
The first option considered for the material (as shown in [48]) is aluminium, which allows reducing weight and costs as well. As cons, it cannot be directly cooled with water for corrosion problems, thus requiring a

separate cooling channel.
Instead, the separate channel isn't necessary in the case of the second option with Stainless-Steel (SS) mirror coupled with a copper layer. It is characterized by lower power to be dissipated thanks to lower electrical resistivity of copper (resulting in lower ohmic losses), but on the other hand, it leads to larger weight and lower thermal conduction in the bulk. The second option is more similar to the configuration adopted in W7-X [27].
A further option considered is a heavier only copper mirror, whose advantages are those of the copper in addition to the possibility to improve the cooling channel.
In the following section, the models are presented more in detail.

6.2.3.1 Aluminium Design

The first design concerns an aluminium (Aluminium Alloy 6061-T6) mirror with a minimum thickness of 3 cm (the curvature of the paraboloid produces a variable thickness; the minimum is in the centre of the mirror). Due to the corrosion problem of the aluminium in contact with water, the cooling channel is realized inside a plate of copper, joined to the back surface of the mirror.
It is an elliptical plate of 50 cm x 40 cm (diameters) with a thickness of 2 cm. The cooling channel is a duct of elliptical shape with a circular cross-section of 1 cm in diameter. It is drawn on the ellipse containing the imprints of the beam centres. The geometry is visible in Fig. 6.7. The total weight of the mirror and the plate is $\sim 87kg$.

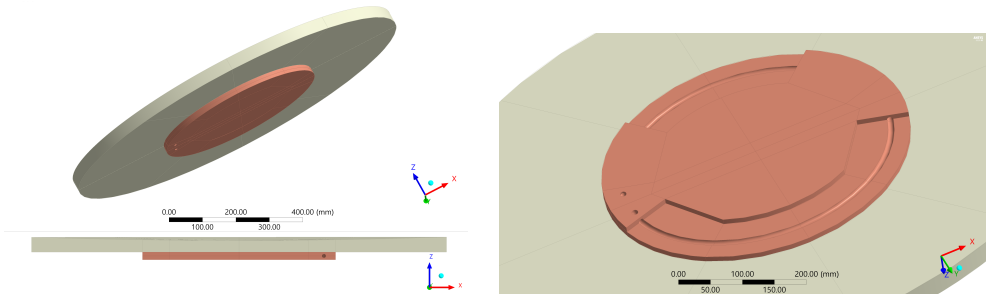

Figure 6.7: *Aluminium mirror geometry. (Top) General view. (Middle) Section view. (Bottom) Details of the dug elliptical plate. It is partially open to appreciate the channel.*

6.2.3.2 SS-Cu design

The second design foresees different materials and different geometry. In this case the mirror has a minimum thickness of 3 cm (at the centre) with a stainless-steel bulk (2.5 cm of constant thickness) and an upper layer of copper with a minimum thickness of 0.5 cm (Fig. 6.8). The SS base is dug similarly to the copper plate of the aluminium mirror, but in this case, the channel has a semi-circular cross-section, being placed between the two materials. The position of the channel is translated closer to the reflection surface and consequently, near to the thermal load, considering the possibility to dig the channel into the SS surface and then add the copper layer by electroforming or other joining methods. To have approximately the same cross-section area as the previous case (circular section with 1 cm of diameter), it is necessary to build a semi-circular section with a diameter of 1.4 cm. This mirror has a total weight of 181 kg (55 kg Cu and 126 kg of Stainless-Steel).

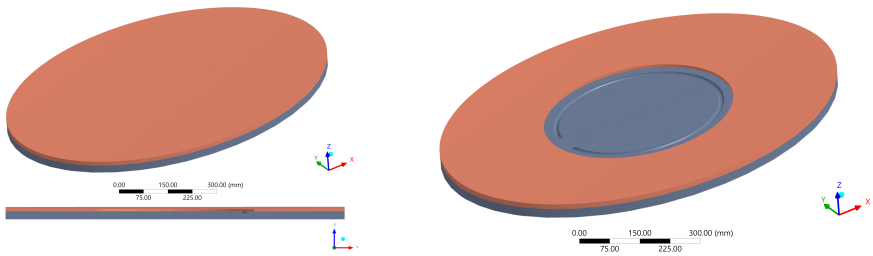

Figure 6.8: *SS-Cu mirror geometry. (Top) View of the superior surface. (Middle) Section view. (Bottom) View of the superior surface with the dug elliptical circuit. The cover layer is partially open to see the channel.*

6.2.3.3 Copper Design

The third design considers a new configuration and material. It is proposed to try to: 1) decrease eventually high temperatures, 2) improve the cooling and 3) homogenize the temperatures. To pursue these objectives, copper could be better than the previous materials from different points of view: it has a lower microwave absorption factor, higher thermal conductivity and lower thermal expansion coefficient (with respect to Aluminium). The cons are the cost and the weight.
As for the steering mirror M2 of the ECRH launcher [52] and for the TL

mirrors of W7-X [27], it is possible to realize a spiral cooling channel to increase the cooling effect. This could produce a more homogeneous distribution of the temperature and a decrement in the maximum values, pursuing all objectives 1), 2) and 3)), provided that the channel covers a great part of the area of the mirror. This means realizing a plate as large as the mirror, but at this point the aluminium becomes unnecessary, and a full copper mirror becomes the next choice.
The concept of the spiral is interesting because it allows a more uniform distribution of heat across the mirror, bringing the water in contact with a larger area, and promoting heat exchange from the most heated to the less heated mirror regions. To this aim, the inlet of the channel is located near the maximum heat flux radius: so that the coldest water is in contact with the hottest zone of the mirror. From the inlet, two different spirals start, the first one towards the centre of the mirror and the second one towards the outside of the mirror, so the mass flow rate is divided into two channels (Fig. 6.9).

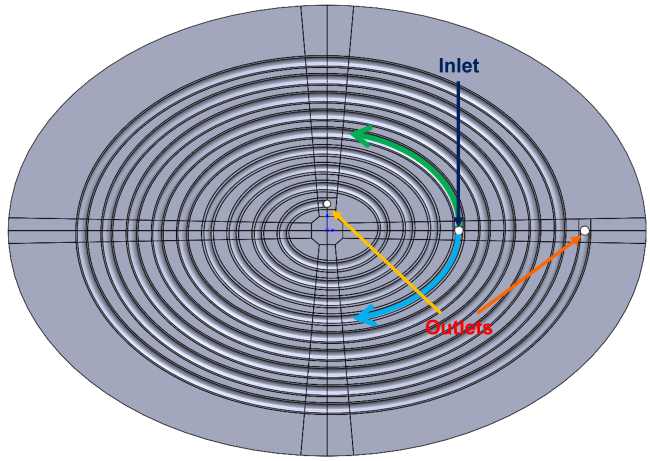

Figure 6.9: *Copper mirror geometry with hollowed-out channels and the holes of the inlet and of the internal/external outlet.*

In this case, the structure is composed of a copper base/bulk, dug with a semi-circular section channel, and covered by a parabolic layer of copper. The total minimum thickness is 2 cm, with a minimum thickness layer of 3 mm. The diameter of the semi-circular section is equal to the previous one: 1.4 cm.
The shape of the channel is an elongated spiral that follows the elliptical

shape of the mirror. The spiral pitch is 3 cm for the minor axis and for the major axis 3 cm multiplied by the ratio between the ellipse radii. The angular range of the spiral is $3\pi \div 20.5\pi$.
The CAD realization of the spiral path, with its particular features will be discussed and explained in section 6.4.1.1.

6.2.4 Thermo-structural simulations, inputs, and results

Thermo-structural analyses are the basis on which the search for the best model is developed. In the following sections, the main results for all the simulations are shown, starting from the input conditions. For each design proposed in Sec. 6.2.3, the transient thermal and static structural simulations are given.

The transient analyses are carried out on three pulses (10800 s), divided into 21 time-steps, finer during each RF pulse (100s long). The thermal load only is active for 100 s and three times in the whole simulation.
The input parameters of the thermal analysis are:

- volume flow rate: $\dot{V} = 20l/min.$
- water inlet temperature $T_{water\ inlet} = 30°C$ (first attempt value: temperature easily available in every season to not create problems of condensation).
- water inlet pressure: $p_{water\ inlet} = 10\ bar$ (conservative value considering possible high pressure drops in the whole circuit).
- heat transfer coefficient: defined for each configuration.

In this preliminary design, the structural analyses are performed with simplified boundary conditions. In order to decrease the computational effort, it was decided to analyse a steady-state structural condition at a given time, corresponding to a specific thermal condition. A transient structural analysis will be considered with the most promising mirror design.
Hereafter the structural simulation will concern the time instant related to the highest temperature, occurring at the end of the third shot (7300 s).
In the static structural analysis, the loads are:

- the temperature distribution at 7300s,
- the pressure of the water on the channel walls (10 bar conservatively constant),
- the forces at the inlet and the outlet that simulate the continuity of the flow.

Concerning the constraints, the idea is to simulate something like a free displacement. Being the load quasi-symmetrical, it is possible to assume a null displacement of the symmetry planes in their normal direction and a null displacement on the vertical direction of the centre of the back surface (indeed, the real support could be connected to the mirror in the central back area). The equivalent support will be improved subsequently, considering a more realistic condition. In Fig. 6.10 the structural constraints, applied in the aluminium mirror, are visible.

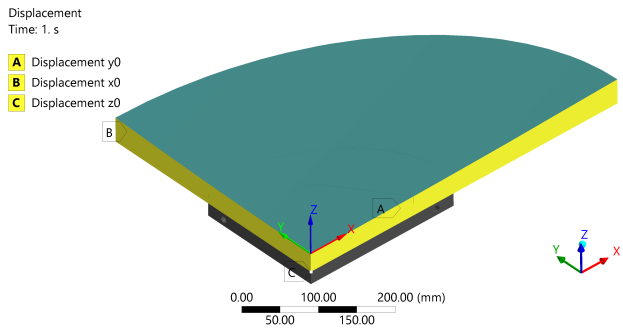

Figure 6.10: *Representation of the constraints: null displacements of the planes of symmetry (in yellow (A and B) and of the centre of the back surface (white square) (C). Here it is represented only a quarter of the mirror because the constraints are symmetric with respect to the x and y axes.*

6.2.4.1 Aluminium design thermo-structural results

The input parameters of the thermal analysis have already been reported. Only the HTC needs to be specified for each configuration:

- Heat transfer coefficient: $h \cong 17000 W/(m^2 K)$, constant, calculated considering the water properties at $T_{water\ inlet}$.

The Reynolds number is ~ 53000, a value that confirms fully turbulent flow inside the channel.

Fig. 6.11 reports the first simulation result of the design of sec. 6.2.3.1: the temperature distribution at the end of the third pulse, at 7300 s. The maximum temperature reached on the mirror is 116.2°C, an acceptable value in this kind of application (as seen in [52]), but it must be considered in relation to the thermal expansion effect. For this reason, a structural analysis is essential.

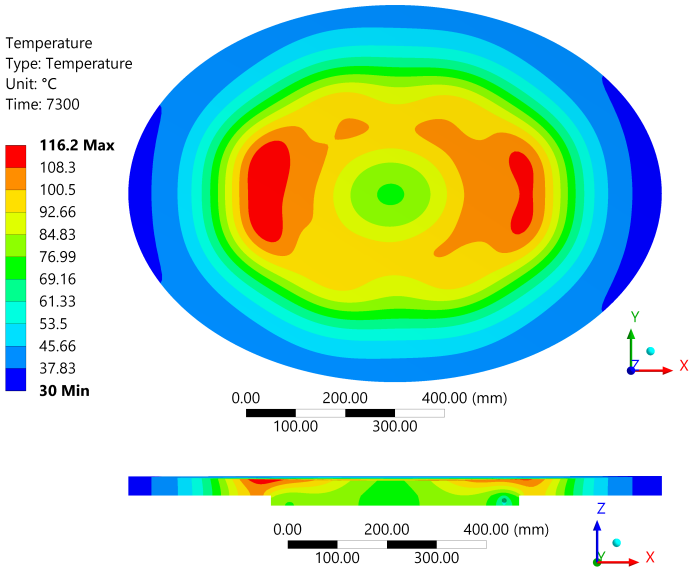

Figure 6.11: *Aluminium mirror design: (Top) Contour plot of the temperature distribution at the end of the third pulse, front view. (Bottom) Temperature distribution on the section view (x-z plane).*

The water outlet temperature at the end of the pulse reaches 41°C (Fig. 6.12), still low, and its properties change little enough to consider the HTC constant.

The maximum heat power absorbed by the water during the transient is $Q = \dot{m} c_p \Delta T_{water} = 15.25 kW$, $\sim 47\%$ of the total absorbed power (sec. 6.2.1).

The evolution in time of the maximum mirror surface temperature will be reported in section 6.2.4.4.

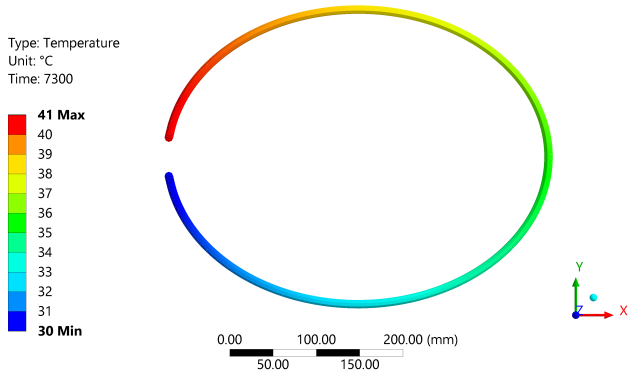

Figure 6.12: *Aluminium mirror: water temperature plot.*

Considering the structural constraints seen before, a static structural analysis (at 7300 s) is carried out. Fig. 6.13 shows the contour plot of the total deformation.

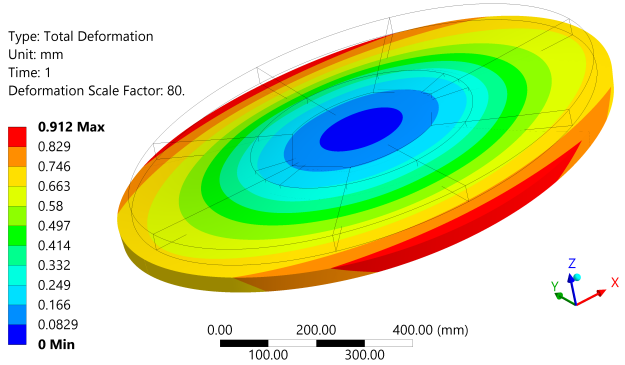

Figure 6.13: *Contour plot of the total deformation of the aluminium mirror design. Deformation scale factor (x80).*

As visible in Fig. 6.13 the maximum total deformation is 0.912 mm. The directional deformations out of the reflection plane are the most critical for the propagation efficiency of the beam, so the most important to be analysed. The trends and the maximum values of the Z directional deformation (out of the mirror plane) in the main axes (on the superior surface) of the mirror will be reported in section 6.2.4.4.

6.2.4.2 SS-Cu design thermo-structural results

The input parameters of the thermal analysis have already been reported. Only the HTC is here different with respect to the previous design due to the small change in the cross-section area:

- heat transfer coefficient: $h \cong 17600 W/(m^2 K)$, constant, calculated considering the water properties at $T_{water\ inlet}$.
  The Reynolds number is ~ 46000, a value that confirms fully turbulent flow inside the channel.

The reflective material is different from before, as reported in Tab. 6.1. The heat flux distribution changes and the peak is lower.
Fig. 6.14 shows the temperature distribution at the end of the third pulse. The pattern is different from the previous one, but the maximum temperature is 113.5°C, only 3°C lower than the previous case.
It is well visible the channel and the effect of the cooling along the path. The back surface has a different distribution too (Fig. 6.14, right).
The difference with the previous case is due to the change of the materials and the different thermal behaviour. As already mentioned, the thermal conductivity of the SS is lower than the one of the aluminium or copper, so the back surface remains cooler and heat conduction gets worse, but the position of the channel, close to the load, still allows for lower maximum temperature. Maintaining the same conditions and moving the channel closer to the rear surface would increase the temperatures.

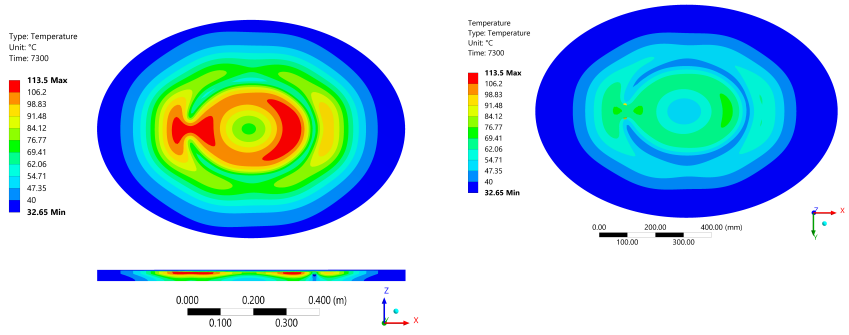

Figure 6.14: *SS-Cu mirror design: (Left) Contour plot of the temperature distribution at the end of the third pulse, front view (top) and (x-z plane) (bottom). (Right) Back view.*

In this case, the maximum water outlet temperature is 38.1°C (at

7300 s) (Fig. 6.15). The water temperature difference is low, and the maximum heat power absorbed by the water during the simulation is $Q = \dot{m} c_p \Delta T_{water} = 11.2kW$, $\sim 44\%$ of the total absorbed power. It is lower in absolute value than in the previous case, but similar in percentage, because for copper the total power is lower (sec. 6.2.1).

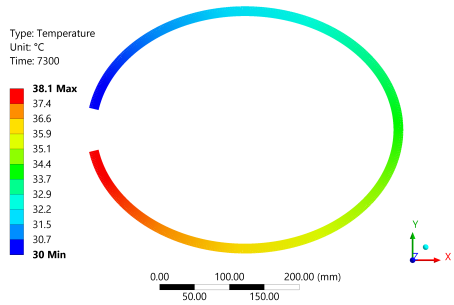

Figure 6.15: *SS-Cu mirror: water temperature plot.*

The evolution in time of the maximum temperature of the copper mirror will be reported in sec. 6.2.4.4. As done before a static structural analysis has been carried out with the thermal condition at 7300 s, with unchanged boundary conditions. The first important result is that the maximum total deformation increases by $\sim 94\%$ compared to the aluminium case, up to 1.767 mm (Fig. 6.16).

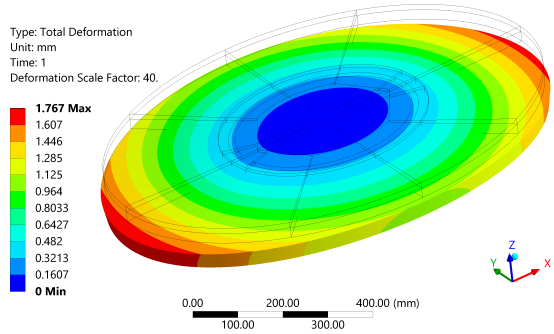

Figure 6.16: *Contour plot of the total deformation of the SS-Cu mirror design. Deformation scale factor (x40).*

The trends and the maximum values of the Z directional deformations for the major and minor axes of the superior surface will be reported in sec. 6.2.4.4.

6.2.4.3 Copper design thermo-structural results

The first analysis of the design of section 6.2.3.3 considers the same diameter and the same volumetric flow rate (10 L/min) for internal and external spirals. The heat transfer coefficient is $\cong 10000\ W/(m^2K)$, with $Re \cong 23100$.

The results of the thermal analysis at the end of the third pulse (7300 s) are visible in Fig. 6.17.

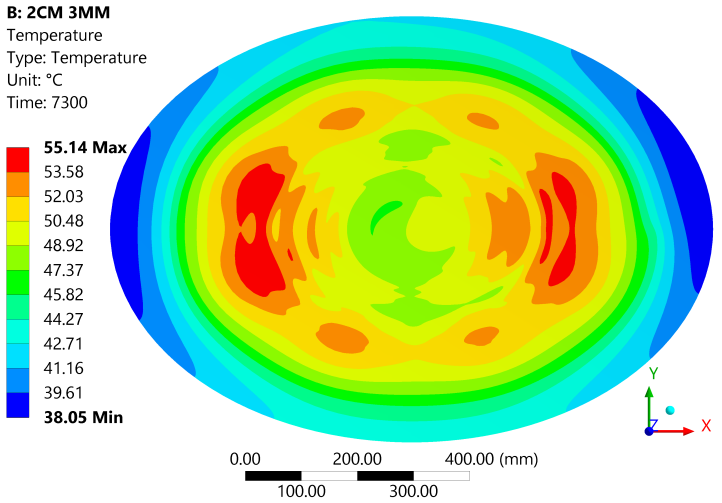

Figure 6.17: *Copper mirror: (Top) Contour plot of the temperature distribution at the end of the third pulse, front view. (Bottom) Temperature distribution on the section view (x-z plane).*

The maximum surface temperature is remarkably decreased, up to 55.1°C. The temperature distribution is also more uniform, and the minimum temperature is higher, resulting in a lower maximum gradient. The water outlet temperature (Fig. 6.18) in the inner spiral reaches a value of 43°C, while in the external spiral the maximum value is 49°C, which is not reached at the outlet because, during the last round, the heat exchange changes and the water heats the outer edge of the mirror, which remains colder. This result is useful to better even out the temperature over the mirror, reducing the temperature gradients.
The maximum absorbed thermal power by the water during the transient is $Q = \dot{m} c_p \Delta T_{water} = 21.9kW$, $\sim 87\%$ of the total absorbed power (sec.

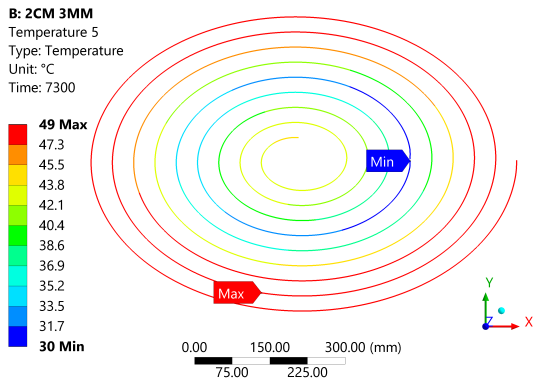

Figure 6.18: *Water temperatures along the internal and external spirals.*

6.2.1). This value is much higher than in previous configurations because, in the copper design, the cooling system is more effective, for the reason seen in section 6.2.3.3.
The evolution in time of the maximum temperature of the copper mirror will be reported in section 6.2.4.4.

With the new design, a more realistic constraint in structural analysis is considered.
With the hypothesis of a spherical joint to sustain the mirror at the centre of the back surface, new constraints are implemented in the simulations, as visible in Fig. 6.19. The back central zone of the mirror has a compression-only support (in blue in Fig. 6.19), the central orthogonal faces are blocked to move in their normal direction (orange and green reference in Fig. 6.19) and the back centre is blocked in Z direction (red reference in Fig. 6.19).

The maximum total deformation of the copper mirror is 0.144 mm, and the contour plot is visible in Fig. 6.20.

The large temperature drop leads a significant decrease in the deformation. The maximum total deformation at the end of the pulse is about 84% lower than the first result, in the aluminium mirror with a 1-turn channel. The trends and the maximum values of the Z directional deformation in the main axes of the mirror will be reported in section 6.2.4.4.

6.2.4.4 Comparison of the thermo-structural results

In this section, a comparison of the results of the three designs is done. Tab. 6.2 reports the main results in temperature and the Fig. 6.21 shows

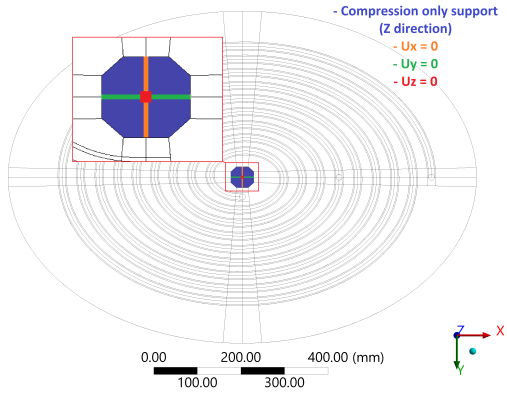

Figure 6.19: *Structural constraints of the copper mirror.*

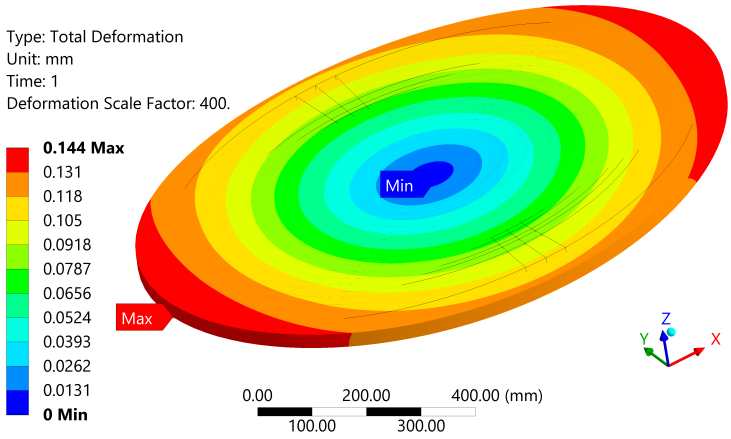

Figure 6.20: *Contour plot of the total deformation at 7300 s of the copper mirror (2cm-3mm).*

the evolution in time of the maximum mirror surface temperature for the three configurations. The trends of the first and second designs (blue and grey) are similar, while the trend of the third design (orange) is quite different, mainly concerning the peak, that in the third design is reduced by 51% with respect to the second design. This important improvement in the temperature distribution is certainly positive for the structural results.

In the first and second designs, the temperature after 1 h returns close to the initial condition, but not equal. However, the maximum temperature rise at the end of each pulse is very low ($\sim 0.1°C$). In the third design,

the mirror reaches the initial condition again before the next pulse. So, in this kind of configuration, it becomes unnecessary to evaluate the thermal performance over three pulses, but only one pulse is sufficient.

Table 6.2: *Main temperature results of the three designs.*

7300 s	**AL Mirror**	**SS-Cu Mirror**	**Cu Mirror**
Max T mirror [°C]	116.2	113.5	55.14
T water OUT [°C]	41	38	43 int 49 ext

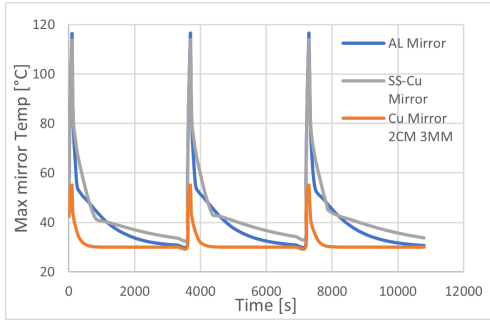

Figure 6.21: *Graph of the evolution of the maximum mirror temperature in time for the three design configurations considered.*

The Z directional deformation maximum values in the major and minor axes of the mirror of the superior layer are reported in Tab. 6.3, in addition to the maximum value of the total deformation. In Fig. 6.22 the trends of the Z directional deformations are shown for the main axes. The comparison of the three configurations shows that the design in SS-Cu is the worst solution, and the only copper design is the best one. Not only the maximum total deformation decreases by 84% in the only copper mirror, but the maximum value of the Z directional deformation decreases by 93% on the major axis and 96% on the minor axis.
The difference is that the deformation of the copper mirror on the major axis is positive contrary to the previous cases.

The copper mirror turns out to be the most suitable solution, certainly not free of charge. To achieve this, it was essential to consider a cooling system that was certainly more complex, a heavier material, and more expensive.

Table 6.3: *Maximum values of the total deformation and the Z-directional deformation on the major and minor axes of the three designs.*

	AL Mirror	SS-Cu Mirror	Cu Mirror
Max TOT def [mm]	0.912	1.767	0.144
Max Z def MAJOR axis [mm]	-0.568	-1.744	0.037
Max Z def MINOR axis [mm]	-0.815	-1.091	-0.031

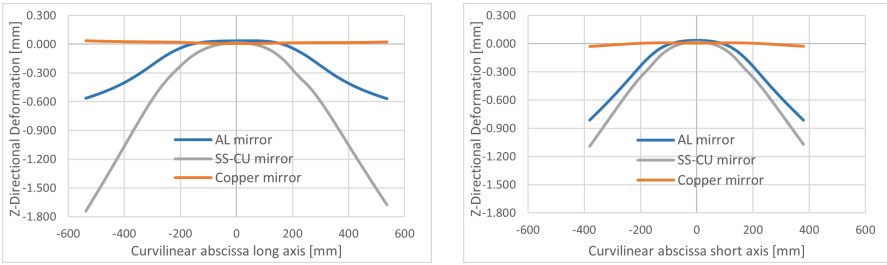

Figure 6.22: *Comparison graph of the z-deformation on major (top) and minor (bottom) axes among aluminium mirror, SS-Cu mirror, and copper mirror.*

6.2.5 Optimization of the mirror performance

Having found the best solution in the copper mirror design, as shown in section 6.2.4, some features are optimised.

6.2.5.1 Effect of the mirror thicknesses

The first optimization concerns the thicknesses. Pursuing the objective of reducing the deformations, different thicknesses of the layer (3;4;5mm) and of the mirror (1.5;2cm) are studied. The first solution of the copper mirror foresees a total thickness of 2 cm, with a minimum thickness for the layer of 3 mm. A parametric analysis for the different cases is executed. The results of the comparison are reported in Tab. 6.4 and in the graphs of Fig. 6.23.

From the maximum values of the total deformation reported in Tab. 6.4, it is visible that the solution using 1.5 cm thickness is worse than 2 cm, regardless of layer thickness: less material allows a reduction of the

Table 6.4: *Comparison of the maximum values of total deformation and Z-directional deformation among 5 configurations of the copper mirror.*

	2CM 3MM	2CM 4MM	2CM 5MM	1.5CM 3MM	1.5CM 5MM
Max TOT DEF [mm]	0.144	0.145	0.145	0.154	0.155
Max Z DEF Long axis [mm]	0.037	0.017	0.016	0.039	0.019
Max Z DEF Short axis [mm]	-0.031	-0.043	-0.051	-0.044	-0.064

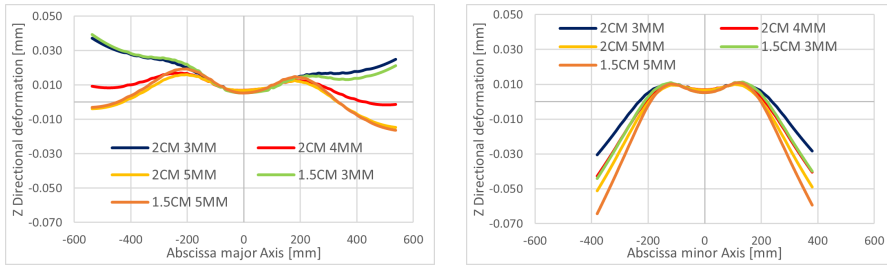

Figure 6.23: *Comparison of the Z deformation along major (top) and minor (bottom) axes among all the configurations of the copper mirror.*

weight of the structure, but it also reduces the stiffness, so the mirror becomes more prone to deformations.
The choice among the layer thickness (3 mm, 4 mm, or 5 mm) is not trivial. The 5 mm configuration seems to be better considering z-deformations on the major axis, but the 3 mm one exhibits lower deformation along the minor axis. The solution of 4 mm presents intermediate values of the maximum Z directional deformations.
To individuate the final choice, it is useful to refer to Fig. 6.23, reporting the trends of Z-directional deformations on two main axes for all the configurations.
It is visible how the 4mm deformation trend is in the middle of the previous two. It produces a more homogeneous deformation in the major axis, so 2 CM-4 MM is the best solution.

6.2.5.2 Hydraulic flow balancing

As reported in section 6.2.4.3, the mass flow rate is equal for both spirals internal and external. This leads to different pressure drops because the spiral lengths are not equal. With regard to the future installation of the cooling circuit, in order to avoid the use of intermediate valves or pumps, the system must be designed to have the same pressure drops. For this purpose, four conditions must be satisfied simultaneously:

- $\Delta P_{int} = \Delta P_{ext}$ (Evaluated for straight tubes and multiplied by a corrective factor (1.5))
- $\Delta P = 1bar$ (Arbitrary choice inside the range of 4 bar, compatible with DTT water cooling system)
- $\dot{V}_{tot} = \dot{V}_{int} + \dot{V}_{ext}$
- $\dot{V}_{tot} \cong 20L/min$

The system is solved by setting an array of internal mass flow rates (Tab. 6.5) and finding for each value a couple of internal and external diameters (consequently the external mass flow rate), which guarantee equal pressure drops.

Table 6.5: *Values of the channel diameters related to specific volume flow rates.*

$\dot{V}_{int}[L/min]$	$d_{int}[m]$	$d_{ext}[m]$
4	0.0084	0.0177
6	0.0098	0.0168
8	0.0109	0.0159
10	0.0119	0.0149
12	0.0127	0.0137
14	0.0135	0.0123
16	0.0142	0.0105

In order to choose the optimal pair of diameters, seven thermal simulations, corresponding to the cases reported in 6.5, are carried out, without changing the geometry of the mirror (the diameters of the spirals), but using a reference geometry (2cm-5mm) with $d_{int} = d_{ext} = 1.4cm$ and applying adaptive HTCs, calculated as follows:

$$h_{fem} = h_{eff} \cdot \frac{A_{side\ eff}}{A_{side\ fem}} \tag{6.2}$$

where h_{fem} is the fictitious HTC to be used with the reference geometry, h_{eff} is the effective HTC (calculated analytically with the correct diameters), $A_{side\ eff}$ is the convection area of the effective geometry and $A_{side\ fem}$ of the reference geometry.
The results of these thermal simulations are visible in the graph of Fig. 6.24, in which the maximum ΔT, the $T_{average}$ and T_{max} of the mirror are plotted.
The choice of the pair of diameters is done with the objective to minimize the temperatures. The lowest values are related to an internal flow rate of $\sim 10 L/min$.

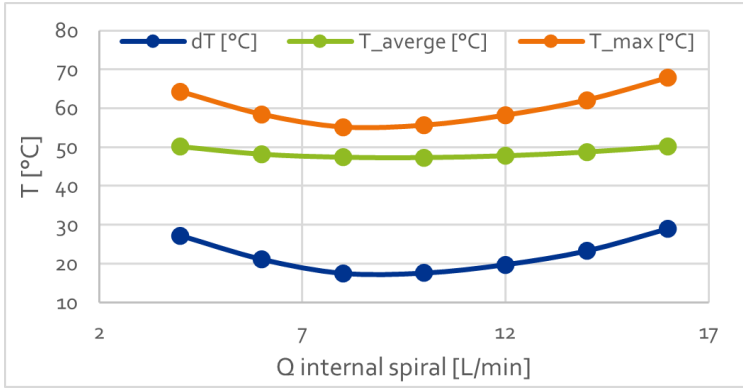

Figure 6.24: *Comparison of the results of 7 sets of* $\dot{V}_{int}, d_{int}, d_{out}$.

The pair of diameters corresponding to this value of flow rate is approximatively $d_{int} = 12mm$,$d_{ext} = 15mm$. Such approximation leads to a $\dot{V}_{int} = 10.279 L/min$ and $\dot{V}_{ext} = 10.280 L/min$.

6.2.5.3 Complete thermal and structural analysis results

Once all the study and the comparison have been executed, having the final design, in geometry and material, the right thicknesses, and the right hydraulic condition, it is useful to carry out a complete analysis. It concerns a coupled transient thermo-structural simulation, in which analysing the mirror temperature and deformation during and after the heat pulse. Not only the deformation in steady state condition will be thus analysed, but also the time evolution of the deformation. The total analysis time

is 300 s, considering only one pulse as explained in the results of section 6.2.4.4. The thermal load is active in the range 10 s - 110 s, to permit to stabilize the conditions in the first 10 s.

Considering the last geometry (2cm-4mm) (Fig. 6.25), a structured mesh is realized, as visible in Fig. 6.26.

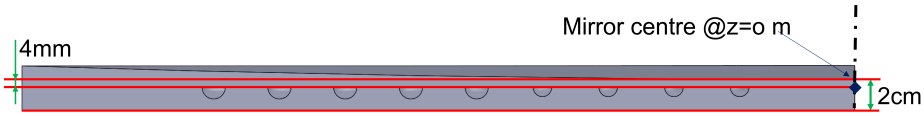

Figure 6.25: *Copper mirror last geometry: section view of a half part of the mirror.*

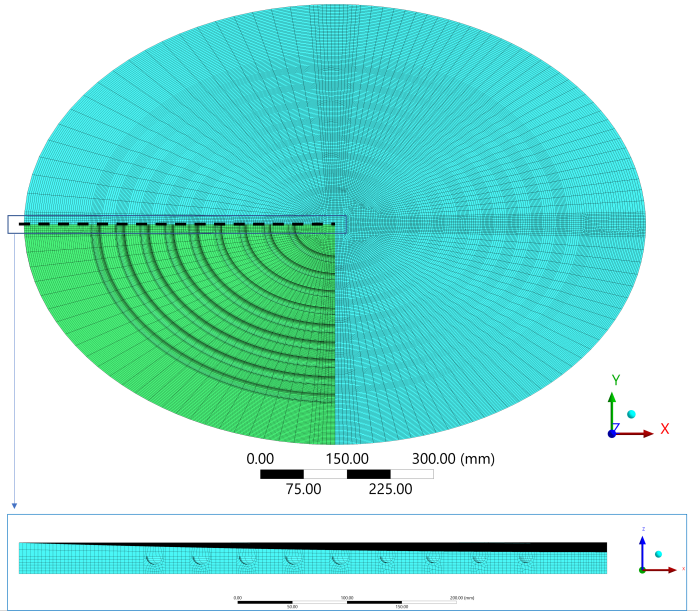

Figure 6.26: *(Top) Mesh of the latest version of the copper mirror. In the bottom left corner, the detail of the mesh of the bulk with the channel is visible. (Bottom) Section view of half part of the mirror.*

The thermodynamic features are:

- volume flow rate: $\dot{V}_{int} = 10.279\ l/min$, $\dot{V}_{ext} = 10.280\ l/min$.
- water inlet temperature $T_{water\ inlet} = 30°C$.

- water inlet pressure: $p_{water\ inlet} = 10\ bar$.
- heat transfer coefficient: $h_{int} \cong 14000 W/(m^2K)$, $h_{ext} \cong 9000 W/(m^2K)$, $Re_{int} \cong 28000$, $Re_{ext} \cong 22000 W/(m^2K)$, HTCs constant, calculated considering the water properties at $T_{water\ inlet}$.

The boundary conditions of the structural analysis:

- temperature field,
- pressure inside the channel (10 bar),
- forces at the inlet and outlets for, continuity of flow,
- support constraint.

The results at the end time of the RF pulse are visible in Fig. 6.27.

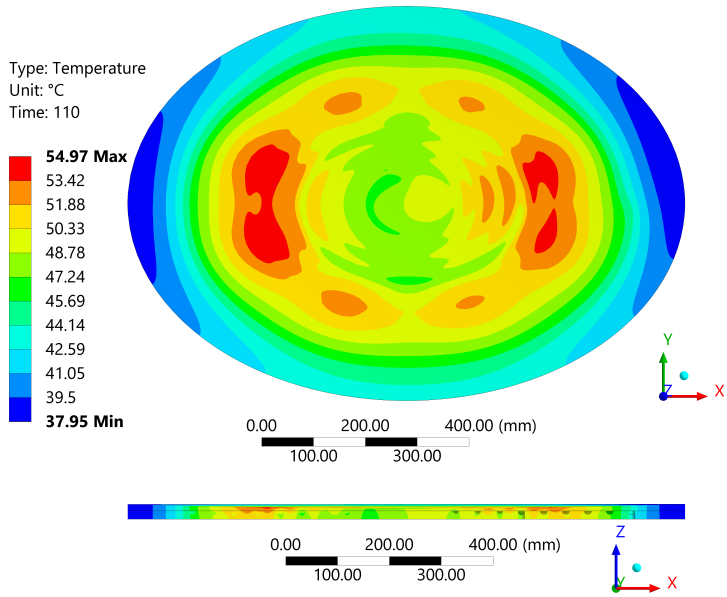

Figure 6.27: *Contour plot of the temperature at the end of the pulse in the latest version of the copper mirror: (top) frontal view, (bottom) section view.*

The maximum surface temperature of the mirror over time is 54.97°C. The water temperature reaches the value of 48.5°C in the external spiral, whilst 43.8°C in the internal spiral.

Figures 6.28-6.29 show the contour plots of the total deformation at two different instants, 44 s and 110 s respectively. In the graph of Fig. 6.30 the maximum total deformation and maximum temperature in time are plotted, while Fig. 6.31 plots the maximum and minimum z-deformation in time along the major and minor axes.
It is possible to observe that the total deformation is higher at 44 s (i.e. 34 s after the pulse start) than at the end of the shot (110 s, namely 100 s after the pulse start). The deformation value is 0.177 mm at 44s versus 0.140 mm at 110s. The temperature gradient along the thickness around 44 s is higher than the end time.
As visible from Fig. 6.30-6.31 the main difference between these instants is the deformation out of the mirror plane.

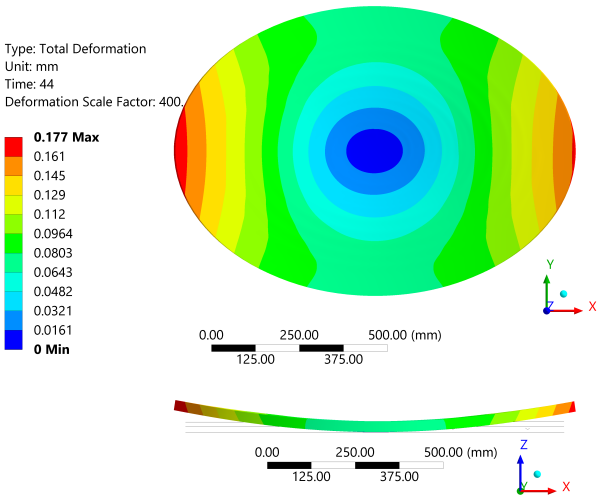

Figure 6.28: *Contour plot of the total deformation at 44s in the last version of the copper mirror: (top) frontal view, (bottom) side view. Deformation scale factor:* $\times 400$.

At 44s the z components are much higher than at 110s (see also Fig. 6.31), where most of the total deformation is given by the x and y components. Indeed, in Fig. 6.29 the deformation out of the mirror plane is low, but the expansion on the mirror plane is high. The black ellipse in Fig. 6.29 shows the undeformed mirror. It shows as the mirror expands along the plane.
Looking at the first instants ($\sim 1.5s$ from the start) in Fig. 6.30, despite

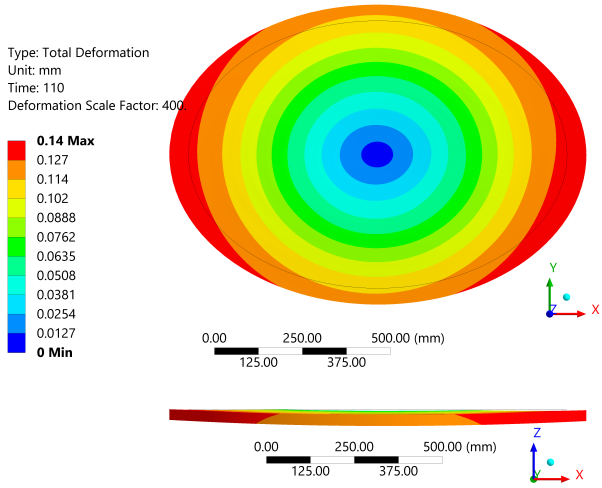

Figure 6.29: *Contour plot of the total deformation at 110s in the last version of the copper mirror: (top) frontal view, (bottom) side view. Deformation scale factor:* $\times 400$.

the low temperatures, the distribution of the temperatures produces a fast increment of the deformations. As visible in Fig. 6.31, reporting the Z directional deformation over time on the mirror axes, this kind of deformation is in the opposite direction with respect to that one occurs at 44 s, indeed, the z-directional deformation at $\sim 11.5s$ is negative, whilst at 44s it is positive.
Therefore, considering these kinds of results, not only the deformation at 110s needs to be verified with optical codes, in order to study beam deflection, but also the mirror deformation at 44s, which seems to be more dangerous, mainly due to the deformation out of the mirror plane.

From the graph in Fig. 6.30, it can be seen that an even higher total deformation is recorded around 150 s, but what happens after the 110 s instant is of little interest from the optical point of view. Actually, from a structural point of view, these thermal loads do not pose any problems for the system. If the deformations are also beyond acceptable limits when the impulse has already been interrupted, these deformations do not affect the transmission efficiency of the beams.
Finally, it is visible how after 300 s the temperatures return close to the initial conditions, as do the deformations. At the end of a duty cycle, lasting 1 h, the mirror temperatures will have completely recovered to its

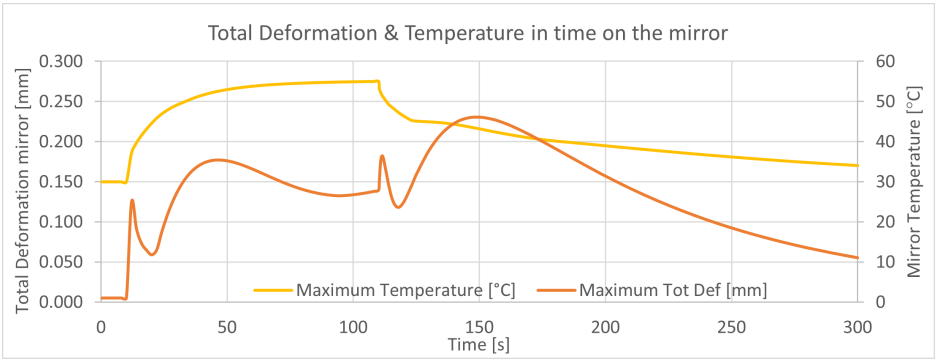

Figure 6.30: *Graph of the trends of the maximum total deformation and temperature in time for the last version of the copper mirror.*

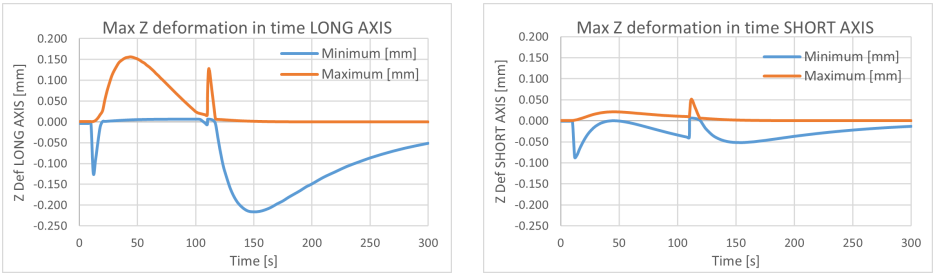

Figure 6.31: *Graphs of the trends of the minimum and maximum Z-deformation along the long (left) and short (right) axes.*

initial conditions.

6.2.6 Non-simultaneous beams

The last activity of this part concerns the study of this configuration of mirror subjected to different loads: during the exploitation of DTT, it could happen that not all the beams are simultaneously on, so only a part of the set could transmit the power. In this case the thermal load on the mirror is lower, but it assumes a different distribution which leads to different deformation. The symmetry is lost and other thermo-structural simulations are necessary.

The graphs in fig. 6.32 show the comparison of the results between these simulations. The z-directional deformations are always lower than the original case, in which all the beams act together. This confirm that, despite the loss of the partial symmetry of the thermal load, however the

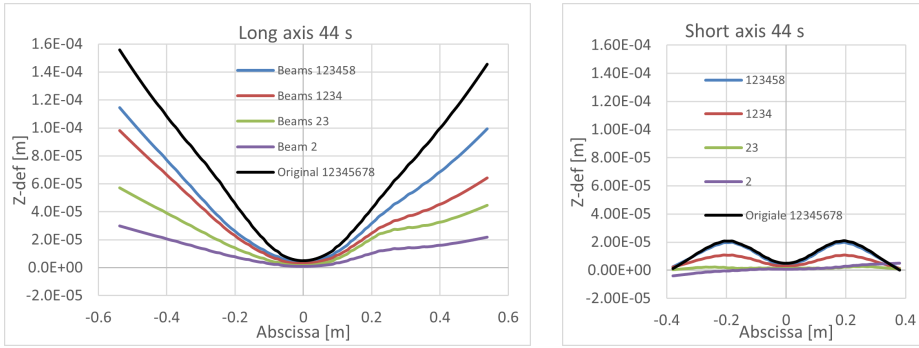

Figure 6.32: *Comparison of Z-deformation on the long axis for different configurations of load on the copper mirror.*

most loaded configuration is worst from structural point of view and the design can continue with the analysis of the configuration with all beams.

6.2.7 MBTL parabolic mirror: summary and first considerations

A comparison of different parabolic mirror designs of the DTT ECRH MBTL was presented. The three configurations analysed include an aluminium and copper mirror, a stainless-steel and copper mirror and a copper-only mirror. Different cooling systems were implemented, and thermo-structural simulations were carried out, to evaluate the best configuration from a thermal and structural point of view. The study led to define the copper-only mirror as the best configuration, that was optimized in the thicknesses and the hydraulic parameters.
It is a copper mirror with a bulk dug by a cooling channel in the shape of a double spiral, with the addition of a cover layer. The minimum total thickness of the mirror is 2 cm, including 4 mm (minimum thickness) of the cover layer. The inlet of the cooling channel is located on the major axis, in correspondence with the peak of the heat flux hitting the mirror. Two outlets are foreseen, because the circuit is divided into two channels, one towards the centre of the mirror and one towards the external edge, to simultaneously cool two different areas of the mirror. Considering an inlet water temperature of 30 °C and a mass flow rate of $\sim 10 L/min$ for both spirals, the maximum temperature on the mirror, during the 100 s of the pulse, is $\sim 55°C$, recorded at the end time, with an increase in water

temperature of 13.8 °C and 18.5 °C in the internal and external channels, respectively.
The thermal gradient along the radius and especially along the thickness results in thermal expansion effects. At the end of the pulse the maximum total deformation is 0.140 mm. Despite the maximum temperatures are recorded at the end, the most critical instant from the deformation point of view is approximately 34 s after the start of the pulse, when the maximum total deformation reaches a value of 0.177 mm. Even the first instants could be dangerous, because a sudden increase in deformation occurs about 1.5 s after the start of the pulse, producing deformation in the opposite direction (negative deformation in the z-direction). However, the maximum value is lower than that at 34 s and more abrupt. If the deformation at 34 s will be acceptable, it will not be necessary to further analyse the deformations occurring at later times.
The resulting deformed geometry at the critical instant will be verified with optical codes to study its effect on the beams' propagation. First results of the study about the coupling losses produced by this kind of mirror deformation is reported in article [21], but they are progressing, considering the deformations on the other mirrors of the MBTL.

6.3 Update of thermal conditions for Parabolic mirror

In this section, the update of the calculations for the change of the water inlet temperature to 15°C, consistent with the Water Cooling System (WCS) requirement, is presented. As suggested by the WCS group, the water inlet temperature for the mirrors can be 15°C. So new thermo-structural analyses are executed with the new condition.
The thermodynamic features are the same of the previous analysis, except for the inlet water temperature and for the HTC, dependent on the water temperature:

- Volume flow rate: $\dot{V}_{int} = 10.279\ l/min$, $\dot{V}_{ext} = 10.280\ l/min$.
- Water inlet temperature $T_{water\ inlet} = 15°C$.
- Water inlet pressure: $p_{water\ inlet} = 10\ bar$.
- Heat transfer coefficient:

$h_{int} \cong 11000 W/(m^2K)$, $h_{ext} \cong 75000 W/(m^2K)$, constants, calculated considering the water properties at $T_{water\ inlet}$.

The structural constraints remain unchanged, as visible in fig 6.19. The results are reported in the tab. 6.6 and in the graph of fig. 6.33.

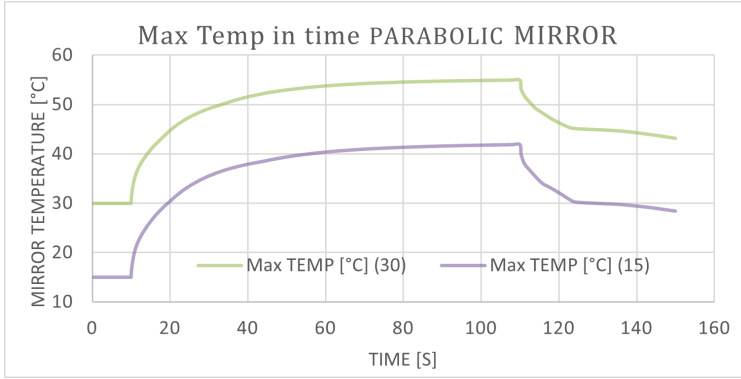

Figure 6.33: *Graph of comparison of the trends of the maximum temperature of the parabolic mirror with two different water inlet temperatures.*

Table 6.6: *Comparison of temperatures at 100s with two different water inlet temperatures for the parabolic mirror.*

$1^{st}shot(t = 100s)$	$T_{in} = 30°C$	$T_{in} = 15°C$
T max [°C]	54.9	41.9
T min [°C]	37.9	22.8
T water out (Int-Spiral) [°C]	43.8	29.1
T water out (Ext-Spiral) [°C]	48.5	33.6

As foreseeable, seeing from Fig. 6.34 and tab. 6.6, the lower inlet temperature leads to lower temperatures on the mirror. The maximum temperature decreases of about 13°C. On the other hand, it causes a decrement of the HTC value, not positive for the maximum difference of temperature on the mirror. At the end of the pulse (after 100 s), the thermal gradient increases of 2°C (from 17°C to 19°C). So, the higher gradient produces higher deformation as visible in fig. 6.34 from the comparison of the trends of the Z directional deformation on major and minor axes of the mirror at the instants 44 s (34 after the pulse start) and 110 s (100 s after the pulse start). The same result is visible in the graph reporting

the trends of maximum temperature and maximum total deformation in time (fig. 6.35).

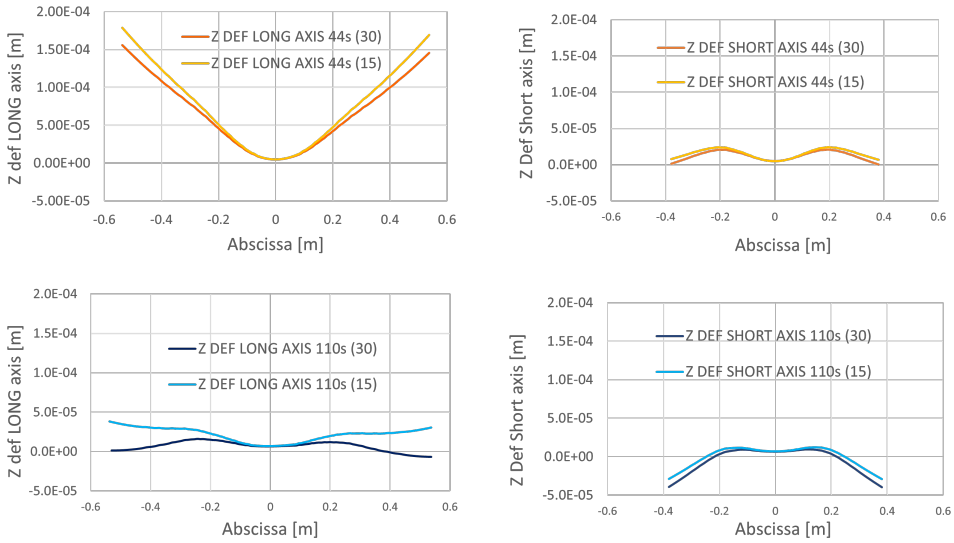

Figure 6.34: *Graphs of the Z directional deformations on the long axis (top) and short axis (bottom) in two different instants (44 s (left) and 110 s (right)) comparing two different water inlet temperatures.*

Table 6.7: *Max total deformations and max Z deformations at 44s and 110s for two inlet temperatures*

	44 s		**110 s**	
	$T_{in} = 30°C$	$T_{in} = 15°C$	$T_{in} = 30°C$	$T_{in} = 15°C$
Max TOT DEF [mm]	0.177	0.198	0.140	0.145
Max Z DEF Long axis [mm]	0.156	0.179	-0.016	0.038
Max Z DEF Short axis [mm]	0.021	0.024	-0.040	-0.029

An increment of the maximum thermal gradient of $\sim 12\%$ (from 17°C to 19°C) leads to an increment of $\sim 12\%$ of the maximum total deformation at 44 s.

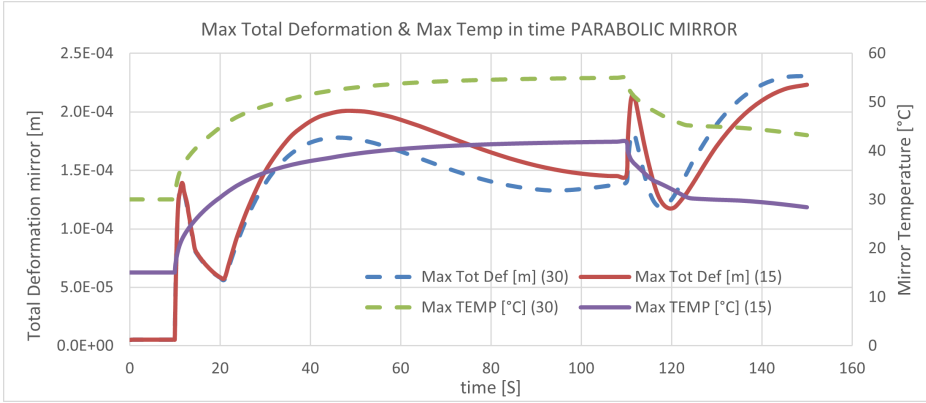

Figure 6.35: *Graph of the trends of maximum total deformations and temperatures over the time with two water inlet temperatures.*

6.4 MBTL Flat mirrors design

In order to permit to ECRH group to evaluate spillover and coupling losses in the line [21], due to non-idealities of the mirrors surface deformation, a complete transient thermo-structural analysis is required for a selected number of TL mirrors. For this reason, it's important to complete a sequence of mirrors, designing the other kind of mirrors of the line. The sequence of four mirrors inside the corridor of the line is visible in fig. 6.36.

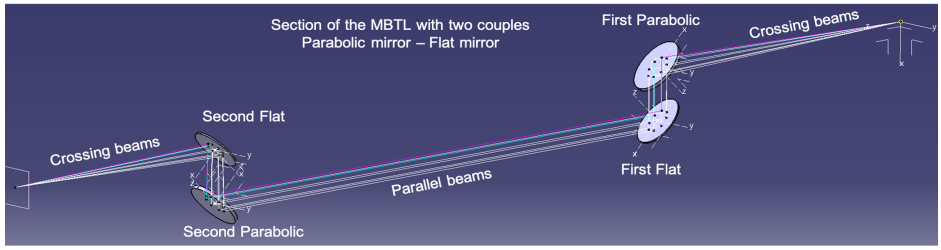

Figure 6.36: *Set of a sequence of mirrors internal to the corridor of the MBTL: two parabolic and two flat mirrors.*

The two parabolic mirrors of a sequence of the line are equal and characterized by the same thermal load, so the design of the previous one can be adopted for the other parabolic mirrors. Instead, the flat mirrors, which are equal to each other in geometry, are different in terms of heat fluxes, in the case of reflection of crossing or parallel beams (ref.

fig. 6.36). The beams propagate alternatively crossing or parallel to each other between two focusing mirrors on which they are separated [21].

6.4.1 Geometry of flat mirrors

The main differences between flat and parabolic mirrors are the size and the reflective surface. The flat mirror has a minor radius of 350 mm and a major radius of 495 mm, and the reflective surface is flat. So, the flat model is very similar to the parabolic one, as visible in fig. 6.37. Also in this model the total thickness is equal to 2cm, comprehensive of 4 mm of the cover layer. The diameters of the channel are respectively 12 mm and 15 mm for the internal and external semi-circular cross-sections. The mirror material is pure copper.

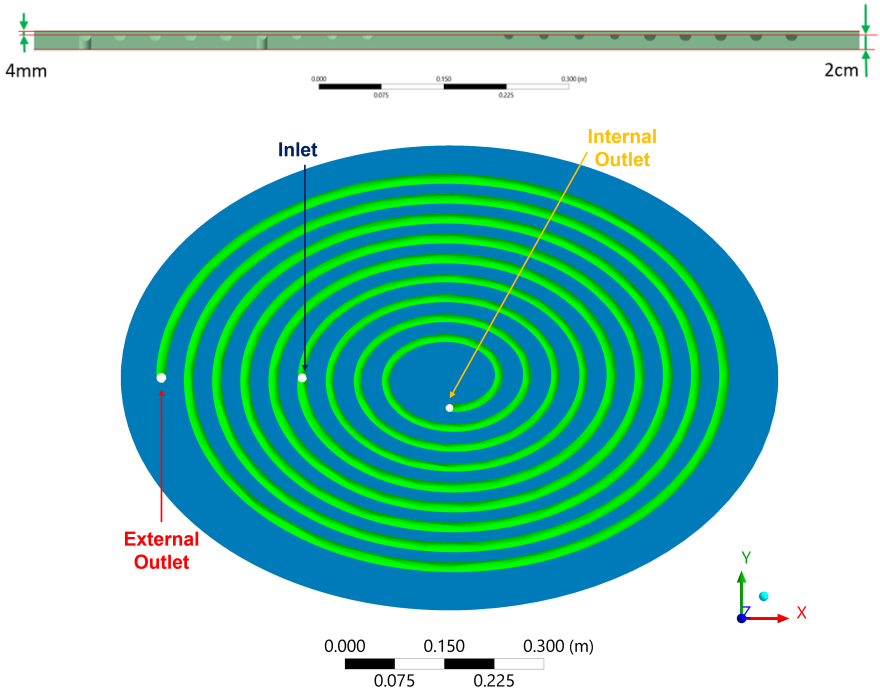

Figure 6.37: *CAD geometry of the flat mirror internal to the corridor.*

6.4.1.1 Details of realization of the mirror with spiral channel

In section 6.2.3.3 was presented for the first time the channel with double spirals for the parabolic mirror, but a part from dimensional details,

the realization of the spiral path wasn't presented. This paragraph wants to clarify the realization details, being the spiral channel a news in this field. The features presented are equal for all the MBMs with double spirals of the chapter and the same for the spiral pitch. Instead the angular ranges and dimensions can change for each configuration.
The parametric equation of the spiral path is the following ones:

$$\begin{cases} x(\theta) = -\frac{r_{major}}{r_{minor}} \cdot \frac{30}{2\pi} \cdot \theta sin(\theta) \quad [mm] \\ y(\theta) = \frac{30}{2\pi} \cdot \theta cos(\theta) \quad [mm] \end{cases} \tag{6.3}$$

Two spirals are simply two different ranges of the same equation (fig. 6.38). The internal spiral (green in fig. 6.38) has an angular range of $2\pi - 9.5\pi$, whilst the external one (red in fig. 6.38) $9.5\pi - 19.5\pi$. The points at $\theta = 2\pi; 9.5\pi; 19.5\pi$ are respectively at the inner outlet, the inlet and the external outlet.

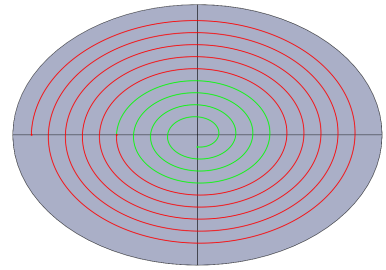

Figure 6.38: *Double spiral path.*

The problem that arises with the spiral at these 'critical' points relates to its characteristics. It has no vertical or horizontal tangents in the points that intercept the axes. Thus, the normal of the channel section (created on the spiral path) at critical points would not be parallel to the axes and this occurrence could produce misalignments in the realization of the inlet and outlet holes. For this reason the spiral path needs some adjustments: the path is made rectilinear in correspondence of the points, modifying as low as possible the spiral.
Inner outlet (Fig. 6.39 bottom right zoom): a segment (blue) is created with two constraints: tangent to the spiral (red) and perpendicular to the axis. The result is a segment of about 6.7 mm and an inner outlet translated on y-axis of 0.4 mm (negligible variation, but useful for the respect of perpendicularity).
Inlet (internal spiral side, fig. 6.39 left zoom and external spiral side, fig. 6.40 right zoom): a segment (black) of 4 mm is created with two constraints: perpendicular to the axis with a distance from the spiral end of 0.5 mm, and tangent to the spline realized on the spiral (red).
External outlet (Fig. 6.40 central zoom): a segment (black) of 4 mm is created with two constraints: perpendicular to the axis with a distance from the spiral end of 0.5 mm, and tangent to the spline (blue) realized

on the spiral (red).

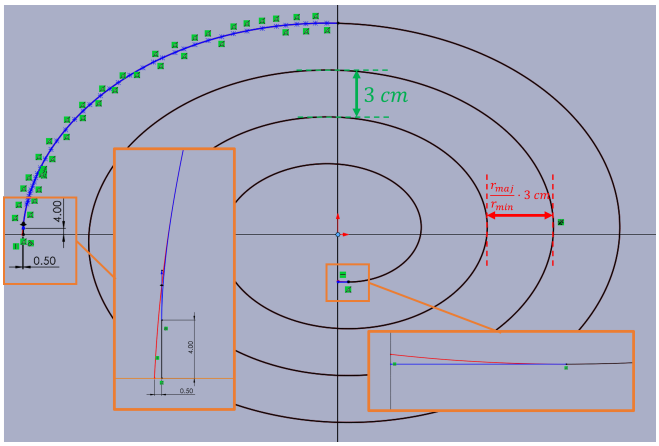

Figure 6.39: *Internal spiral: details of adjustment.*

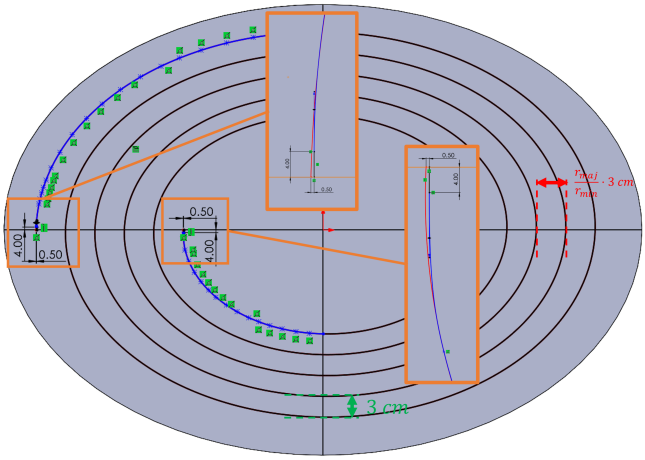

Figure 6.40: *External spiral: details of adjustment.*

The last part of the realization of the CAD model foresees the division of the mirror, as in fig. 6.41. The procedure is necessary to realize a structured mesh, that, as opposed to a tetrahedral mesh, allows to have an higher mesh quality with less elements. The presence of a spiral channel makes it harder: the path and the

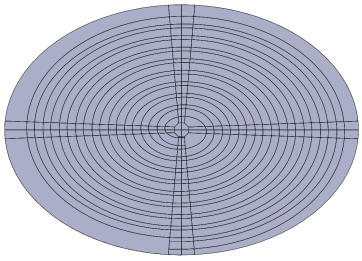

Figure 6.41

cross section break the symmetry on the radius and thickness, for this reasons the number of bodies of the division is high.

6.4.2 Thermal load of flat mirrors

The thermal load is the absorbed fraction of the microwave beam power, calculated as explained in section 3.3, with the same condition of Q and A reported in section 6.2.1. The parameters for the load calculation change as reported in Tab. 6.8.

Table 6.8: *Microwave load parameters for MBTL FLAT mirrors.*

	$w_x[m]$	$w_y[m]$	$P_{abs\ MAX}[MW/m^2]$	**A**
Parallel FLAT	0.12654	0.08948	0.18478	0.21%
Crossing FLAT	0.14827	0.10484	0.17179	0.21%

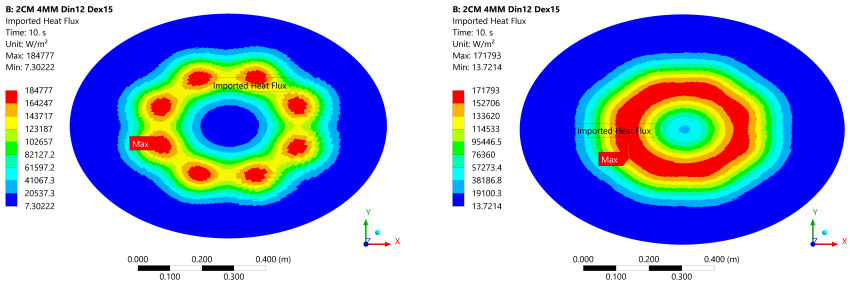

Figure 6.42: *Contour plot of the heat flux of the microwave load for the parallel flat mirror (left) and the crossing flat mirror (right).*

The two mirrors are characterized by different heat flux distributions as shown in fig. 6.42, due to different beam sizes (w_x and w_y) and different locations of the beam centres.

6.4.3 Thermo-structural analyses of Flat mirrors

Once the model for this kind of mirror is completed, thermo-structural simulations are carried out, again comparing the solution with two water

inlet temperatures (15°C-30°C), considering the same boundary conditions used before. In the following rows the results are visible.

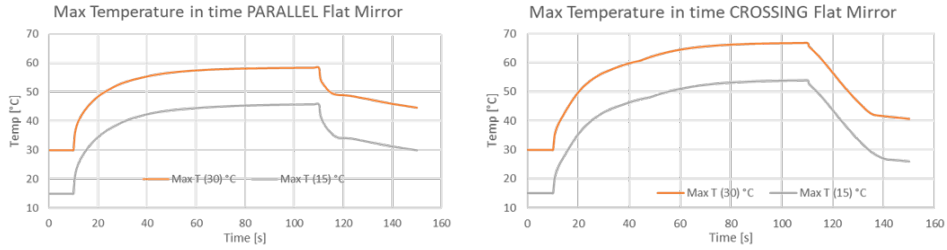

Figure 6.43: *Graph of comparison of the trends of the maximum temperature of the parallel flat mirror (left) and crossing flat mirror (right) with two different water inlet temperatures.*

Table 6.9: *Comparison of the temperatures at 100s with two different water inlet temperatures for the parallel and crossing flat mirrors.*

T_{in}	$30°C$	$15°C$	$30°C$	$15°C$
$1^{st} shot (t = 100s)$	**PARALLEL**		**CROSSING**	
T max [°C]	58.5	45.8	66.7	53.9
T min [°C]	43.9	29.7	40.5	25.4
T water out (Int-Spiral) [°C]	44.0	29.0	50.0	35.0
T water out (Ext-Spiral) [°C]	50.0	35.0	44.0	28.0

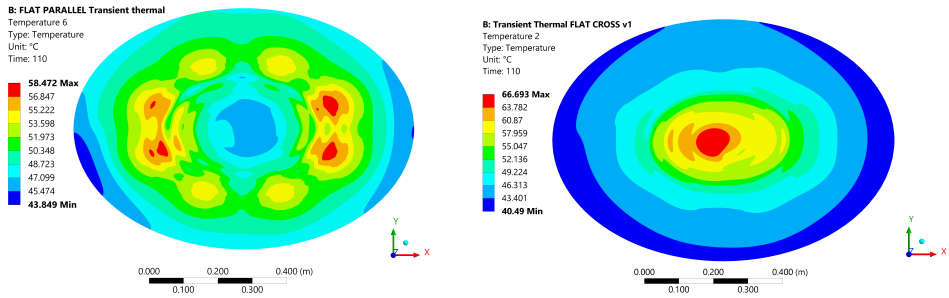

Figure 6.44: *Contour plots of the temperature on the PARALLEL FLAT mirror (left) and CROSSING FLAT mirror (right) considering T water inlet of 30°C.*

As visible from the tab. 6.9 and figures 6.43-6.44, the solutions at

15°C as inlet temperature are better in terms of maximum temperature. But the crossing flat mirror seems to have a very different behaviour with respect to the parallel one. This is caused by the distribution of heat flux, that is more concentrated near the centre. Indeed, the hot spot is located in the centre and reaches a maximum temperature $\sim 8°C$ higher than the parallel configuration.

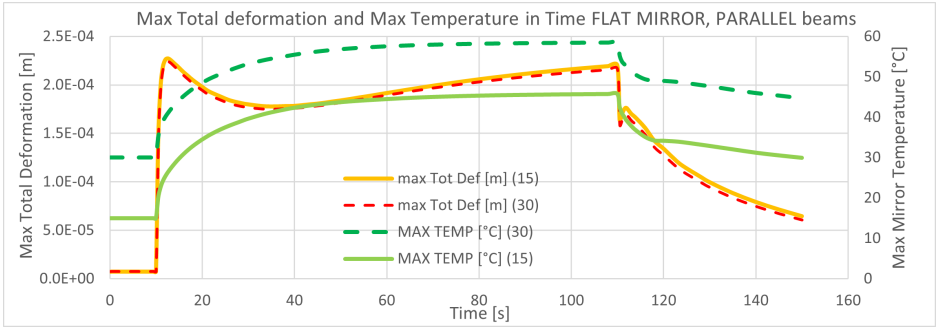

Figure 6.45: *Graph of the trends of the maximum total deformations and temperatures over the time with two water inlet temperatures for the parallel flat mirror.*

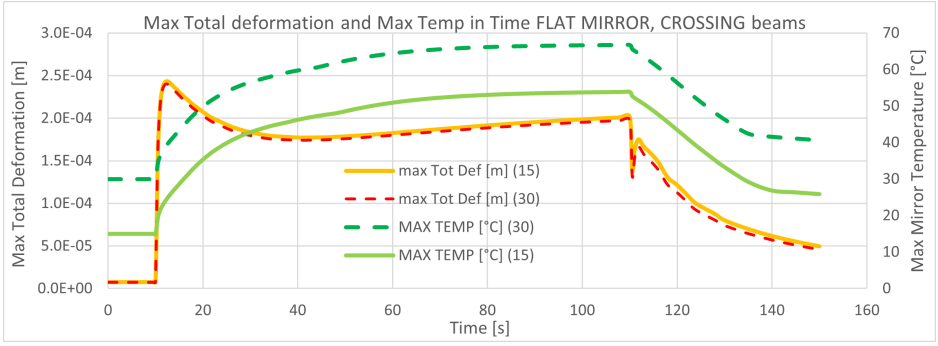

Figure 6.46: *Graph of the trends of the maximum total deformations and temperatures over the time with two water inlet temperatures for the crossing flat mirror.*

The structural results are interesting since, despite the big difference in the trends of the temperature considering two different water inputs, the total deformations are very similar, in both beam configurations. Despite the higher temperature reached in configuration crossing, the relative maximum total deformation is lower than parallel most of the time

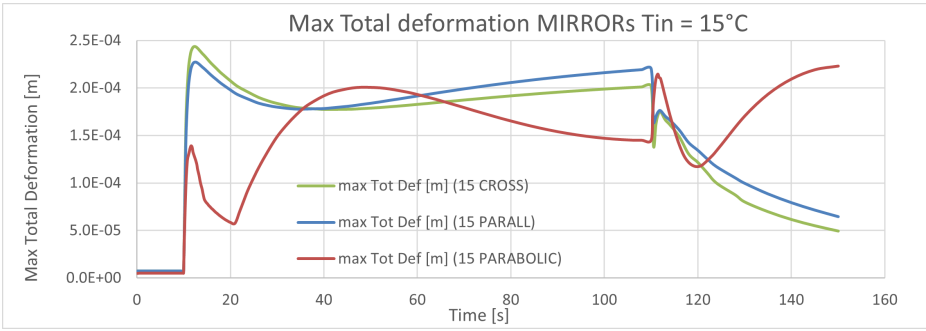

Figure 6.47: *Graph of the trends of the maximum total deformations over the time with a water inlet temperature of 15°C.*

(fig. 6.47).
Neglecting the initial peak, due to the highest gradient (in a short initial transient) on the flat mirror, the final instant (110 s) seems to be a good point of analysis and comparison, in fact, even the highest value of the parabolic configuration (recorded at 44s), of 0.198 mm (tab. 6.7), is lower than those reached at 110s in the flats (tab. 6.10).
The flat mirrors present an increment of the maximum total deformation at 110s of $\sim 50\%$ with respect to the parabolic mirror.

Table 6.10: *Maximum total deformations at 100s for all the mirrors internal to the corridor.*

Max Tot def (110s)					
PARALLEL FLAT		**CROSSING FLAT**		**PARABOLIC**	
0.216 mm (30°C)	0.220 mm (15°C)	0.198 mm (30°C)	0.202 mm (15°C)	0.140 mm (30°C)	0.145 mm (15°C)

Another consideration concerns the evident difference in the trends between the parabolic and flat mirrors. This is caused by the geometry: the temperature gradients generated in the parabolic mirror, and the curvature of the superior layer produce not trivial deformed structure. To highlight this problem, figure 6.48 shows how the parabolic mirror deformation is completely opposite to the flat one on the major axis.

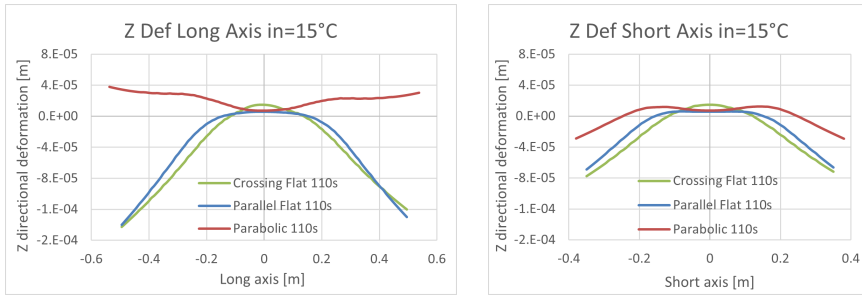

Figure 6.48: *Graphs of the Z directional deformations on the major axis (left) and minor axis (right) at 110 s comparing all the mirrors internal to the corridor.*

6.5 Update of thermal load conditions for MBTL mirrors

In this section the update of the calculations for the reduction of the gyrotron's maximum power and the mirror's absorption coefficient, are presented.
Until now, for the MBTL, these values have been considered as high as possible, to remain widely conservative in the mirror design. But considering the worst condition for all the parameters isn't truly realistic. Therefore, to relax the conservative conditions and simulate more realistic configurations, it was decided to decrease the value of the beam power and the absorption coefficient, as reported in tab. 6.11.

Table 6.11: *Thermal conditions evolution.*

	Q [MW]	**A [Cu]**	$T_{W_{in}}[C]$
Old parameters	1.5	0.21 %	15
New parameters	1.0	0.14 %	15

New conditions lead to lower thermal load, as visible in the tab. 6.12. The other parameters and simulation inputs remain equal with respect to the previous analyses, so it is possible to show directly the new results .
As visible from fig. 6.49 and tab. 6.13, the scaling of the thermal load involves the scaling of the resulting temperatures. A decrement of the Q of 33 % produces a decrement of the maximum temperatures of the mirror at 100 s between 35 % and 40 %.

Table 6.12: *Microwave load parameters for mirrors internal to the corridor.*

	A	$P_{abs\ MAX}[MW/m^2]$
Parallel FLAT	0.14 %	0.082372
Crossing FLAT	0.14 %	0.076373
Parabolic	0.14 %	0.063755

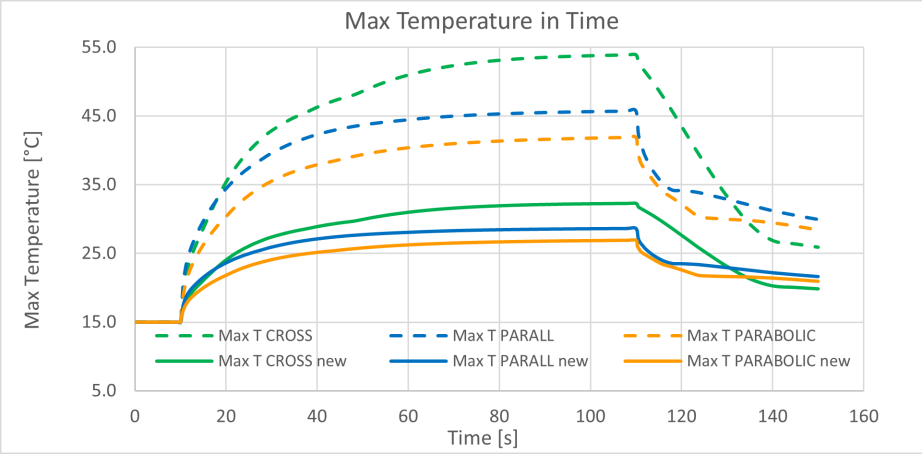

Figure 6.49: *Graph of the trends of maximum temperatures over the time comparing old and new parameters for all the mirrors internal to the corridor.*

Table 6.13: *Maximum temperatures for all the mirrors internal to the corridor, comparing the results with old parameters.*

End of shot: t = 100s Max Temperature [°C]	**Old parameters**	**New parameters**
Parallel FLAT	45.8 °C	28.7 °C
Crossing FLAT	53.9 °C	32.3 °C
Parabolic	41.9 °C	26.9 °C

In this case, the improvement of the thermal results also involves the structural results. Considering the reference instant of 100s, here the maximum total deformation decreases by approximately 54 % for each mirror (tab. 6.14). Fig. 6.50 shows the trends of the maximum total deformation over time for the analyses with new parameters, compared

to the configurations with the old parameters. As visible, the decrease occurs over the entire time interval.

Table 6.14: *Maximum Total deformations for all the mirrors internal to the corridor, comparing the results with old parameters.*

End of shot: t = 100s Max Tot Def [mm]	**Old parameters**	**New parameters**
Parallel FLAT	0.216 mm	0.100 mm
Crossing FLAT	0.198 mm	0.091 mm
Parabolic	0.145 mm	0.065 mm

Figure 6.50: *Graph of the trends of maximum total deformations over the time comparing old and new parameters for all the mirrors internal to the corridor.*

At the end of these simulations, the deformed reflective surfaces are passed to the design group, to be analysed with GRASP software, to assess how the non-idealities affect beam propagation.
The exchange is performed with excel files reporting the final positions of the superior surface nodes, after the deformation. So, with them, it is possible to reconstruct a cloud of points, representing the deformed reflective surface.

6.6 Design of MBTL mirrors external to the corridor

The last part of the activity about the MBTL concerns the mirrors outside the corridor. Such mirrors are similar to the others, reflecting multi-beams, but smaller and characterized by different thermal loads. Changing the geometry, in this case, the new analyses need new models. So, the modelling process must necessarily start from the production of the new CAD models, to the modifications necessary to have a structure as modular as possible, to permit the realization of the optimal structured mesh as seen in section (6.4.1.1).

For a complete analysis of a sequence of mirrors, 4 configurations must be studied: 1 parabolic mirror, 3 flat mirrors (two with parallel beams and one with crossing beams). Two CAD models are developed: one for the parabolic mirror, one for the flat one. The 3 flat mirror configurations differ only in the thermal load.

6.6.1 CAD models of the external mirrors

The parabolic mirror is similar to the one internal to corridor. Its features are explained in 6.2.1. The difference is about the geometrical dimensions with a minor radius of 350 mm, a major radius of 495 mm and a focal length of 2300 mm. Fig. 6.51 shows the mirror in the global reference system with the generatrix parabola and the dimensions of F (2300 mm) and ρ (4600 mm).

To distinguish it from the parabolic internal to the corridor, this will be called hereafter parabolic2300.
As far as thicknesses are concerned, it was decided to adopt the same dimensions used for the other mirrors: 2 cm as the minimum total thickness, which includes the 4 mm minimum thickness of the cover layer (fig. 6.52). The definition of the cooling channel follows the base reported in section 6.4.1.1: two spiral channels with one inlet in proximity of the heat flux peak and two outlets. But in this case the angular ranges are different: the internal spiral is $2\pi - 8.5\pi$ and the external spiral is $8.5\pi - 20\pi$. The external outlet is shifted on the y-axis. As presented in section 6.2.5.2, the definition of the diameters of the semi-circular sections depends on the

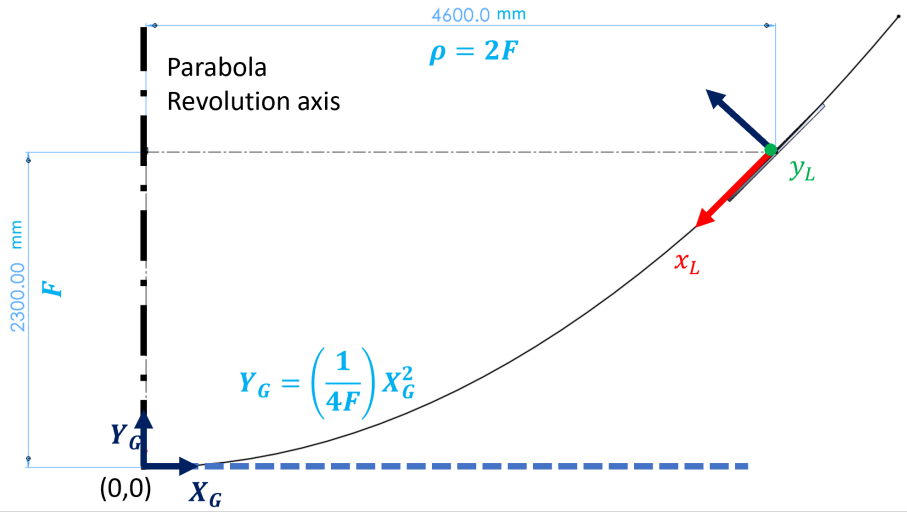

Figure 6.51: *Parabolic2300 mirror external to the corridor: 2D detail of the cut with paraboloid for the curvature of the reflective surface.*

pressure drops. Using the same 1D model, the diameters are calculated considering equal pressure drops for internal and external circuits. In this case, imposing an internal diameter of 12 mm, the external one has to be of 16 mm.
The material is always pure copper.

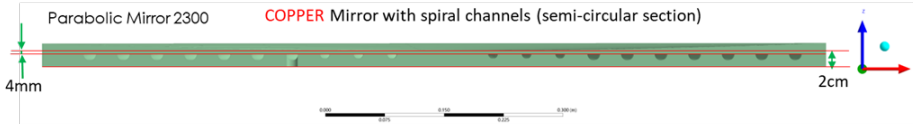

Figure 6.52: *Parabolic2300 mirror external to the corridor: section view.*

The concept of the flat mirror is the same. The only differences are the sizes and the shape of the reflective surface. The dimensions are: 325 mm the minor radius and 460 mm the major radius. The cover layer is flat, with a constant thickness of 4 mm.

The mesh models are mostly structured with a high degree of thickening. The parabolic mirror has 332615 elements and 381996 nodes (Fig. 6.54 left). The flat mirror has 295503 elements and 331819 nodes (Fig. 6.54 right).

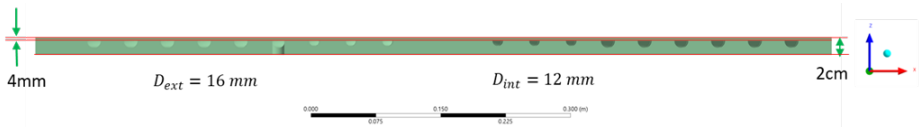

Figure 6.53: *Flat mirror external to the corridor: section view*

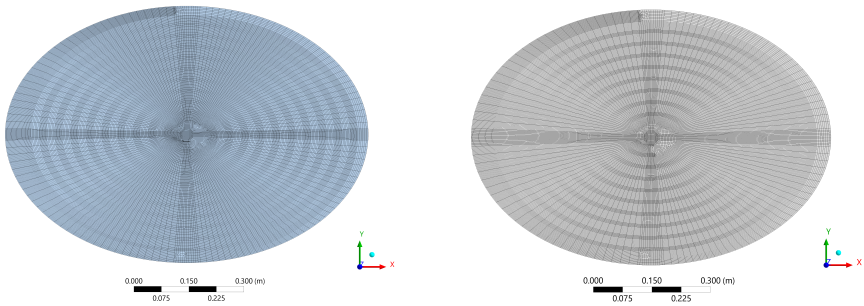

Figure 6.54: *Mesh models of external mirrors Parabolic2300 and Flat.*

6.6.2 Thermal loads of the external mirrors

New thermal loads are defined for the mirrors external to the corridor. As usual they are subject to microwave load, but the parameters like the beam radii (wx and wy), the absorption coefficient (tab. 6.15) and the beams centre location are different. Concerning the beam power and the water inlet temperature the new parameters of section 6.5 are assumed.

Table 6.15: *Microwave load parameters for the mirrors external to the corridor .*

	$w_x[m]$	$w_y[m]$	$P_{abs\ MAX}[MW/m^2]$	A
Parabolic2300	0.14808	0.10471	0.083599	0.15%
1st FLAT PARALLEL	0.08344	0.05900	0.207950	0.16%
2nd FLAT PARALLEL	0.11062	0.78220	0.126426	0.16%
3rd FLAT CROSSING	0.14602	0.10325	0.117604	0.16%

In fig. 6.55 the contour plots of the heat flux are represented. They are very different from each other, due to different beam centres location. Also, the peaks are different, varying from the $\sim 0.08 MW/m^2$ of the parabolic (lowest A) to $\sim 0.2 MW/m^2$ of 1st flat.

Like in the internal mirrors, the flat mirror with crossing beams presents

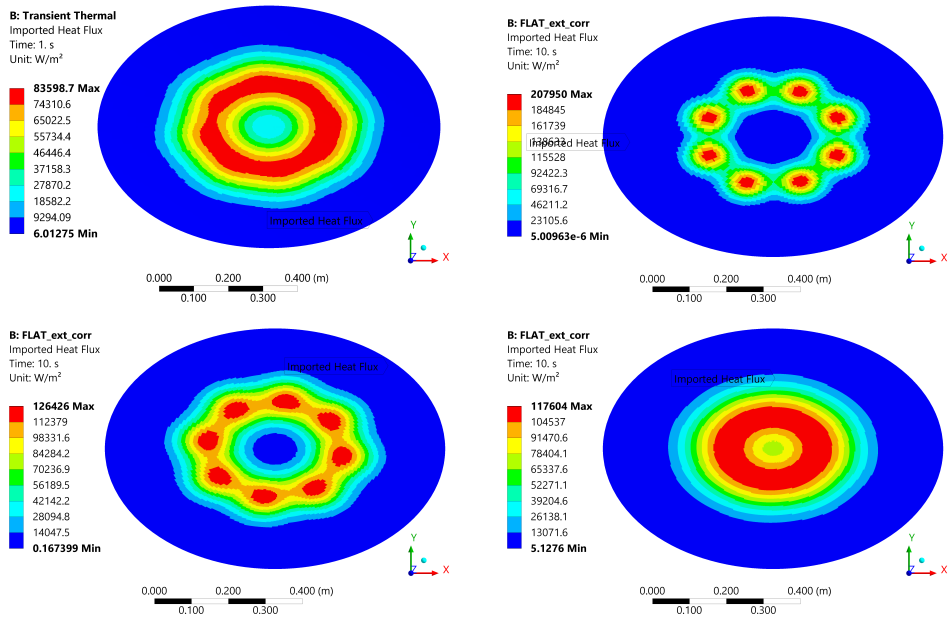

Figure 6.55: *Contour plots of the heat flux on the external mirrors. (Top Left) Parabolic2300; (Top Right) 1st Flat Parallel; (Bottom Left) 2st Flat Parallel; (Bottom Right) 3rd Flat Crossing.*

the most peculiar heat flux distribution: it is again very close to the centre. It can be expected a hot spot in the centre of the the mirror.

6.6.3 Thermo-structural analyses of the external mirrors

The thermal inputs change in function of the new diameters of the models. With still a total volume flow rate of $\sim 20 L/min$ and a new cross-section area, the two flow rates differ from the previous ones, calculated as reported in section 6.2.5.2. So, also the HTC values change (equation 3.2). The new inputs are:

- Volume flow rate: $\dot{V}_{int} = 10.9 l/min$ and $\dot{V}_{ext} = 9.0 l/min$.
- Water inlet temperature $T_{water\ inlet} = 15°C$.
- Water inlet pressure: $p_{water\ inlet} = 10\ bar$.
- Heat transfer coefficient: $h_{int} \cong 12000 W/(m^2 K)$, $h_{ext} \cong 6200 W/(m^2 K)$, constant, calculated considering the water properties at $T_{water\ inlet}$.

In fig. 6.56 and tab. 6.16 thermal results can be seen. The graph represents the trends of maximum temperatures over time. The table shows the maximum and minimum temperatures at the instant of 100 s. The lowest temperatures are related to the parabolic mirror, which, in fact, is the least loaded mirror (lowest maximum P_{abs}). Interesting the trends of the first and third flats, which, despite having a different heat flux distribution, show similar temperature trends. The intermediate results are for the second flat mirror.
Looking at the contour plots of the temperature in fig. 6.57 is visible that the third flat mirror is the only one which presents the hot spot near the centre of the mirror, as happened for the crossing flat mirror internal to the corridor. It depends on the heat flux, which is concentrated in the middle area, due to centres beams locations.

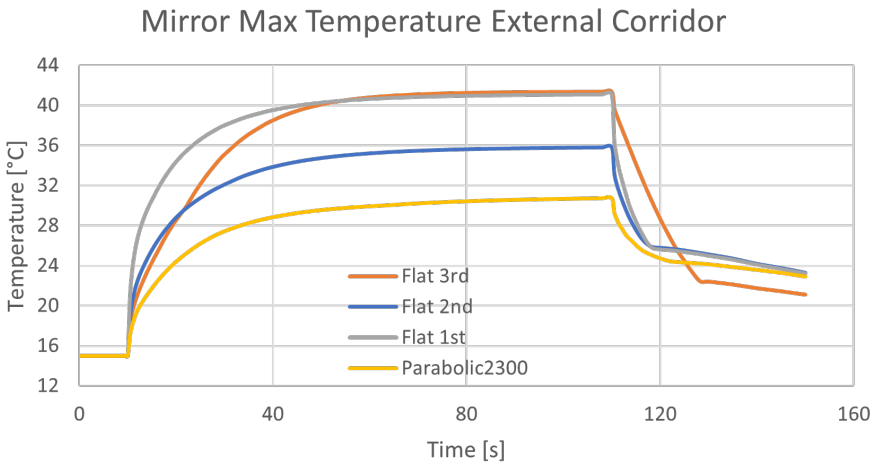

Figure 6.56: *Graph of the maximum temperature over the time for all the external mirrors.*

Before passing to structural results, it's useful to compare the thermal trends of these mirrors with those internal to the corridor. Looking fig. 6.58 it is possible to appreciate that the thermal results are worse than before. With the same thermal conditions, the external mirrors have higher temperatures. This can be explained by considering two conditions. The first one is the geometry: the external mirrors are smaller than the internal ones, so there is less material conducting heat. The second condition is the absorption coefficient, which, in this case, is 0.02% higher for the flats

Table 6.16: *Table reporting the maximum and minimum temperatures recorded on the mirrors at 100s.*

1° shot (t=100s)	$T_{max}[°C]$	$T_{min}[°C]$
Parabolic2300	30.7	22.2
1st FLAT PARALLEL	41.1	23.1
2nd FLAT PARALLEL	35.8	23.9
3rd FLAT CROSSING	41.3	21.5

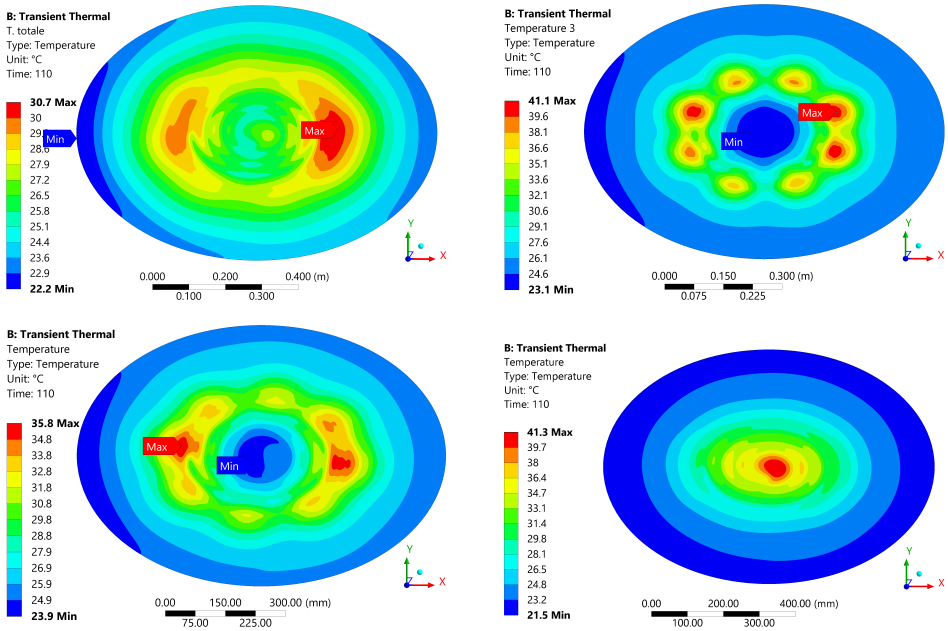

Figure 6.57: *Contour plots of the temperatures on the external mirrors at 100 s. (Top Left) Parabolic2300; (Top Right) 1st Flat Parallel; (Bottom Left) 2st Flat Parallel; (Bottom Right) 3rd Flat Crossing.*

and 0.01% higher for the parabolic. The variation of the absorption coefficients depends on optical calculations, which for different mirrors change its value.

Finally, structural results are presented. Considering the higher temperatures, the deformations found are higher, as expected. Looking at fig. 6.59 and tab. 6.17, the graph of the trend of the maximum total deformation over time shows that the parabolic mirror has the lowest maximum total deformation of the set, and its trend is similar to those already seen.

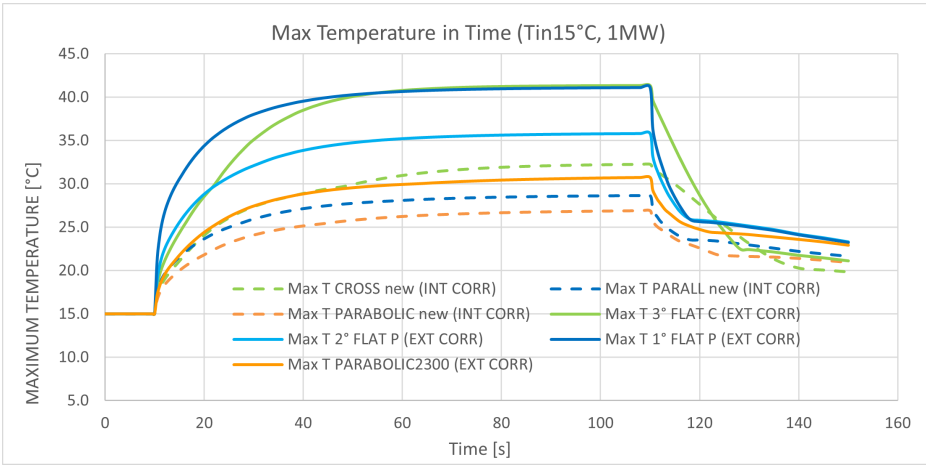

Figure 6.58: *Comparison of the trends of the maximum temperature for the mirrors internal and external to the corridor.*

As for the third flat, which presented the most peculiar temperature distribution, the deformation is lower than that of the parallel flats most of the time. The trends of the parallel flats are very similar, although their temperature trends differ in terms of maximum temperature. The maximum total deformation at 100 s represents well the situation over the entire time range. The highest values come from the parallel flats (1st and 2nd). Fig. 6.60 shows the different behaviour of the parabolic mirror, which, as seen in fig. 6.48 for the external parabolic mirror, shows a deformation in the opposite direction (positive Z).
The increment of the maximum total value of the 1st parallel flat external to the corridor is 26% with respect to the parallel flat internal to the corridor.

Table 6.17: *Table reporting the maximum total deformation recorded on the mirrors at 100s.*

1° shot (t=100s)	**Max Tot def (110s) [mm]**
Parabolic2300	0.087
1st FLAT PARALLEL	0.126
2nd FLAT PARALLEL	0.125
3rd FLAT CROSSING	0.114

The last graph in fig. 6.61 is a comparison of the trends of the maxi-

Figure 6.59: *Graph of the maximum total deformation over the time for all the external mirrors.*

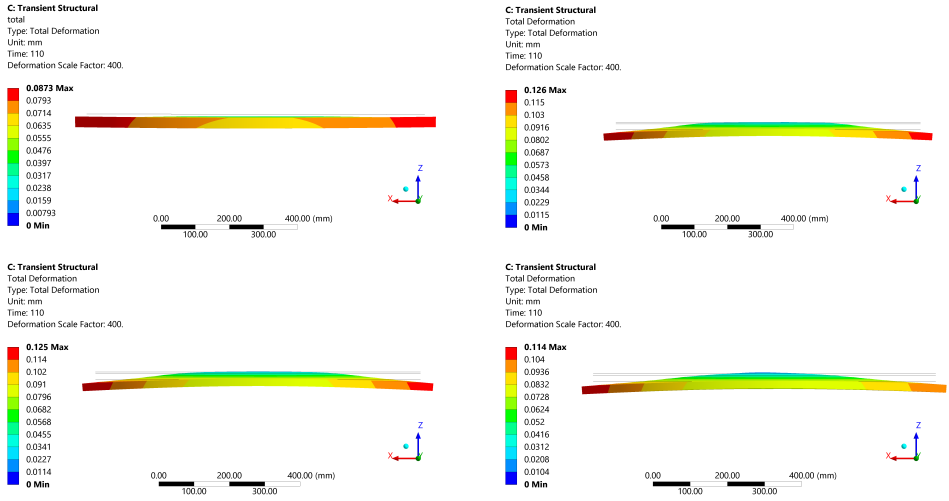

Figure 6.60: *Contour plots of the maximum total deformation on the mirrors external to the corridor at 100 s. (Top Left) Parabolic2300; (Top Right) 1st Flat Parallel; (Bottom Left) 2st Flat Parallel; (Bottom Right) 3rd Flat Crossing.*

mum total deformation among the internal and external mirrors. The last ones have higher total deformation.

The deformed reflective surfaces have been shared with the design group to analyse the beams propagation in terms of microwave propaga-

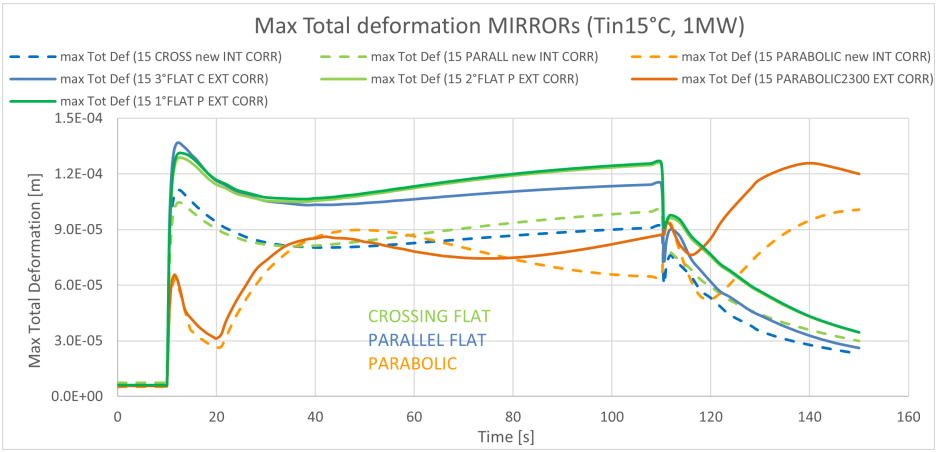

Figure 6.61: *Comparison of the trends of the maximum total deformation for the mirrors internal and external to the corridor.*

tion and spurious mode content.

6.7 Summary of the MBTL mirror design

Starting from the design of the parabolic internal mirror, flat mirrors were implemented in the design, considering a similar geometry, adapted to new characteristics and constraints. In particular, the design of the flat mirrors required the study of two different configurations: with parallel beams and with crossing beams.

The flat mirrors present a different trend of the maximum total deformation, and most of the time is higher than the parabolic one. The highest maximum value of total deformation is recorded for the flat mirror with parallel beams.

An update of the thermal calculations was carried out, due to the change of the water inlet temperature, the maximum power of beam and the absorption coefficient of the reflective surface. A decrement of the Q of 33% produces a decrement of the maximum temperatures of the mirrors at 100 s between 35% and 40%. Instead at 100 s the maximum total deformation decreases by approximately 54% for each mirror.

Considering the final choice of the parameters the internal mirrors have a maximum temperature in the range of (27-32)°C and a maximum total deformation at 100 s in the range of (0.065-0.100 mm). The maximum

temperature is recorded in the crossing flat mirror, instead the maximum total deformation in the parallel flat mirror.
Once the design of the internal mirrors sequence was obtained, the deformed reflective surfaces were used from the DTT researchers for analyses of the propagation in terms of spurious modes content. Similar work was then carried out for the external mirrors. Again, starting from the same basic design concept, new features were adapted to the different mirrors. In this case the sequence was characterized by a parabolic mirror, smaller than the first one and a flat mirror, in three configurations: two configurations with parallel beams and one configuration with crossing beams.
The mirrors external to the corridor have a maximum temperature in the range of (30-41)°C and a maximum total deformation at 100 s in the range of (0.087-0.126 mm). They are characterized by different dimensions and heat fluxes, resulting from the fraction of the incident power of the beams.
The results, in terms of deformation, showed that the external mirrors deform more than the others. The maximum total deformation of the external parallel flat mirror is 26% higher than the internal one.
Thus, the optical analysis of the physic group will determine whether the deformations are within the limits, or the mirrors need an optimization to perform better.

In conclusion to have an idea of the improvement of the results, the maximum temperature of the parabolic internal mirror decreased of 28°C and the maximum total deformation of 0.075 mm.

The herein presented results are reported partly in a poster presented at the conference 32nd Symposium on Fusion Technology (SOFT) 2022 and in the journal publications [21] and the studies submitted [60].

Chapter 7

DEMO

This chapter presents the activity related to the DEMO facility. Before presenting the work elaborated in the context of this machine, DEMO is presented.

One of the most important steps of the EUROfusion roadmap [6] is the realization of an EUropean DEMOnstration fusion reactor, called EU-DEMO. It has the aim of generating around the middle of the century, several hundred MWs of net electricity and operating with a closed tritium fuel-cycle [61]. The objective is the production of 500 MW of electrical power, corresponding to a thermal output of about 1500 MW.
DEMO will be between ITER and the commercial power plant. It will demonstrate first electricity production by fusion, with two additional goals compared to ITER: electricity production and fuel self-sufficiency. It will mark the very first step of fusion power into the European energy market by supplying electricity to the grid. The main objectives are [6]:

- DEMO will breed its own tritium, which is part of the fusion fuel;
- DEMO will demonstrate materials suitable for handling the fluence of neutrons produced during the fusion reactions;
- DEMO will demonstrate safety and environmental sustainability, and sufficient technology to allow a first commercial power plant to be constructed.

The pre-concept design phase of DEMO is focused on different design integration issues [62]. The EUROfusion consortium is conducting detailed studies on different issues and aspects, dividing the studies in Work

Packages. One of them is the work package "Heating and Current Drive" (WPHCD), which is developing the conceptual design and the R&D of three HCD systems: the neutral beam system (NBS), ion cyclotron system (ICS) and electron cyclotron system (ECS).
The functions devoted to the heating and current drive system are: plasma breakdown, plasma ramp-up to the flat-top where fusion reactions occur, the control of the plasma during the flat-top phase, and finally the plasma ramp-down [14]. A total of 130 MW of power has to be provided to the plasma as additional heating power.
The EU-DEMO project was in a Pre-Concept Design Phase during 2014-2020, meaning that in some cases, the design values of the device and the precise requirements from the physics point of view were not yet frozen [14]. One of the last approved baseline design [22] has a reference scenario that foresees 2 h pulsed machine with a duty cycle pulse/dwell ratio of 2 h / 10 min, ∼18 MA of plasma current, a major radius of the machine of 9 m and the on-axis maximum toroidal field of 5.9 T.

7.1 DEMO ECRH system

With reference to [22] and [63], a brief description of the DEMO ECRH is done.
The system (fig. 7.1), configured with high modularity, is organised in basic units: the launcher, inserted in the equatorial port; the transmission line, organised in clusters, with two clusters reserved for each port; the gyrotron subsystem, organised in clusters equal to those of the transmission lines.
Considering 15% transmission losses and 2 MW power for each beamline at the output of the gyrotron subsystem, a total of 6 launchers powered by 12 clusters of 9 gyrotrons each are needed.
Each launcher consists of 4 mirror antennas capable of launching respectively 3, 8, 8, 3 beams (22 beamlines).
The transmission line is partly quasi-optical. In the Tokamak building, corrugated waveguides are the preferred choice. Outside the Tokamak building the beams of each cluster are transmitted jointly by a multi-beam quasi-optical confocal transmission line 100 m long, similar to the one of the stellarator Wendelstein 7-X (W7-X), with alternating plane and parabolic mirrors in a specific configuration. The line, with excel-

lent optical performances ($< 0.1\%$ beam coupling losses) and intrinsically broadband, is evacuated to reduce maintenance, transmission losses and risk of arcs.
The reference source is a gyrotron capable to operate at two different frequencies (170 GHz and 204 GHz) with 2MW power level.
The whole ECS is thus composed by 108 gyrotrons, $\sim 216MW$ of power installed and $\sim 130MW$ delivered with high reliability to the tokamak.

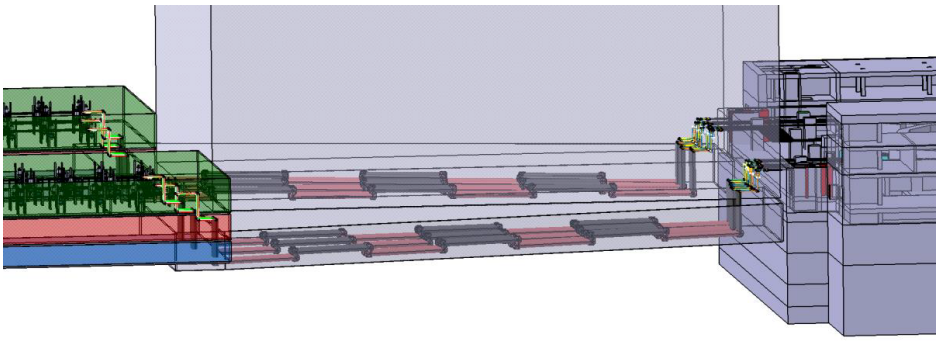

Figure 7.1: *CAD representation of the gyrotron halls (left), the multi-beam transmission lines (centre) and the optical connections to the waveguides in the Tokamak Hall (right).*

7.2 DEMO activity

The activity about DEMO is related to a deliverable of a task of the WPHCD. It concerns the focusing mirror of the multi-beam transmission line (fig. 7.2) of DEMO ECRH system.
A preliminary conceptual design of the mirror has been realized, considering also its supporting structure. Being the mirror subject to thermal loads coming from the microwave reflection, it must be cooled. For the mirror construction, a cooled metallic layer backed by a honeycomb structure seems to be a good solution to reduce the weight and at the same time the deformations. A preliminary shape of the cooling circuit has been designed.
For the supporting structures three different proposals have been considered and a part of the enclosure of the mirrors in the line has been proposed, taking into account the geometrical constraints of the mirrors.

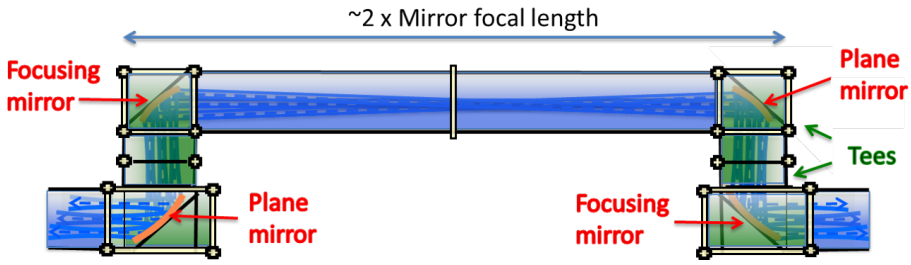

Figure 7.2: *Schematic image of a part of the MBTL, comprehensive of 2 plane mirrors and 2 focusing mirrors [64].*

7.3 DEMO ECRH Focusing mirror

The mirror taken into analysis is the focusing one, that has an elliptical shape and a parabolic curvature on the front face (that reflects the microwave beams). Its function is similar to that one of the focusing mirror of DTT, already presented.
Its dimensions are extrapolated by the optical calculation for the reflection of the beams. They are: 1365 mm x 965 mm, respectively the major and minor diameter of the ellipse (fig. 7.3 left).

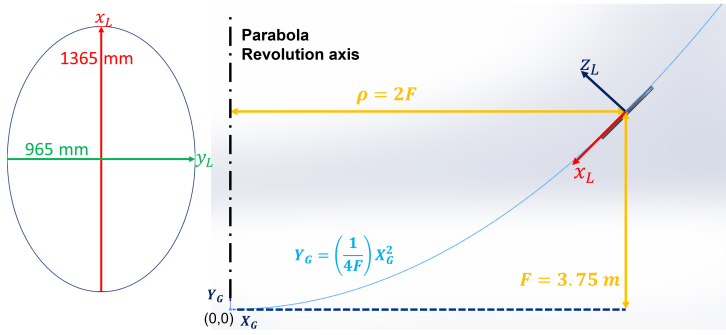

Figure 7.3: *(Left) Focusing mirrors dimensions. (Right) CAD representation of the DEMO parabolic mirror.*

The procedure of realization of the mirror CAD model is the same seen for DTT parabolic mirror (section 6.2.1).
Considering the transmission line direction, and so the incidence beams direction, the mirror is rotated of 45° with respect to the horizontal plane. The parabolic curvature is given by a cut of a flat mirror with a paraboloid that has the revolution axis rotated of 45° respect of the major radius of

the mirror, i.e. it is vertical. The planar distances between the paraboloid vertex and the centre of the mirror are the focal length (F = 3.75 m) on the vertical and a length of 2F on the horizontal (fig. 7.3 right) [18]. As visible in fig. 7.3, x_L, y_L and z_L are the axes of the Local coordinate system on the mirror, to be distinguished from the Global reference system in which the parabola is defined, with the equation 6.1.

The development of the mirror design started from the W7-X experience. As reported in [29], the multi-beam and single-beam mirrors of the transmission line of the ECRH are made in similar way. They have a 60-70 mm thick honey-comb structure of stainless steel covered by a thin (2 mm) layer of electro-formed copper. The foreseen cooling channel has the shape of a spiral in order to cover well all the heated area, and it is dug inside the stainless-steel bulk, under the copper.
On the base of the W7-X experience, the following design was proposed. For the Parabolic mirror of EU DEMO ECRH, some thicknesses are chosen for first attempt. In particular, the bulk thickness is chosen of 60 mm and the cover layer has a minimum thickness of 2mm in the centre (fig. 7.4). Due to parabolic cut (symmetrical with respect to x_L axis), the maximum thickness of the layer on the y_L axis is 12.977 mm in both external edges (in $y_L = \pm 965/2mm$). The maximum thicknesses on the x_L axis are visible in fig. 7.4.

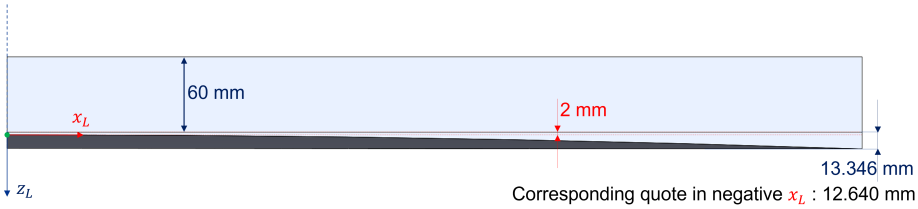

Figure 7.4: *Half mirror (Positive x_L) and relative quotes.*

The honeycomb structure of W7-X mirrors is considered for DEMO mirror, even if, due to the need of avoiding trapped volumes under vacuum, the honeycomb cell must be open.
This choice can remarkably reduce the weight of the mirror (that has large dimensions), guaranteeing a good stiffness, necessary to reduce the deformations of the mirror due to thermal expansion during the activity.

The problem in fact is that, although the reflection efficiency is very high (above all in case of copper coating), a little part of the power is absorbed by the mirror. This leads to a high heating of the mirror surface, and to thermal expansions and deformations. If this kind of thermal expansions couldn't be a problem from a structural point of view, on the other hand, they could lead to small deformations that can produce important beams deflection affecting the transmission efficiency. So, it's important to reduce as much as possible the mirror temperature designing a good cooling system, but also choosing the best materials and geometrical features to reduce thermal expansions. The honeycomb structure goes in this direction.

The chosen honeycomb is composed of a repetition of hexagons circumscribed to a circumference of 6 cm of diameter. The distance between two adjacent hexagon-centres is always 6.5 cm. The whole structure appears as in fig. 7.5. The dimension of the honeycomb shell is taken as a first reference and is not optimised. For the optimization, in addition to mechanical and feasibility considerations, an evaluation of the overall surface exposed to vacuum may be required, since it may contribute to the total outgassing in the transmission line vacuum enclosure.

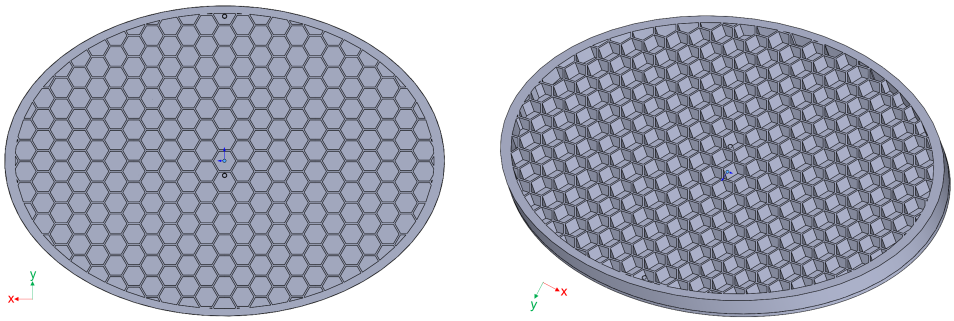

Figure 7.5: *Honeycomb bulk structure.*

Inside the bulk structure a preliminary cooling channel has been dug. It has a semi-circular section with a diameter of 1.2 cm. The shape of the channel is an elongated spiral following the elliptical shape of the mirror. The spiral pitch is 3 cm for the minor axis and for the major axis 3 cm multiplied by the ratio between the ellipse radii. The angular range of the spiral is $(\pi - 30\pi)$ (fig. 7.6). The cover layer closes the channel.

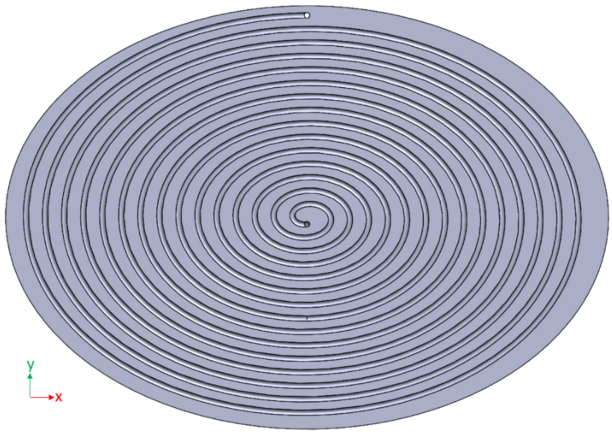

Figure 7.6: *Cooling channel dug inside the mirror with a spiral path.*

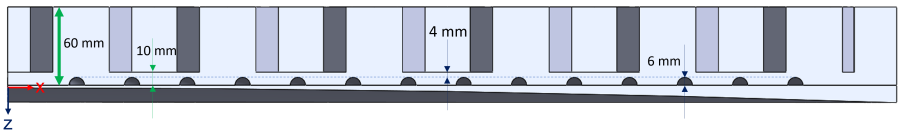

Figure 7.7: *Half mirror: section view (positive x_L), quotes definitions.*

The honeycomb extends for 5 cm of the bulk thickness, the remaining 1 cm is dug for 6 mm by the channel.
This design foresees a channel extending on the flat stainless-steel surface. So, the distance between the surface and the channel increases with the distance from the centre, due to curvature of the mirror. In case of need to improve the cooling, the channel can be brought closer to the surface, even if this means more difficult realization, for example by electroforming.
The manufacture of the honeycomb structure is an aspect not yet considered. Generally, this kind of structure can be commercial, produced by expansion method or corrugation method, but it can be realized also with additive manufacturing (3D printing).
In this phase of design, the materials are the same of W7-X [3]: the bulk in 316L (N)-IG Stainless Steel and the cover layer in Pure Copper.

7.3.1 First structural analysis of the mirror

With the scope to have a first evaluation of the mirror weight and of the deformations induced by gravity for different concepts and verify the advantages of the choice of the honeycomb, some structural analyses on the mirror have been carried out. The objective is to verify if and how much the honeycomb structure permits to reduce the mirror deformations. So, three different mirrors (fig. 7.8) have been compared under the same constraints:

a) Mirror with honeycomb structure.

b) Mirror with the same weight and density of a), without honeycomb, therefore thinner than a).

c) Mirror with the same geometrical dimensions of a), without honeycomb and therefore massive.

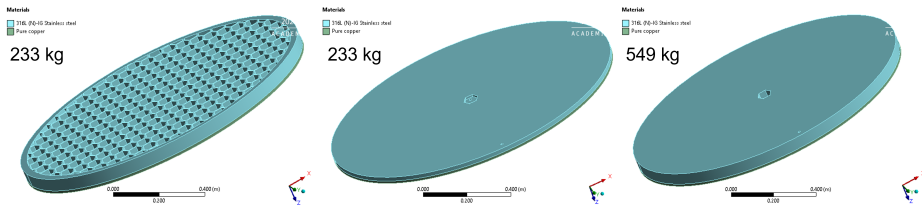

Figure 7.8: *Three mirrors: left a), centre b), right c).*

A simplified sensitivity analysis for the mesh has been done. It brought to choose a general element size of 2mm for all the cases. The elements are tetrahedrons of linear order. The average aspect ratio (mesh quality parameter) obtained for the three cases is $\sim$ 2.2, confirming the good quality of the mesh.
The structural constraint used for the analysis is a fixed support on the back central hexagonal face, with distance of 1.2 cm from the superior face (fig. 7.9).

The load is the standard Earth Gravity along the vertical axis, rotated of 45° respect to the z local axis (fig. 7.10).

7.3.1.1 Structural Results

The simulation results show that the chosen honeycomb structure permits to keep an adequate stiffness, reducing the weight at about half of a

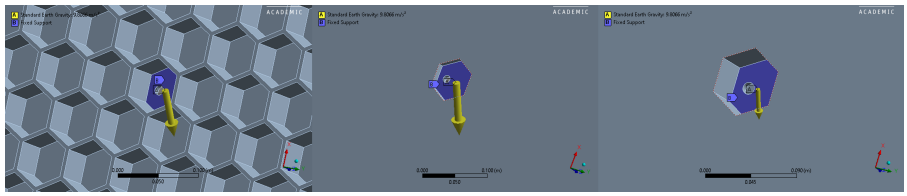

Figure 7.9: *Fixed support in three mirrors: left a), centre b), right c). The yellow arrow is the application of the Gravity.*

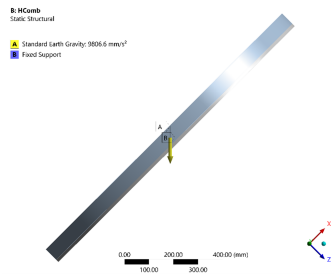

Figure 7.10: *Standard Earth gravity Load.*

massive mirror of the same thickness.
The graphs in fig. 7.11 show the directional deformation out of the mirror plane (along the z local axis) of the major and minor diameters of the superior surface of the mirror.

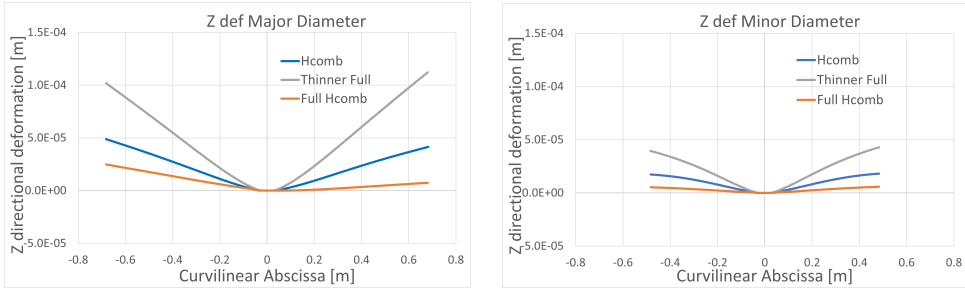

Figure 7.11: *Graphs of the trends of Z_L deformation along the major (left) and minor (right) diameters.*

The curves of the deformations of the different mirrors are represented. Honeycomb (in blue on the graphs) represents an intermediate solution between the case of a full mirror with a weight of $\sim 550\ kg$ (orange lines), with high stiffness and lower deformations, and the case of a thinner full

mirror of 233 kg (grey lines). It has got the same weight of the thinner mirror, but better structural performance, being a factor of two less deformable. In the honeycomb solution the maximum Z_L directional deformation respectively on the major and minor diameters are $\sim 0.05\ mm$ and $\sim 0.02\ mm$.
Such values aren't now indicative from an optical point of view. Further analyses, considering the gravity and thermal effects will be carried out, in order to evaluate the deformations. The deformed surface will be object of the studies that the research group will execute to analyse the beam deflection. They will address the mirror design.

7.3.2 Enclosure for a couple of mirrors

The TL conceptual design foresees confocal mirrors to contain the divergence of the beams dimensions and it requires a layout with a dog-leg, for the alternance of the parallel and crossed beams.
In this phase the part of the enclosure of a single couple of mirrors is considered, starting from a simple cylinder with vertical axis and recalling that the evacuated setting needs high-vacuum flanges of large dimensions, so that the needs of construction, maintenance, inspection, evacuation and the costs call for choosing a minimum possible size of the enclosure.

In addition, the optical design requires a distance between the mirrors of 1000 mm.
Recalling the dimension of the mirror ($1365\ mm \times 965\ mm$), it can be inserted ideally at 45° inclination in a cylindrical enclosure with minimum diameter equal to the minor mirror diameter, since the two dimensions are linked by the following formulation:

$$1365\ mm \cos(45^\circ) \cong 965\ mm$$

The biggest standard commercially available vacuum flanges in this range of dimensions are found in standard ISO-K, in particular the biggest one has a diameter of 1000 m: DN 1000 ISO-K, that could be suitable for the top and bottom sealing of the enclosure.
Another flange is necessary in the back of the mirror to permit the inspection and eventual alignment. For this necessity is foreseen the flange DN 650 ISO-K. The alignment is foreseen at the installation and verified at the line openings.

In addition to the inspection flanges, other flanges with feedthroughs for diagnostics and cooling will be added at the sides.
In figure 7.12 the enclosure dimensions are reported.

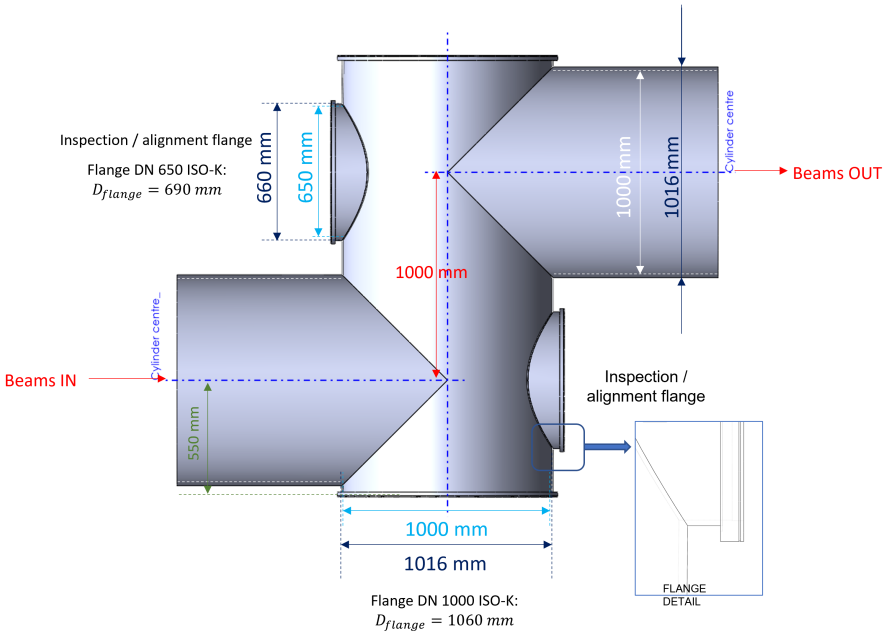

Figure 7.12: *CAD representation of a part of the enclosure of two consecutive mirrors.*

The enclosure could be cooled by external pipes or cooling clamps placed in specific points. The clamps may be needed close to the mirrors where spillover can occur. The positions and characteristics will depend on the released power, to be addressed with future optical calculations.

7.3.3 Modification of the focusing mirror

The thickness of the mirror increases its footprint dimensions and the occupied volume (fig. 7.13), and this happens even more if the mirror is not fixed, but it must be aligned with little rotations.
This will be a recurrent procedure during the activity, in order to accommodate the beam alignment with slight deflections of the mirrors.

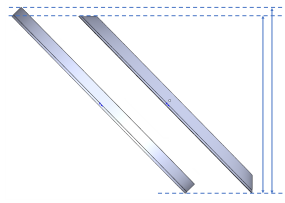

Figure 7.13: *Particular of mirror thicknesses.*

So, the supporting structure must foresee a handling system that permits the rotation of the mirror around its major and minor axis of an angular quantity still to be defined with tolerance evaluations, but preliminary considered to be maximum ± 2 *deg*.
So, the thickness and the position of the mirror, consequently to the rotation, changes the overall dimensions.
For this reason, it is important to reduce the back dimensions of the mirror and smooth its edges to fit to the circular enclosure with a chamfer.
As shown in fig. 7.14 the chamfer is executed with a surface of cut, generated by a smooth surface connection between two ellipses: the green one (1365 mm x 965 mm) and the blue one. The blue ellipse dimensions are obtainable as described in fig. 7.15.

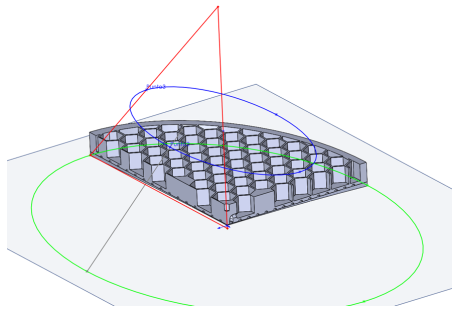

Figure 7.14: *Generation of the cut-surface for the creation of the chamfer.*

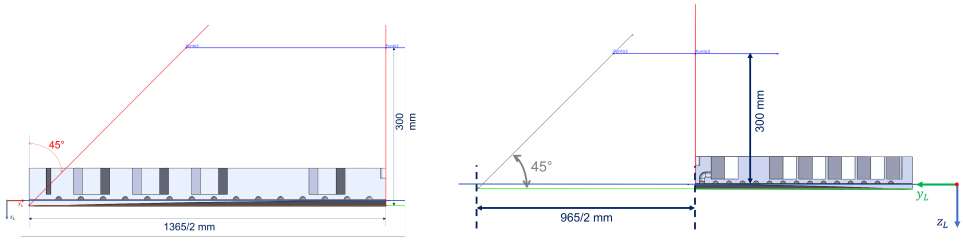

Figure 7.15: *(Left) Dimensions of the long diameter section. (Right) Dimensions of the short diameter section.*

The cut of the mirror is done with the "loft surface" of fig. 7.16.
The final result is shown in fig. 7.17.
To improve the aspect of the mirror, it could be good to reduce the

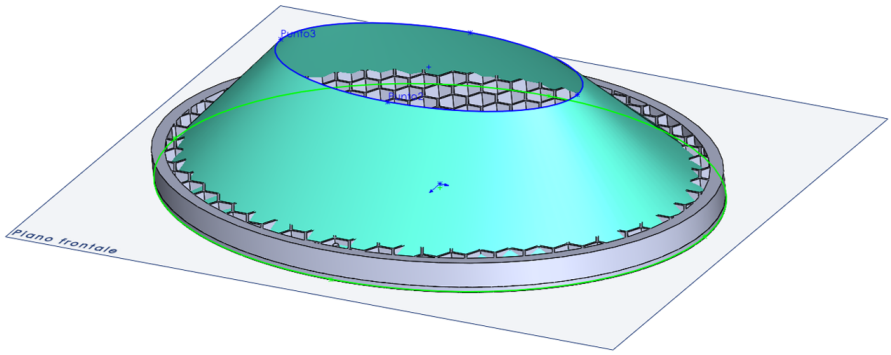

Figure 7.16: *Loft-surface to chamfer the mirror.*

Figure 7.17: *Result of the chamfer on the edges of the mirror.*

dimensions of the ellipse that includes the honeycomb, in order to not have cut edges. The result is visible in fig. 7.18.

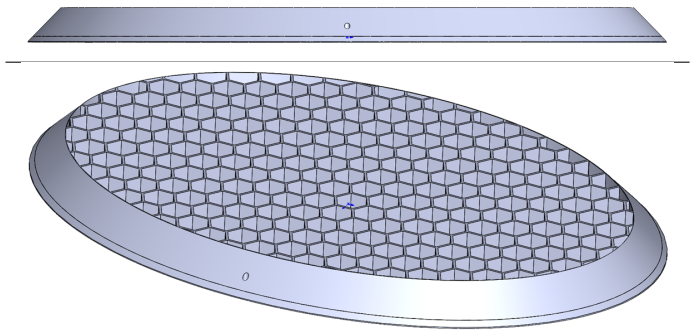

Figure 7.18: *Improvement of the chamfer on the mirror.*

The hole visible on the edge of the mirror is the outlet of the cooling channel.

7.4 Proposals for mirror supporting structure

Three different supporting structures and ways of mounting are considered in this phase. Given the mirror placement and the enclosure geometry, the support arms are supposed to be attached (in some way, not

still defined) at the top and bottom of the cylindrical enclosure. The supporting structure at the bottom is shown in figures, while the one on top is considered as the same, just put upside-down.

7.4.1 Supporting structure with circular rails

This solution foresees two rails for the rotations respectively around major and minor diameters of the mirror ellipse in the plane passing for the mirror surface centre. It allows to adjust the mirror position between pulses along the main axes, according to the necessity to have as much as possible aligned beams.
The support is welded to the mirror in the central back surface. So, in correspondence of the centre, the hexagonal cell must be filled to be connected to the support.
With reference to the fig. 7.19, the support is explained.
The superior part (a) in yellow, is constituted by a circular base, able to slide on a circular guide of part (b) in blue. At the same time (b) has a circular base, able to slide on another circular guide of the part (c) in grey. The bottom circular guide is perpendicular in respect to the superior one and this permits to have independent perpendicular rotations. In this set all the rotations are referred to the same rotation centre. This will be coincident with the centre of the front face of the mirror. As visible in figure 7.19 right, the distance between the front face of the part (a) and the centre is equal to the thickness of the mirror.

The base of the structure, (which is shown in fig. 7.19 in grey colour) must support a plate (2 cm of thickness) in which four spherical screws will be mounted (fig. 7.20). They are adjusting screws for the mirror handling. The plate has four holes to host the screws, located along the major and minor diameters.
The distance between the horizontal screws is 260 mm, whilst between the vertical screws is 450 mm.

The handling can be done for one rotation at the time.
To rotate the mirror around the major axis, the vertical screws must be fixed. The two horizontal screws will be moved. The first one will be unscrewed and then the second one will be screwed. In reverse for the other verse of rotation. To rotate the mirror around the minor axis the procedure is equal.
The screws work in compression. They will be in tangent contact with the

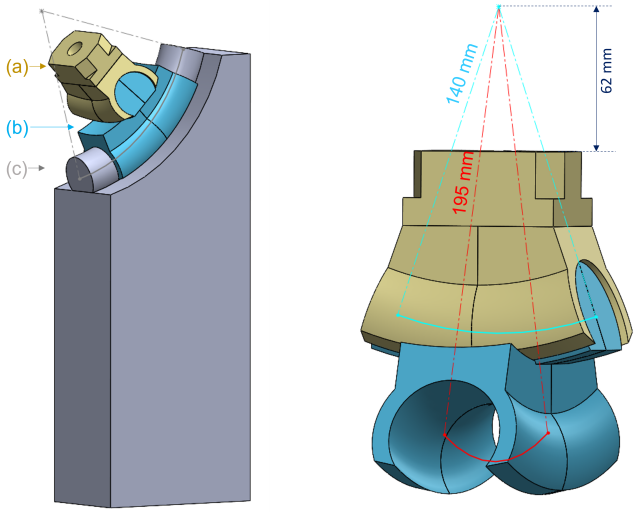

Figure 7.19: *(Left) Three parts of the support ((a), (b), (c)). (Right) Details of parts a) and b) of the support.*

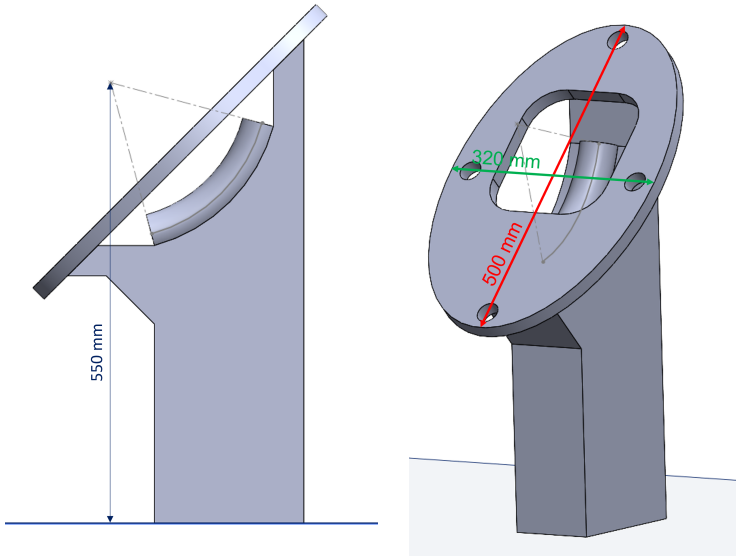

Figure 7.20: *Base of the support with elliptical plate.*

mirror back surface.

Four hexagonal cells, in which they act, mustn't be empty, so another modification on the mirror is done (fig. 7.21). In this figure it is visible

also the filled central cell.

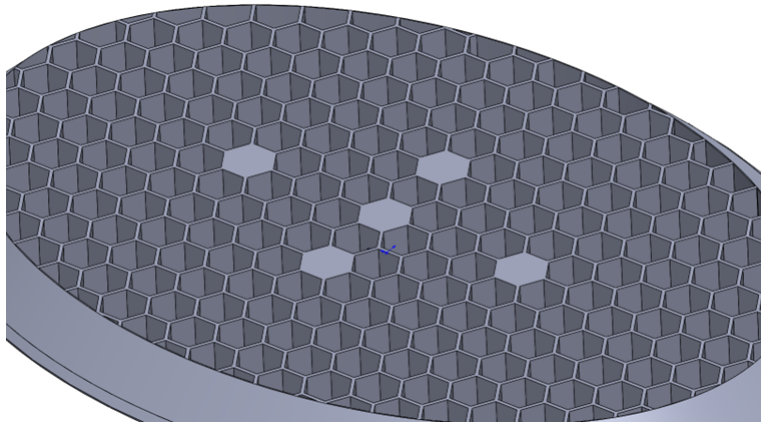

Figure 7.21: *Improvement of the mirror with filled hexagonal cells.*

The mirror and its supporting structure are visible in the following figures (7.22-7.23-7.24).
Fig. 7.22 shows the three reference orientations assumed by the mirror: the nominal one (45°) and ±2° for the rotation around y local axis.
The figure 7.23 shows the three reference orientations assumed by the mirror: the nominal one (45°) and ±2° for the rotation around x local axis. The figure 7.24 shows in another view the rotation around x local axis.

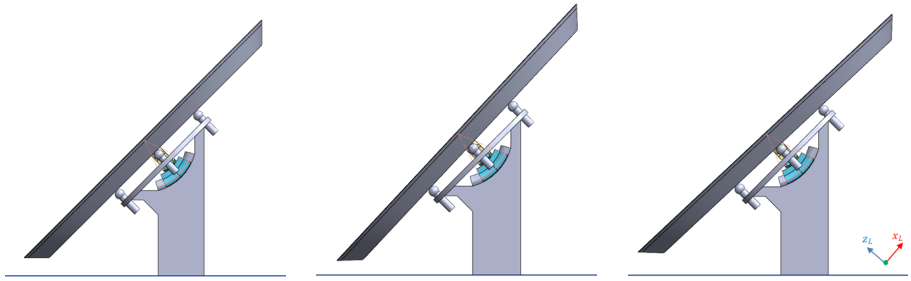

Figure 7.22: *Mirror with the supporting structure in nominal position (left), rotated of -2° around the y local axis (centre), rotated of +2° around y local axis (right).*

In this configuration the last point concerns the feeding circuit and the inlet of the cooling channel.

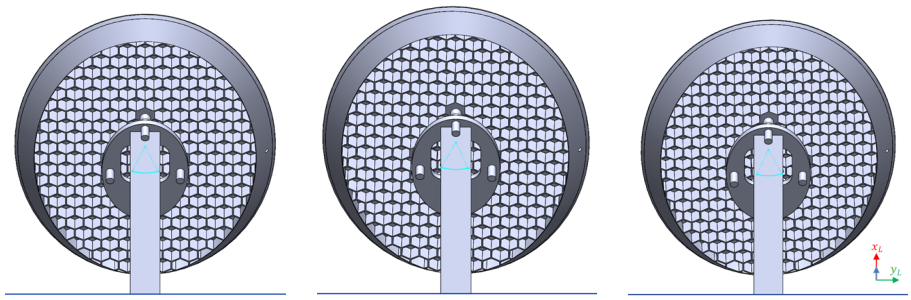

Figure 7.23: *Mirror with the supporting structure in nominal position (left), rotated of -2° around the x local axis (centre), rotated of +2° around x local axis (right).*

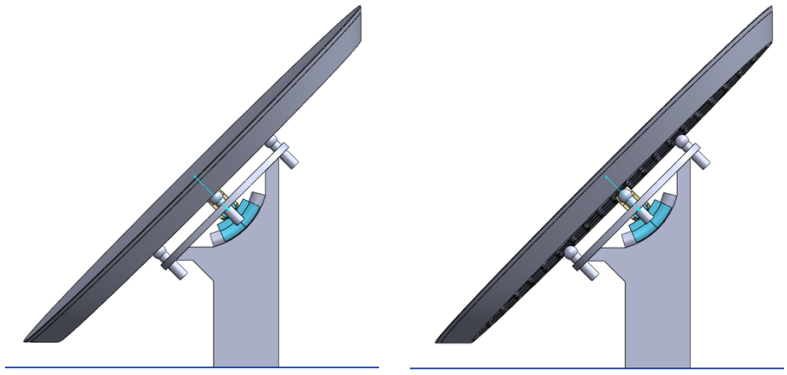

Figure 7.24: *Another view of the mirror rotation around the x local axis: (left) +2° around x local axis, (right) -2° around x local axis.*

The support is welded in the centre, near the inlet of the spiral cooling channel, so it is necessary to change direction of its feeding channel. The result is visible in fig. 7.25.

In fig, 7.26, in yellow it is represented a hypothetical feeding tube (with an inner diameter of 1.2 cm). It crosses the plate of the screws, but needs space in case of rotation. Thanks to the central opening of the plate, the rotation around minor axis isn't a problem. But to avoid interference with the base support in case of rotation around major axis, the centre of the tube must have a distance of 4 cm with the wall of the central cell. An alternative could be to do the last part of the feeding flexible and near the plate a junction to a rigid tube.

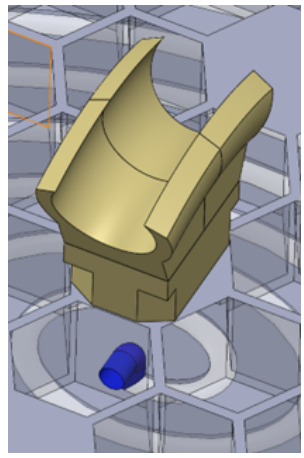

Figure 7.25: *Adjustment of the inlet.*

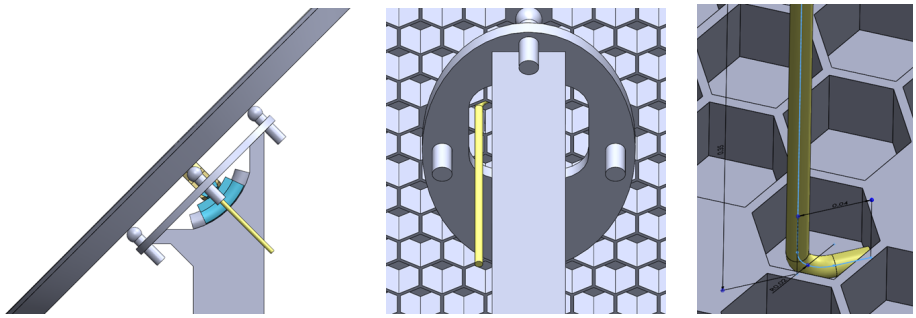

Figure 7.26: *Feeding tube in different views.*

7.4.2 Supporting structure with spherical joint

The second proposal of supporting structure foresees a spherical joint located in the back centre of the mirror. The spherical joint, as before, permits to have the centre of the rotation coincident with the centre of the front surface of the mirror and enables both rotations with a single joint.
In figure 7.27 is visible the mirror and the support.

For example, a joint that could be proposed is like a spherical axial joint of SKF GX 20 F [65]: 20 mm bore diameter and 55 mm outside diameter and an overall height of 20mm (fig. 7.28).

The material of the joint SKF GX 20 F is through-hardened and ground bearing steel. The operating temperature range is: -40 to +75

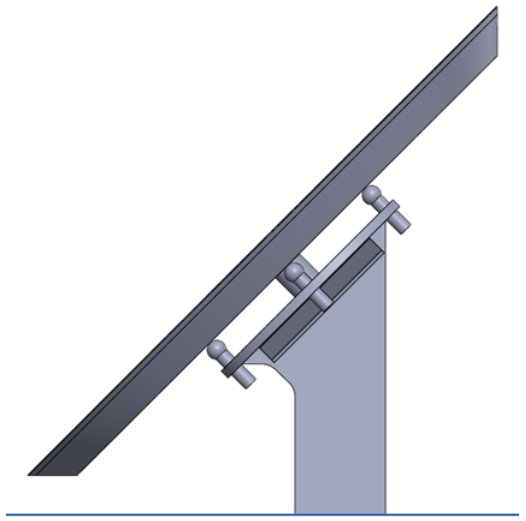

Figure 7.27: *Mirror and supporting structure with spherical joint.*

°C, for brief periods up to +110 °C, with reduced load carrying capacity at temperatures above +50 °C. It will be necessary verify the compatibility of this kind of bearing with the setting conditions: the temperatures and the vacuum.
For the vacuum condition it would be better to avoid the lubrification. Bearings with a maintenance-free steel/PTFE fabric sliding contact surface should be used when lubricant-free operation is specified.

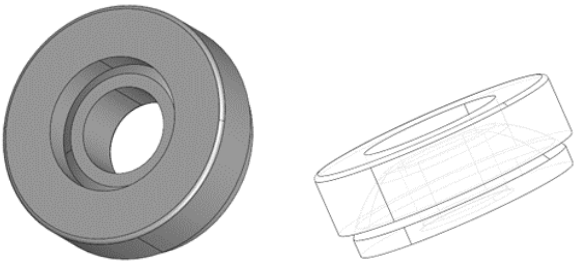

Figure 7.28: *Spherical axial joint SKF GX 20 F.*

For this solution it is necessary to adapt the mirror to the joint. The distance between the sphere diameter centre and the shaft washer back face of the joint is 12.5 mm.

As visible in fig. 7.29 left the central part of the honeycomb must be

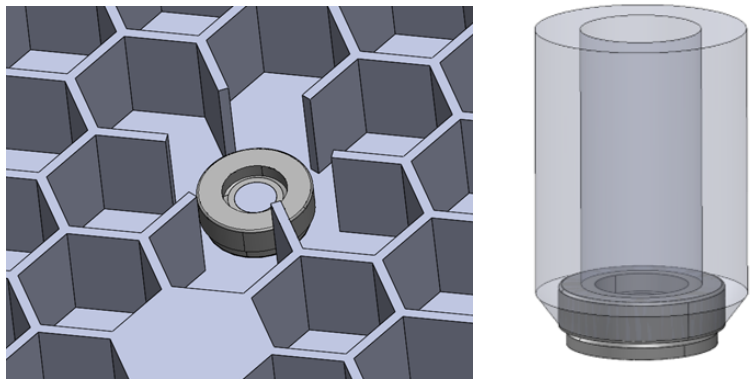

Figure 7.29: *(Left) Mirror detail of the housing of the joint, (right) detail of the pillar between the joint and the base.*

cut to leave space to the pillar that sustains the joint (fig. 7.29 right). To not lose the benefice of the honeycomb in central zone, the cut can be modified as visible in fig. 7.30. The hole has a diameter of 8 cm. This dimension permits to avoid interferences between the arm and the structure during the handling of the mirror.

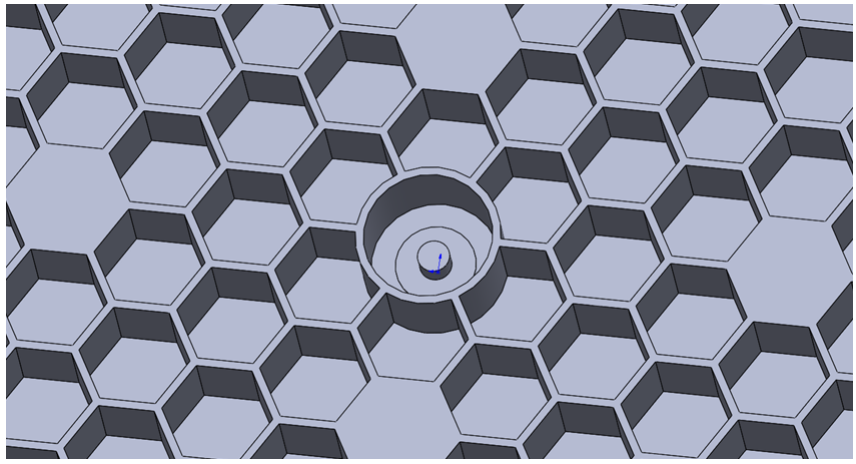

Figure 7.30: *Joint housing adjustment.*

In case of use of this kind of joint it will be necessary to foresee a sealing system to keep together the rings of the bearing. A solution could be a precision spring in compression between the mirror and the outer ring as shown in a representative example in fig. 7.31. It will be included and

considered in the future development.

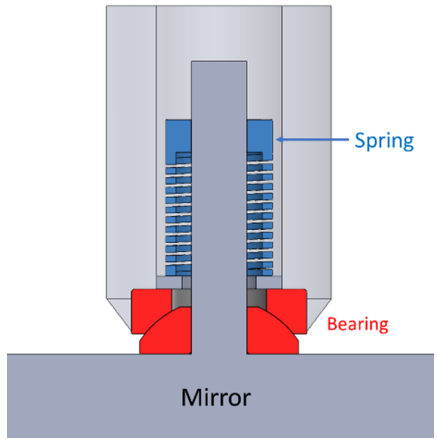

Figure 7.31: *Example of sealing system for the spherical joint.*

As for the previous configuration, the handling of the mirror is done by 4 screws located on a plate directly welded on the base support and reinforced with two lateral ribs (fig. 7.32).

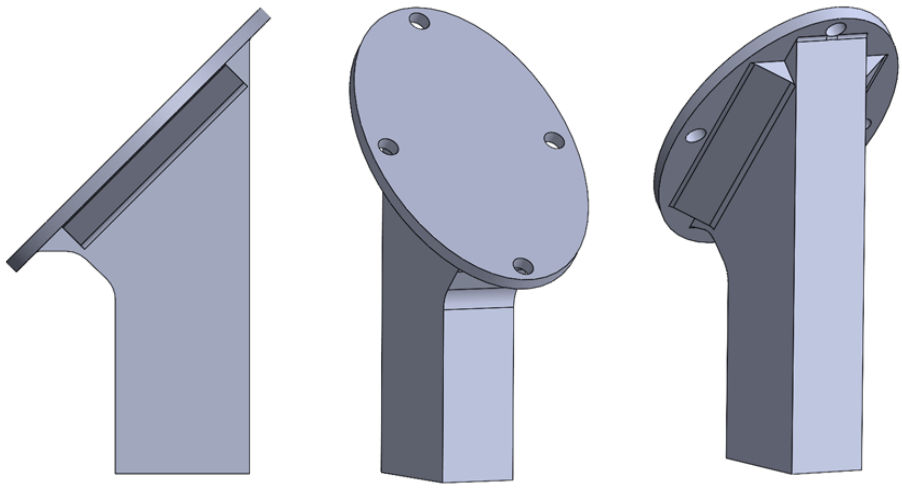

Figure 7.32: *Different views of the base support for the proposal with spherical joint.*

In this configuration a problem concerns the inlet. There isn't space to build the inlet feeding in the presented solution. The start of the spiral

path is in correspondence of the joint (fig. 7.32 left) and there isn't enough thickness between the channel and the mirror back surface (fig. 7.33 right) to provide a solution like the previous case.

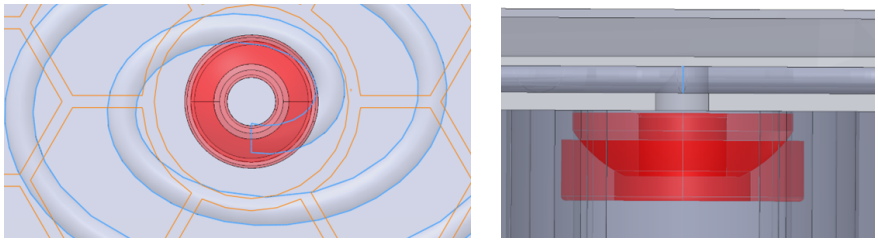

Figure 7.33: *Detail of the interference between the joint and the inlet.*

A solution can be to reduce the tournaments of the spiral path of the channel of $\pi/2$ (the angular range becomes: $1.5\pi - 30\pi$) and create a fitting toward an adjacent cell. The result is visible in fig. 7.34.

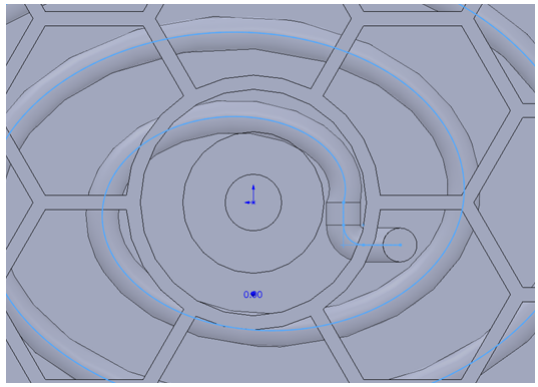

Figure 7.34: *Inlet adjustment for the spherical joint proposal.*

In this case, the plate isn't open in the centre, so the feeding tube cannot cross the plate: another change of direction must be foreseen (fig. 7.34).

In fig. 7.35 and fig. 7.36 the part of the tube represented in orange can be flexible to permit the rotations of the mirror. Instead, the yellow part can be a rigid tube to be connected with the external circuit.

Another aspect concerns the fact that the spherical joint enables also the rotation around the z local axis. So, it will be necessary to foresee a system to block this kind of movement.
The problem of the z rotation has not been addressed for the moment.

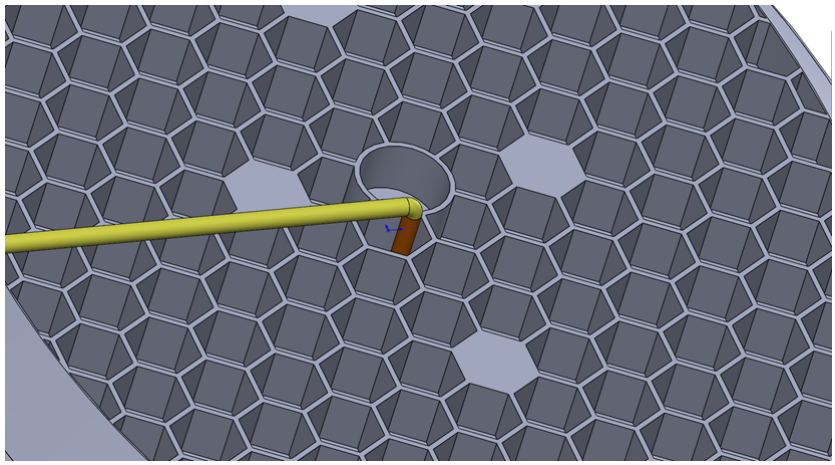

Figure 7.35: *Adjustment to the inlet feeding tube.*

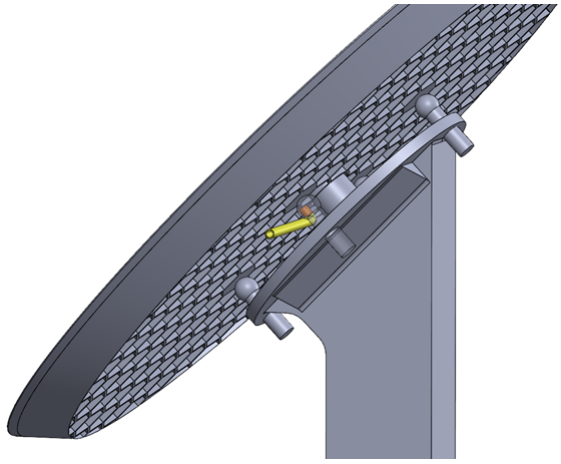

Figure 7.36: *Mirror with spherical joint, supporting structure and feeding tube.*

7.4.3 Supporting structure with cardan joint

The third proposal is visible in fig. 7.37. The use of a cardan joint (fig. 7.38) permits to block the rotation around the z-axis and have mechanism similar to the previous ones (the same base support). But there is a substantial difference. The centre of the rotation, in this case, is not any-more on the front mirror surface, but it is on

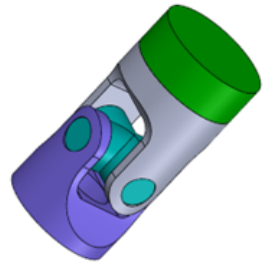

Figure 7.38: *Detail of a cardan joint.*

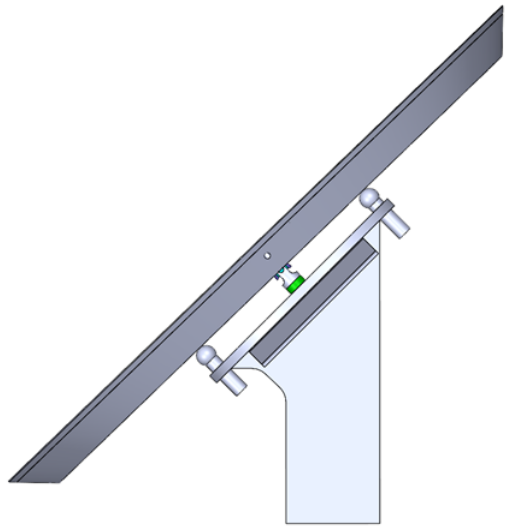

Figure 7.37: *Mirror and supporting structure with a cardan joint. The screws on the short axis of the mirror are hidden to appreciate the joint.*

the back surface, in correspondence of the joint cross. This leads to displacements of the mirror centre of maximum 0.22 cm in vertical and horizontal positions from the nominal position.
This solution needs a more accurate study.

7.5 Enclosure with a couple of mirrors

For a preliminary check and to control possible interferences, two equal mirrors are insert inside the vacuum enclosure. Really, the couple of mirrors will be constituted by a focusing and a plane mirror. But the plane mirror is smaller than the focusing one (plane mirror dimensions: 1273 mm x 900 mm), so in this phase, to control the overall dimensions, it can be replaced by a focusing mirror.
As visible in fig. 7.39, it is important that the central direction of the beams (cylinder axis) is coincident with the axis passing for the mirror centre, and that the distance between two mirrors centres is vertical.
The support base will be fixed to the central flange. The point of fixing depends on the overall dimensions of the mirror in case of rotation, to avoid interferences with the enclosure.

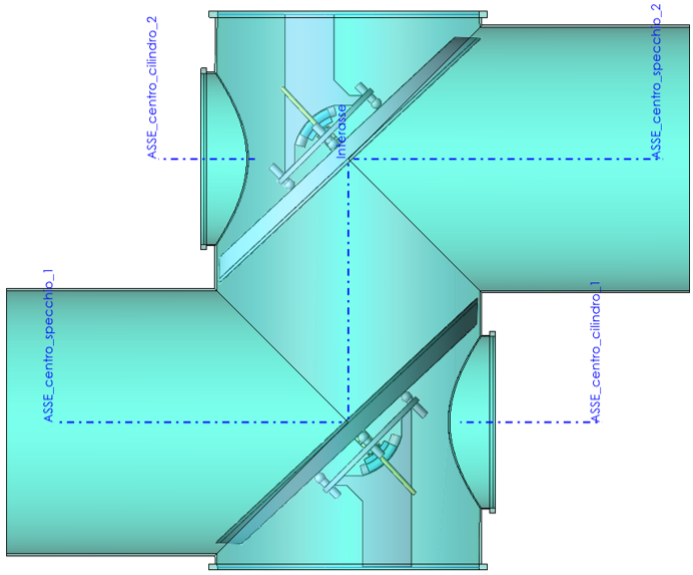

Figure 7.39: *Part of enclosure with two mirrors inside.*

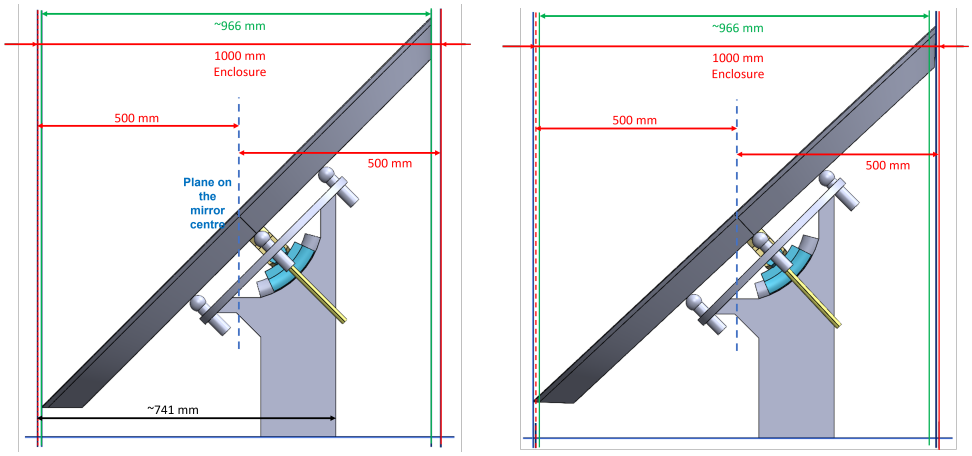

Figure 7.40: *(Left) Mirror in nominal position (45°), (Right) Mirror rotated of +2° around y local axis. View on x-z plane.*

In fig. 7.40 it is possible to observe the overall dimensions of the mirror inside the enclosure, both for nominal position (fig. 7.40 left) and for the position in which the mirror, rotated of +2 deg around y local axis, takes the largest place (fig. 7.40 right). The green lines represent the mirror dimension in nominal position, the red lines the walls of the enclosure and

the blue lines the edges of the extremal position.
Setting the mirror centre (front face) exactly at the middle of the enclosure (0.5 m of distance between the enclosure and the mirror centre), it is possible to establish the angular range for the rotation. In case of a rotation of +2 deg (fig. 7.40 right), the margin between the mirror and the enclosure is $\sim 7\ mm$ on the right side, but at the same time on the left side the mirror exceeds the enclosure dimension of 6.4 mm. The exceeding of the left limit doesn't represent a problem, because in this part the enclosure is open (reference to the fig. 7.39 bottom mirror).
It is important to remember that during the assembly and dismantling of the mirrors inside the enclosure, they must be in nominal position to avoid interferences with the structure.

To guarantee a minimum margin on the right side of 2 mm, the maximum angle of rotation is 2.6 deg, in this case on the left side the mirror exceeds the enclosure of 11.2 mm. Tab. 7.1 shows the margins on the right and left sides for different angles of rotation.

Table 7.1: *Margins on the sides with different rotations.*

Angle [Deg]	**Margin right side**	**Margin left side**
2.7	1.25 mm	12.0 mm
2.8	0.44 mm	12.7 mm
2.9	Exceeds the enclosure	-

However, the first specific to have to 2 deg of rotation of the mirror, coming from the study on the line, is guaranteed with the presented configuration. This kind of enclosure, with commercial flanges guarantees a good flexibility to the system with the possibility to increase the rotation range of 0.8 deg. In case of future needs (more space for mounting, dismantling, diagnostics), it will be worth considering a larger enclosure, at the cost of less standard components.
The natural consequence of the positioning of the mirror in the middle of the enclosure is that the distance between the enclosure and the right face of the base is $\sim 741\ mm$ (fig. 7.40 left).

7.6 Preliminary thermo-structural analyses of the parabolic mirror

After the mechanical design with the realization of the preliminary CAD model of the mirror and the supporting structure, preliminary thermo-structural analyses of the mirror have been carried out, considering one of the supporting structures proposed: support with a spherical joint.
A thermal analysis has been executed, calculating the distribution of the temperature of the mirror under specific cooling conditions and thermal loads. Then, a structural analysis has been carried out considering the thermal condition obtained before. The main result is the reconstruction of the deformed focusing surface of the mirror, which can be analysed to study the behaviour of the beams' reflection in condition of non-idealities of the transmission line.

7.6.1 FEM Model

The thermal simulations were performed with the ANSYS suite, using the FEM tools exposed in section 3.1. The assumptions about the convection and the heat transfer model are the same as in section 3.2.
A preliminary mesh sensitivity analysis has been carried out. Linear tetrahedrons are the elements chosen for the mesh of this complex structure. To reduce the time of calculation, only two different meshes were compared in a steady-state thermal analysis, in which the first one is very fine with 5'856'514 elements and the second one more coarse with a reduction of 53% of elements, 2'707'095 in total. The maximum temperatures on the mirror, calculated with the two different meshes, have a percentual discrepancy lower than 1%. For this reason, the more coarse mesh has been chosen for the analyses (fig. 7.41).

7.6.2 Thermal Load

The activity of this kind of mirror is related to the radiofrequency (RF) pulse. DEMO, with pulses of 2h, practically works in a steady state, so the reflection of the microwave beams can be assumed continuous. The RF load is always on, and the multi-beam mirror must reflect on its surface 9 simultaneous beams.
Being inside a vacuum envelope, far from the plasma, the only load that

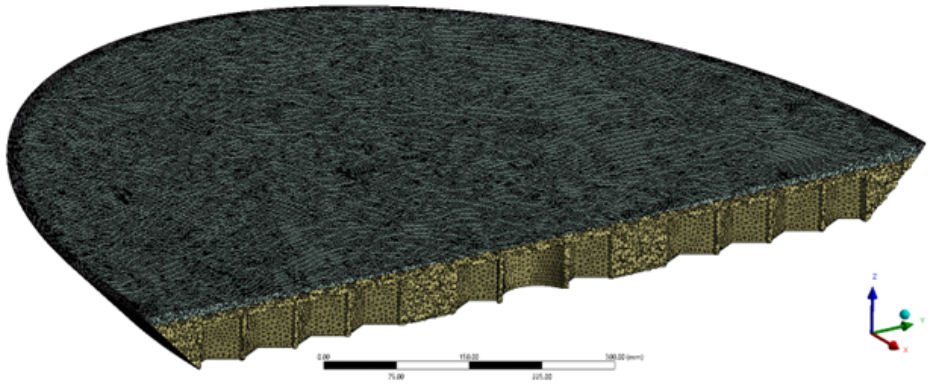

Figure 7.41: *View of the mesh of a section of the mirror.*

hits the mirror is the absorbed fraction of the microwave beams' power. As in DTT the thermal load is defined considering Gaussian distribution, having similar TL design solution, based on quasi-optical Gaussian beam propagation.
The absorbed power density per single beam is calculated as reported in section 3.3, in which, in this case:

- Q = 2 MW
- $w_x = 133.2\ mm$ and $w_y = 94.2\ mm$
- A=0.116%, evaluated under the following assumptions: gyrotron frequency of 204 GHz, perpendicular polarization (H-plane), and a roughness factor of 1.3, considering copper as the material of reflection.

Overall, the microwave absorbed power is 20.9 kW. The images in fig. 7.42 show the representation of the absorbed power as a function of the coordinates x and y.

7.6.3 Steady-state thermal analysis

The thermal input is the thermal load as described in the previous section. Concerning the cooling parameters, there isn't a cooling line yet dedicated for these mirrors, so they are assumed. They are listed below (Fig. 7.43):

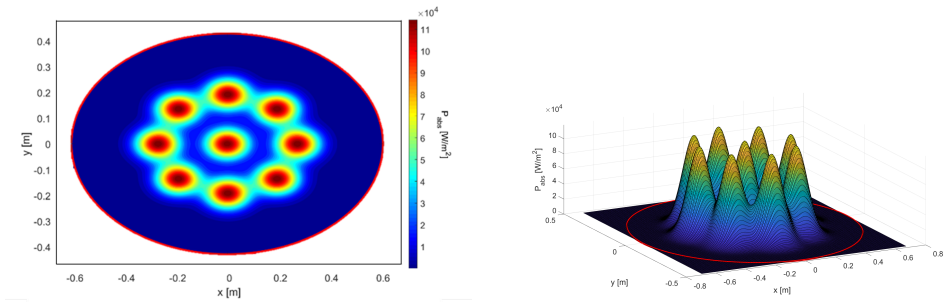

Figure 7.42: *(Left) Representation of the thermal load on the mirror. (Right) 3D representation of the Heat flux.*

- Volume flow rate: $\dot{V}_{int} = 60\ l/min$, first attempt value to guarantee a good cooling.
- Water inlet temperature $T_{water\ inlet} = 15°C$.
- Water inlet pressure: $p_{water\ inlet} = 10\ bar$ (conservative value for the pressure drops of the whole circuit).
- Heat transfer coefficient: $h_{int} \cong 47000 W/(m^2 K)$, $h_{ext} \cong 6200 W/(m^2 K)$, constant, calculated considering the water properties at $T_{water\ inlet}$.

As visible in fig. 7.44 the maximum temperature reached on the mirror is 45 °C. The hot spot is recorded in the centre, in correspondence with the central beam. In this zone, the cooling isn't so performing. Indeed, the water inlet is displaced for mechanical reasons (support structure) (fig. 7.34). This occurrence is visible also in fig. 7.45-7.46. The central beam impacts directly in the centre, the channel is far, and here there isn't a massive structure that can easily conduct heat. Undoubtedly, the reduction of the temperature recorded in the hot spot allows for more uniform temperatures and reduced deformations. It will therefore be advisable to think about alternative solutions for better cooling of the central zone, for example by exploiting a solution similar to that adopted in W7-X.

The temperature distribution on the bulk structure (fig. 7.45) is very similar to that one seen on the superior layer (fig. 7.44), both on the upper surface of the bulk and on the back of the mirror, where the honeycomb is. This trend is demonstrated also by the distribution along the thickness, as visible in fig. 7.46.

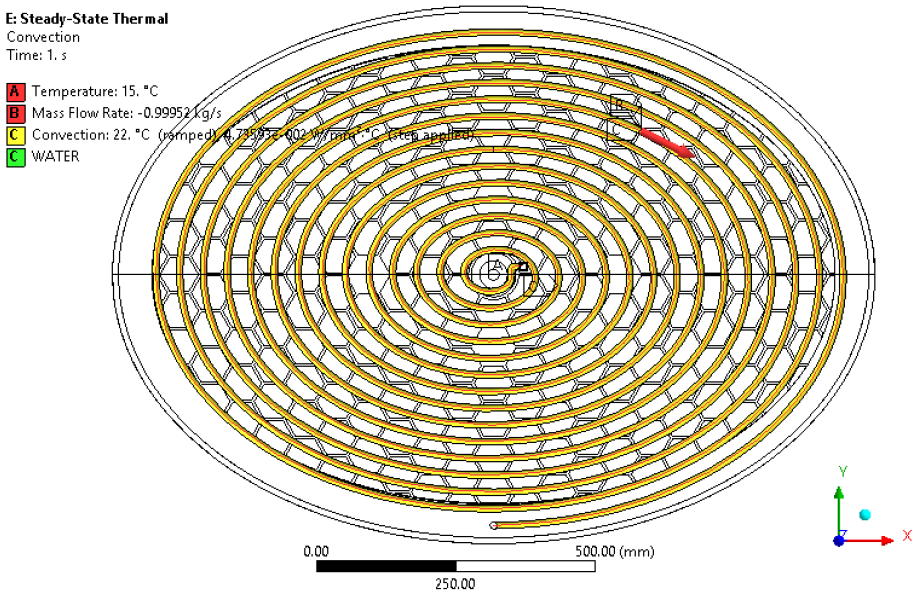

Figure 7.43: *Thermal inputs.*

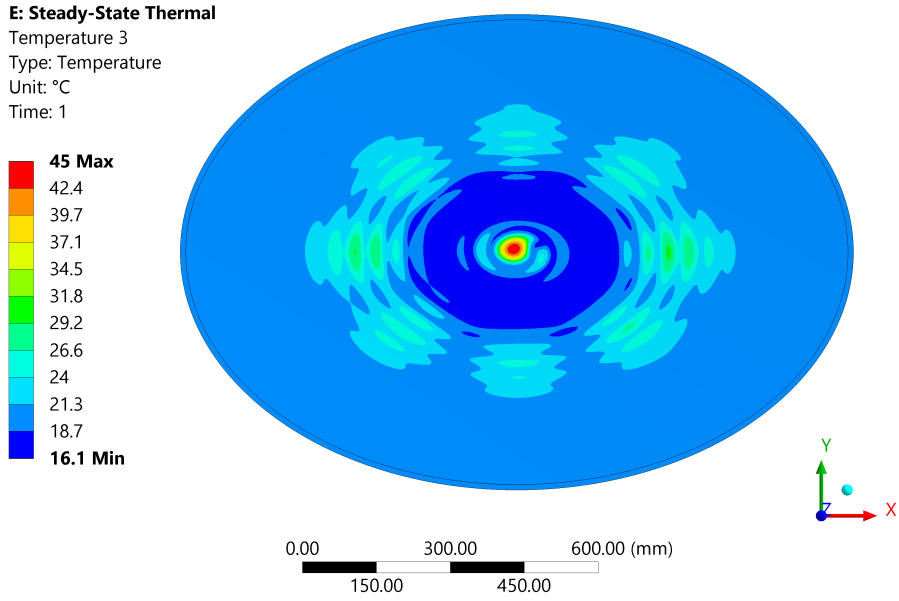

Figure 7.44: *Contour plot of the temperature on the superior layer, frontal view.*

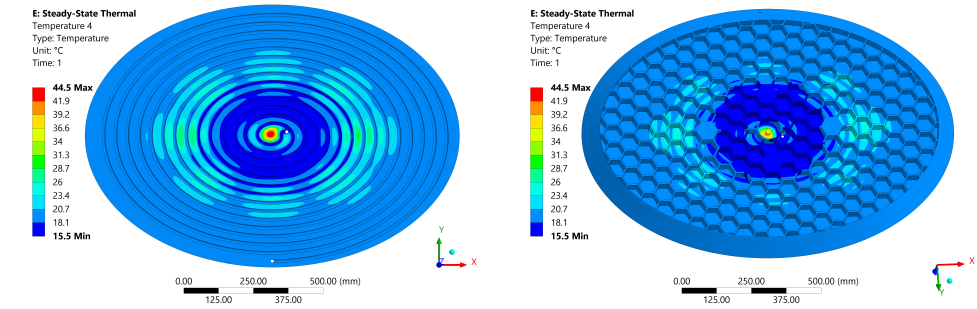

Figure 7.45: *Contour plot of the temperature on the bulk of the mirror, frontal view (left), back view (right).*

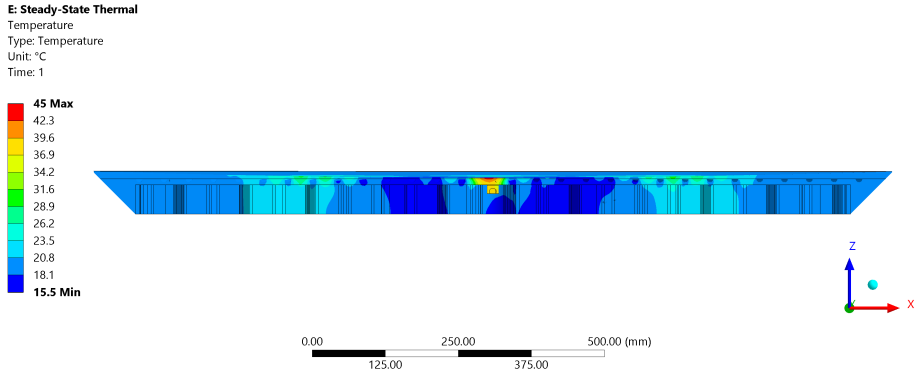

Figure 7.46: *Contour plot of the temperature on the mirror, section view.*

Another consideration concerns the water (fig. 7.47). It heats up of $\sim 5°$. The cooling works well in the central zone (around the hot spot), where the temperature of the mirror remains low, instead towards the outer edge of the mirror, the water reaches a steady condition and reaches the equilibrium with the structure. A solution with two spirals, as done for DTT, may be interesting to uniform better the temperature between the central and outer zones.

7.6.4 Transient thermal analysis

To appreciate better the thermal behaviour, a transient thermal analysis has been carried out. The time of analysis is 150 s in which the heat flux is active starting from 0.5s (not at 0s to permit the stabilization of

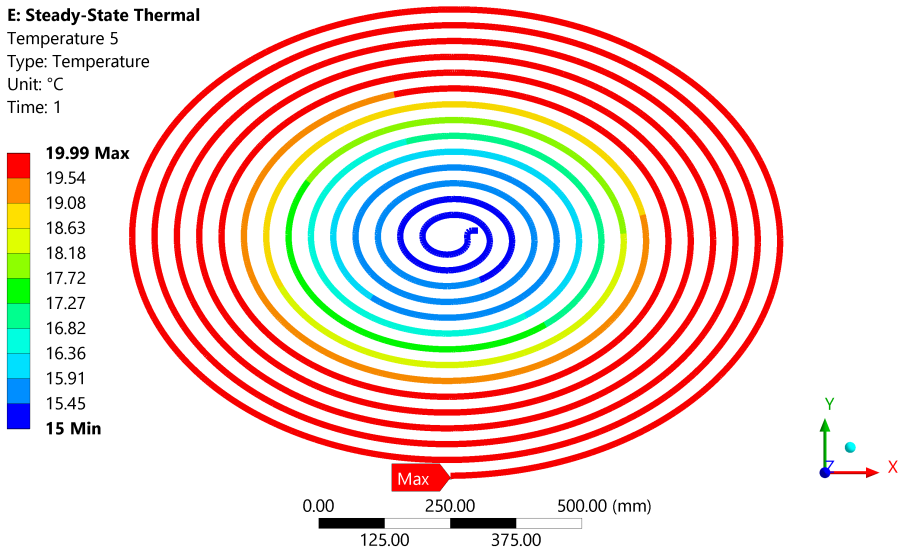

Figure 7.47: *Contour plot of the temperature of the water.*

the integration method). The time-stepping is finer in the first 20 s (Fig. 7.48). The inputs are the same as in the previous steady-state analysis. So, it is possible to describe directly the results.

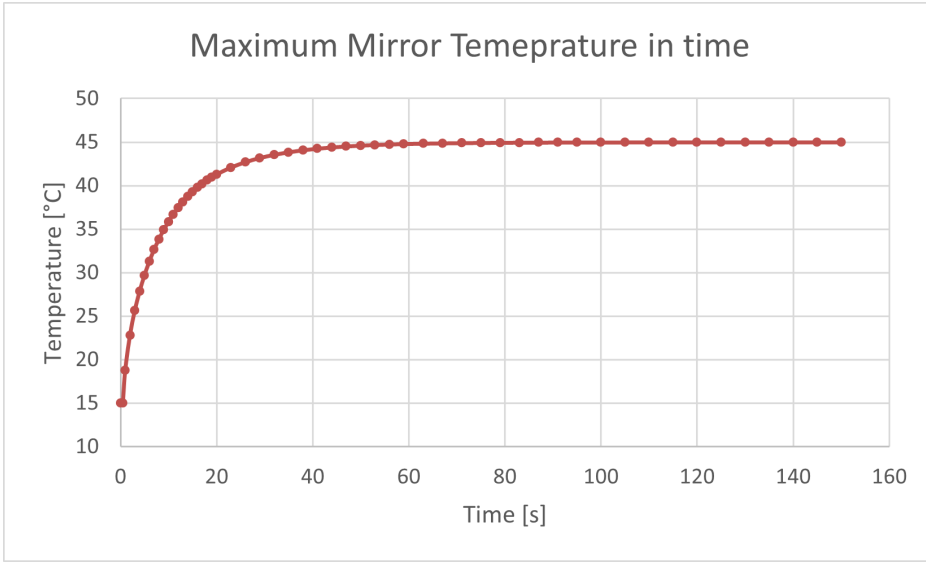

Figure 7.48: *Trend of the maximum temperature of the mirror over the time.*

The first result, visible in fig. 7.48, is that the steady condition is reached only after $\sim 40s$ of activity of the pulse. So the transient phase seems to have a short time-constant. This occurrence is visible in fig. 7.49, where is reported the contour plot of the layer at the instant of 150s. Comparing this figure with fig. 7.44, no differences can be noticed. So, at the end of the analysis, the front surface seems to reach a steady condition. But, from fig. 7.50, it is possible to appreciate that the transient phase at 150 s isn't completed. Indeed the distribution, in this case, isn't equal to that one in fig. 7.46.

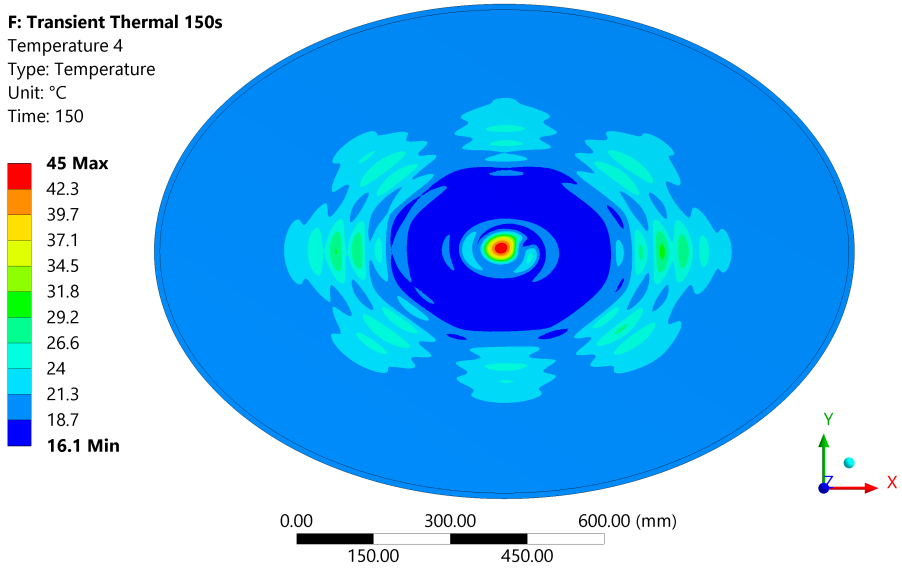

Figure 7.49: *Contour plot of the temperature on the superior layer, frontal view, at 150 s.*

However, these results show that the greatest part of the steady condition is well reached.

Regardless of the mirror temperatures, which are low in absolute value for this kind of application, thermal analysis is necessary for a more interesting structural analysis. Indeed, it is important to design the mirror in such a way as to avoid as much as possible the deformations, that affect the reflection of the beams, producing undesirable deflections. For this reason, a structural analysis has been carried out.
At this stage of the project, only a static structural analysis has been

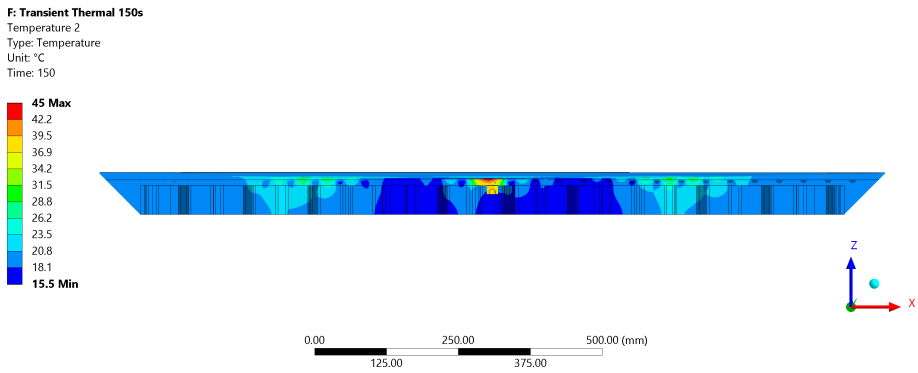

Figure 7.50: *Contour plot of the temperature on the mirror, section view, at 150s.*

performed, starting from steady-state thermal results.

7.6.5 Static structural analysis

The boundary conditions of the structural analysis are:

- Temperature distribution, resulting in thermal expansion, main cause of deformation.
- Standard Earth Gravity, considering the mirror located in the "ground" rotated of 45° respect to the horizontal (fig. 7.51 right).
- Pressure inside the channel due to water: $p_{water} = 10\ bar$ (conservatively constant).
- Forces in inlet and outlet to represent the continuity of the flow.

The support considered for this analysis is the second proposal of section 7.4.2, with the spherical joint in the centre of the back of the mirror and four spherical screws to block the rotation. The equivalent constraint used in the analysis foresees a fixed support to the back face of the pillar in which the joint will be connected. In this way the rotation around the z-axis is blocked, despite the fact that for the time being, there is no system to block this type of movement. The screws, instead, are represented by four springs in "compression-only" mode, that allow traction, but not compression in their direction (fig. 7.51). The stiffness of the equivalent springs is $k = EA/L = 1.178\ MN/mm$ only in compression mode. This

value is evaluated considering the design of the steel screw (Young's modulus E = 200 GPa), with a radius of 15 mm and a length of 120 mm. The design in this case is widely conservative.

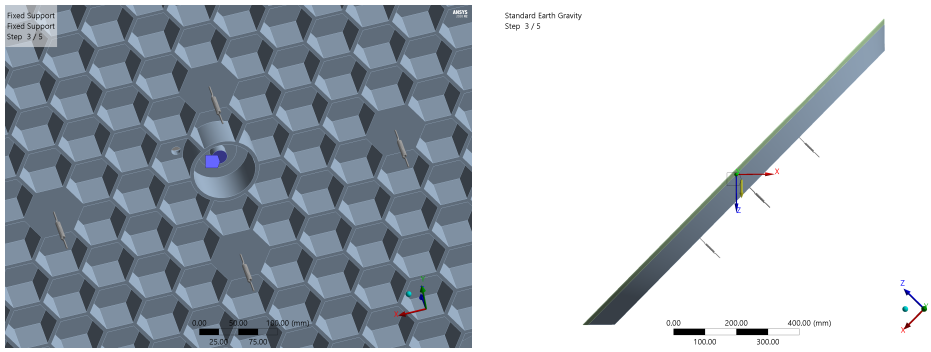

Figure 7.51: *(Left) The fixed support (in blue) and the 4 springs representing the spherical screws. (Right) Representation of the mirror subjected to Gravity (yellow arrow in the barycentre).*

The structural analysis is not trivial. In the case of usage of springs, the analysis isn't linear, so the calculations are more complex, the analysis time longer, and the convergence of each iteration more difficult.

The results show a maximum total deformation of 0.237 mm, registered at the edges of the mirror (fig. 7.52). The deformation out of the mirror plane is directed toward the negative z-axis.
In fig. 7.53 left, it is visible that the mirror is rotated. In fact, when considering the components of the total deformation (the directional deformations x, y, z), the highest results do not concern the directional deformation z. To appreciate this result, it is useful to consider only one vertex of the mirror: it is possible to evaluate the deformation of the only extreme vertex of the mirror in the x-positive direction. As can be seen from Figures 7.52-7.53, the total deformation in this region is high (red). The total deformation of the node is 0.237 mm, whose components are: 0.054 mm on x, 0.212 mm on y, and -0.092 mm on z. Thus, the high value of the total comes from the y deformation. It indicates well how the mirror is rotated. This effect is caused by the pressure within the channel. It will be important to assess, through GRASP software, whether the rotation of the mirror affects the beams more than the z-directional deformation.
Of course, further evaluations will be made to study the rotation and how

it can be avoided.

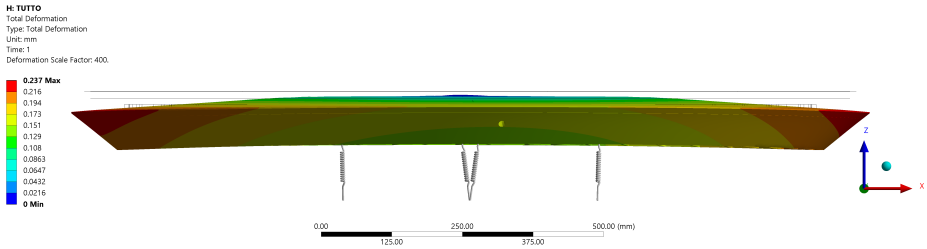

Figure 7.52: *Contour plot of the total deformation of the mirror, side-view.*

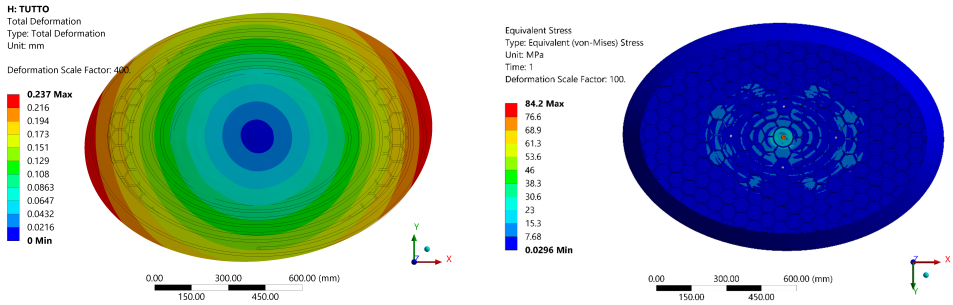

Figure 7.53: *Contour plot of the total deformation (Left) and the equivalent Stress (right) of the mirror.*

To enable the research team to study the behaviour of the beams following mirror deformation, it is necessary to extrapolate the directional deformations of each node of the reflecting surface from the structural result. With this data, it is possible to recreate the cloud of points representing the surface. An excel file was then created with the x-y-z coordinates of the nodes after deformation.
In fig. 7.53 on the right, it is visible that the maximum value of the equivalent (Von-Mises) Stress is 84.2 MPa, a value well below the yield strength limit of the steel. As foreseeable, the maximum stresses are concentrated especially in the area of fixed support.

Another consideration concerns the effect of gravity. If analysed as the only load on the mirror, the maximum total deformation is 0.019 mm, 8% of the maximum total deformation recorded before. Fig. 7.54 shows the

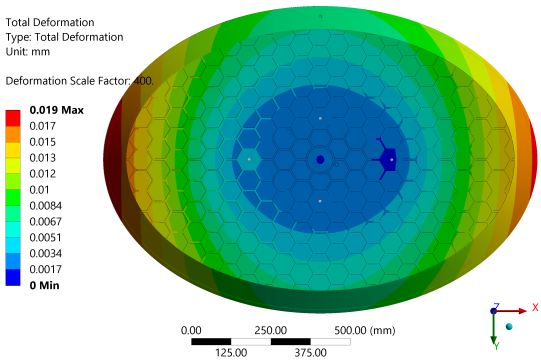

Figure 7.54: *Contour plot of the total deformation of the mirror in case of application of gravity alone.*

constraint generated by the "spring" (the screw) located in the x-positive direction, that in this configuration (only gravity) is the most loaded.

The last consideration concerns the analysis with only Temperature. In this case, the maximum total deformation is 0.089 mm, 38 % of the maximum total deformation recorded in the complete analysis.
For a clearer comparison, the graph in fig. 7.55 shows the trends of the total deformation along the major axis of the mirror for the different cases of load configurations. Pressure and force loads seem to make a major contribution to the deformation, because the discrepancy between the blue and red/purple trends is high. When comparing only the Z deformation out of the mirror plane (fig. 7.56), it can be seen that the complete and the "Temperature+Gravity" analyses produce very similar Z deformation. This result once again shows that the big difference is visible only in the total deformation that considers the x and y directional deformations. It is given by the presence of the pressure, that produces the effect of rotation, which need to be better investigated.

7.7 Summary of the work on the focusing mirror of the MBTL of DEMO

The first proposal of the focusing mirror of the MBTL of DEMO ECRH is a honeycomb-shaped bulk structure in stainless steel with a few mm solid surface dug with a spiral cooling channel, covered by a thin layer of

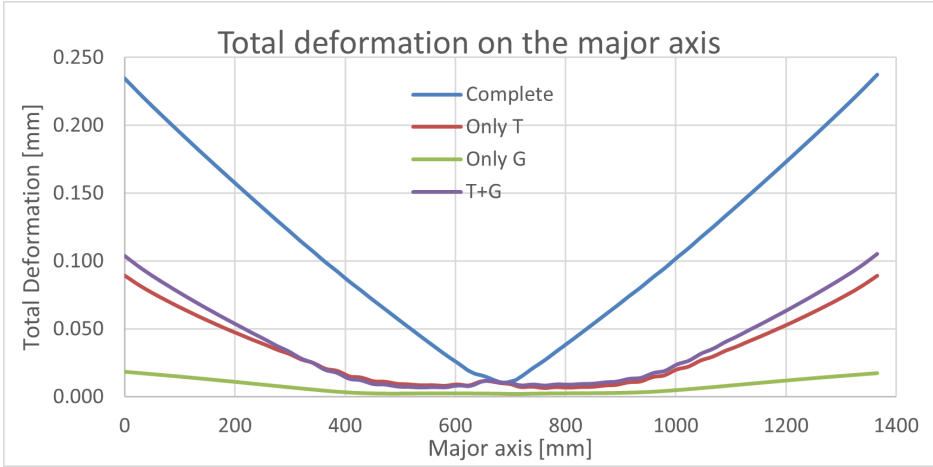

Figure 7.55: *Comparison of the total deformation trend along the major axis in different load configurations.*

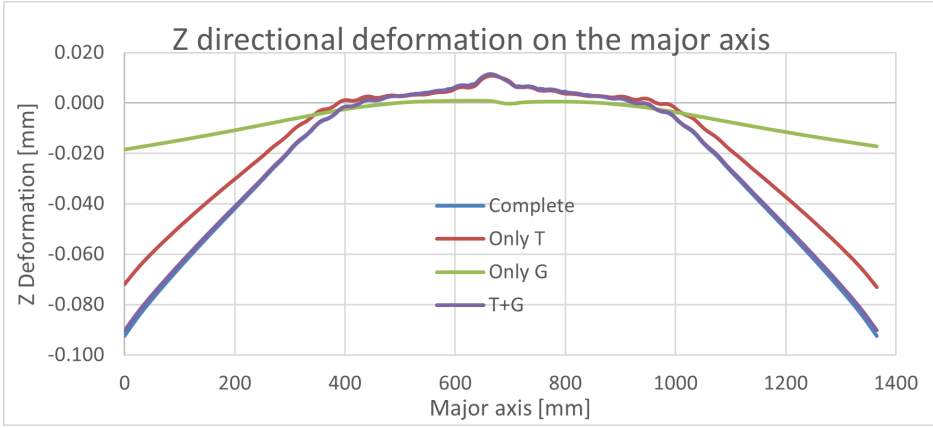

Figure 7.56: *Comparison of the Z directional deformation trend along the major axis in different load configurations.*

copper. The honeycomb choice for the back permits to reduce the weight of the mirror, maintaining a good stiffness to reduce the deformations, as preliminarily considered due to the gravity effect, and as expected when the thermal deformation effects will be considered.
Three proposals of mirror supporting structures have been proposed. Each of them is constituted by a base supporting the mirror with three different methodologies that permit its handling: two circular rails, a spherical joint or a cardan joint. Furthermore, the structure must support a plate,

in which four spherical screws regulate the handling and the alignment of the mirror.
A first conceptual design of the enclosure of a couple of mirrors has been done. Its creation brought to some adjustments of the mirror shape and the verification of the possibility to adjust the mirror position inside the enclosure within a required angular range.
Starting from the preliminary design of the mirror, considering one of the supporting structures proposed, in particular, that one with a spherical joint, different simulations have been carried out, to evaluate preliminarily the thermal and structural behaviour of the mirror subjected to microwave beam loads.
The mirror is heated by the absorbed power, a fraction of the incident power of the beams. It is cooled by a high mass flow rate of water. The centre, not well covered by the cooling and affected by the central beam reaches in the steady state a maximum temperature of 42°C. The increment of temperature leads to thermal expansion and considering also the pressure inside the channel and the gravity effect a structural simulation is executed. It shows that the maximum total deformation of the mirror is about 0.237 mm, but the deformation out of the mirror plane, in the z-direction is lower. The main contribution to the total deformation comes from the thermal load, more than the pressure and gravity. Besides, the total deformation depends a lot on the rotational effect that occurs, considering the current constraint. The first results have permitted the reconstruction of the deformed front surface. It can be analysed by the research group to study the beams' deflection and the losses of the line. However, the first results on parabolic mirror showed a necessity of improving the channel shape, above of in the centre, where the peak is recorded and also studying the effect of a double spiral. Also the structural constraints have to be improved, such as the pressure considered, in order to decrease the rotational effect occur in the deformation.

The studies herein presented are not yet reported in articles. A part of the work will be presented at IAEA 2023 conference [63]. The high variability of the DEMO requirements at this pre-conceptual stage didn't allow a significant contribution to the design, but anyway a preliminary concept of various designs was initiated, which of course can be the basis on which the system can be developed.

Chapter 8

ST40

In the field of nuclear fusion the new frontier of private companies is born. More and more private companies are investing in this field, promoting the research and new technologies. To be fast in the route of nuclear fusion, Spherical Tokamaks (STs) seem to be a good solution for studying special issues [11]. In this context Tokamak Energy Ltd, privately funded company based in the UK, was born, with the aim of developing the fusion power plant of tomorrow while commercialising the technology applications of today. The mission of TE is combining the development of spherical tokamaks with high temperature superconducting (HTS) magnets.

ST40 (fig. 8.1) is the new generation high field spherical tokamak of Tokamak Energy, now operating since January 2018 [66]. Its goal is to extend the high-field ST physics basis and test engineering solutions for future ST reactors [67].
The main parameters of ST40 are: a major radius R = 0.4–0.6 m, a plasma current of 2 MA, a toroidal field at major radius of 3 T and a pulse duration of 1-5 sec. ST40 foresees an auxiliary heating of 2-3MW from the neutral beam injection (NBI) and 2MW of the high-frequency (gyrotron-based) ECRH/EBW. A multi-frequency ECRH system is currently under development. It consists of two 105/140GHz dual

Figure 8.1: *ST40: the machine.*

frequency gyrotrons capable of up to 1 MW each
[68].
Well-established conventional ECRH and CD schemes are planned to be tested in ST40 plasma using a poloidally and toroidally steerable launcher installed at low field side (LFS) of the tokamak [69].
A high-field side (HFS) launcher is also under investigation. Implementation of a HFS launcher is very challenging, but relevant to ST reactor applications as it allows to have much higher densities compared with LFS launching [70].

8.1 ST40 HFS launcher mirror

The ECRH system is in pre-conceptual design, subjected to many changes. The little contribution, reported in the last chapter of this thesis, concerns preliminary investigation on a mirror of the vertical launcher, to have an idea of the behaviour of the mirror considering preliminary thermal load.
The vertical launcher for ST40 will be situated within the divertor region of the tokamak. This set up contains three mirrors one on the HFS the other two on the LFS. The mirror under analysis is on the HFS. It is grooved (it's a polariser) but for simplicity, for now, it has been modelled as flat.

The mirror has an elliptical shape with major radius of 69 mm and minor radius of 49 mm. Its thickness is 13.1 mm. The model was received by the TE ECRH team (fig. 8.2 left).
In the divertor region, high eddy currents may arise, investing also the mirror surfaces, therefore isolation may be necessary. In the first instance, no active cooling is assumed, and if this is insufficient, in future, it will be possible to look into potential thermal links from the mirror.
In this context, the heat exchange is characterized only by radiation and conduction inside the structure. The mirror interacts with the environment and the wall behind it (fig. 8.2 right).

The first material proposed for the mirror is Molybdenum. For the back surface a UHV compatible paint can be used, with an emissivity value of 0.8 (material provided by TE). The wall behind the mirror is

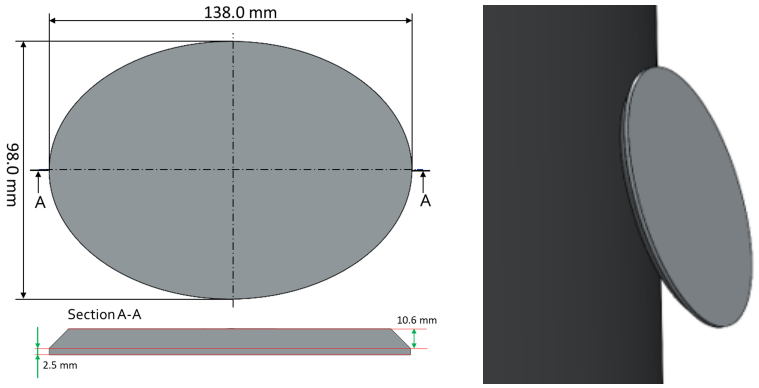

Figure 8.2: *ST40 HFS launcher mirror. On the left mirror details, on the right the mirror and the back wall.*

thought in Stainless Steel (316L (N)-IG).

In terms of the plasma thermal loads on the mirror, the worst case foresees:

- From radiation (total): $\sim 1kW/m^2$
- From neutrals particles: $\sim 40kW/m^2$

It's possible to expect these as a constant heat flux on the mirror surface for one pulse, which lasts for 1 s.
Regarding thermal load from the RF, for now, the beam is modelled as a uniform heat flux for simplicity, as opposed to Gaussian.
The power absorbed by the mirror was calculated considering molybdenum as reflective material, with an absorption coefficient of 0.177% (directly provided), beam waists $w_x = 0.038m$, $w_y = 0.027m$, a maximum power of the beam (Q) of 1 MW. The value of the absorbed power density is: $P_{abs} = 0.549131MW/m^2$. It is applied on the beam area, as shown in fig. 8.3.

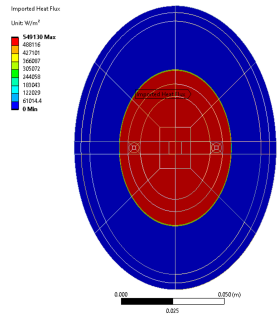

Figure 8.3: *Representation of the absorbed power density on the mirror.*

The mirror is divided in many bodies to produce a structured mesh. A mesh sensitivity analysis has been executed, compared four configurations, shown in fig. 8.4.
The results have shown the accuracy of the mesh already from the configuration 2, which has an increment of the elements of 130% with respect to mesh 1. In order to do transient simulation as fast as possible, the configuration number 2 is a good trade-off between the accuracy of the mesh and the accuracy of the time-steps.

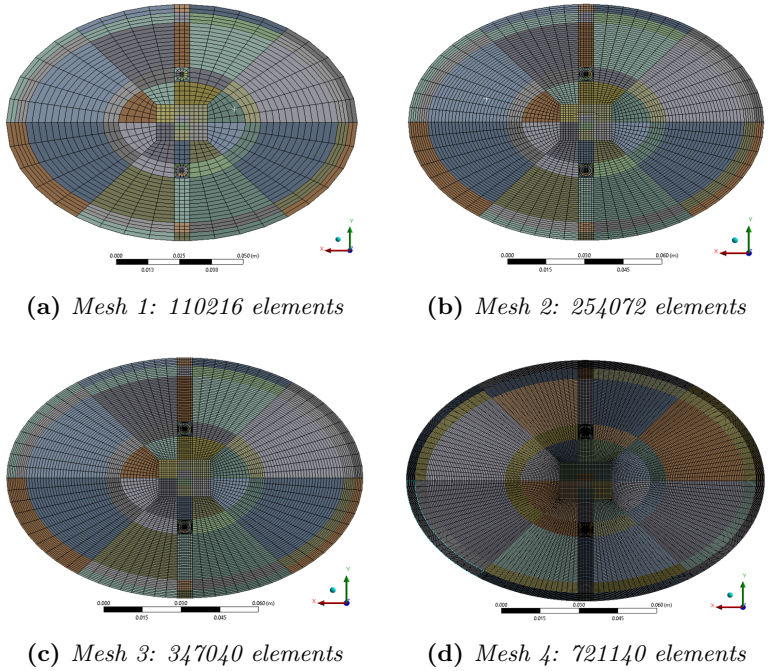

(a) *Mesh 1: 110216 elements* **(b)** *Mesh 2: 254072 elements*

(c) *Mesh 3: 347040 elements* **(d)** *Mesh 4: 721140 elements*

Figure 8.4: *Mesh sensitivity analysis for ST40 HFS launcher mirror.*

8.1.1 Transient thermal analysis

The transient thermal analysis is carried out in four stages:

1) analysis of 1 pulse in 10 s;
2) analysis of 1 pulse in 15 minutes (the time between two pulses);
3) analysis of 3 pulses;
4) analysis of 20 pulses, i.e. the activity of the ECRH over a whole day.

Thermal conditions The initial temperature is 30°C for all the structures. The thermal loads, active for 1 s, are: the heat flux of the plasma radiation ($1000 W/m^2$) all over the superior surface, the hat flux of the neutrals radiation ($40000 W/m^2$) all over the superior surface and the heat flux of the microwave beam ($0.549131 MW/m^2$) on the "beam area" of the superior surface, as in fig. 8.3.
The radiation condition is applied in two different ways. The first one is a condition active all over the time from the mirror (blue surfaces of fig.8.5 left) to the back wall and to the environment, in not-close system, in which the mirror sees the wall but also the ambient, with an emissivity value of 0.8 (of the paint) and an ambient temperature of 30°C .
The second one is a radiation condition from the wall (blue in fig. 8.5 right) to the mirror and the environment, in not-close system, with an emissivity value of the stainless steels (0.3) and the ambient temperature of 30°C .

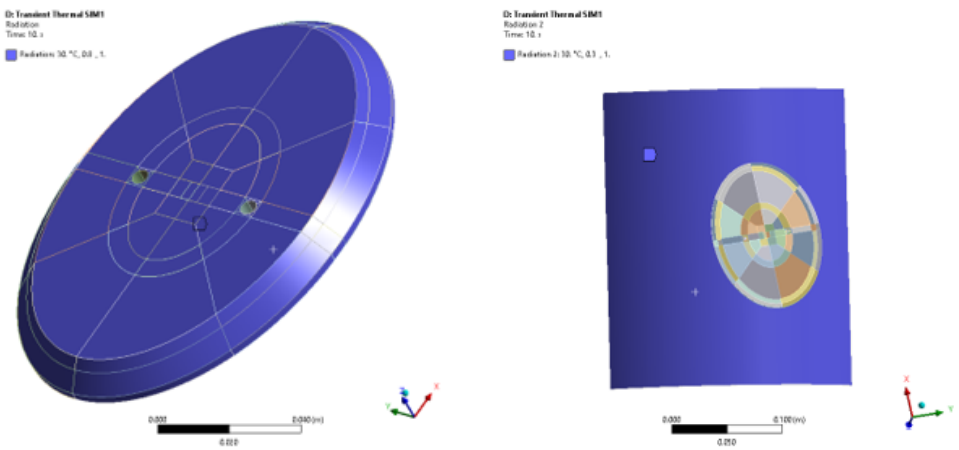

Figure 8.5: *Application of the radiation constraint.*

Time setting 1) and results The first simulation is on 10 seconds, with the activity of the pulse (thermal load) between 0.1-1.1 s (1 s total). 92 time-steps constitute the simulation: finer time-steps between 0-1.5s, coarse time-steps between 1.5-10s.

The results are visible in fig. 8.6 and in the graph of fig. 8.7. The mirror reaches $\sim 67°C$ at the end of the pulse. As visible from the contour

plot, the mirror at the edges remains cold and only the area invested by the microwave beam heats up. The maximum temperature is not so high, in this field of application, considering the absence of the active cooling. Problems can arise with the fact that, in this way, the mirror cannot reach the initial condition at the beginning of the new pulse, so the mirror temperatures always increases. In order to have an idea of this phenomenon, the second stage of analysis is presented.

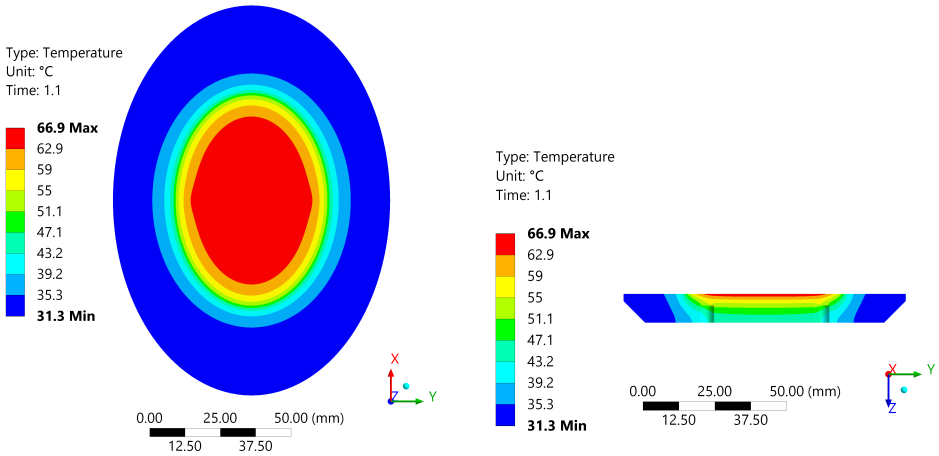

Figure 8.6: *Contour plot of the temperature distribution at the end of the pulse (1.1s). Front view (left) and section view (right).*

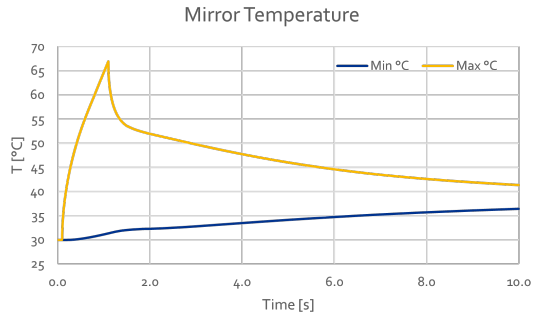

Figure 8.7: *Graph of the trends of the maximum and minimum temperature over 10 s.*

Time setting 2) and results The second simulation is on 15 minutes (900 seconds), with the activity of the pulse between 0.1-1.1 s (1 s total). 84 time-steps constitute the simulation.
The result is visible in the graph of fig. 8.8. The mirror temperature at the end of the first cycle (900 s) is 37.3°C. As expected the mirror doesn't return to initial condition (30°C), so each pulse starts with a higher initial temperature.

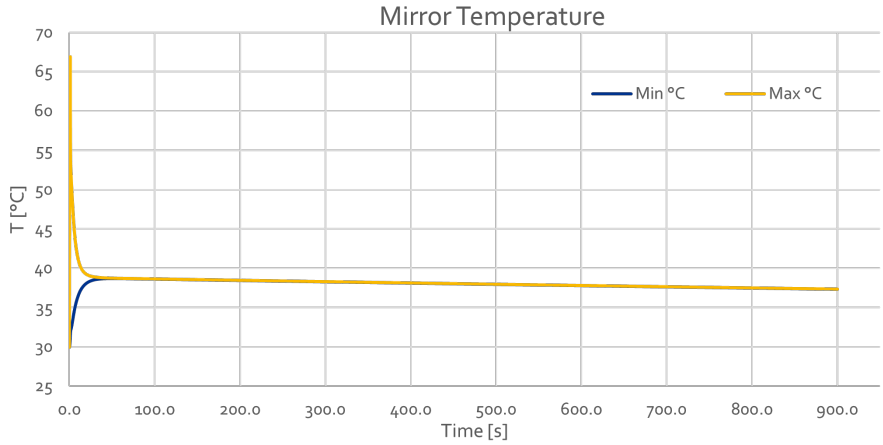

Figure 8.8: *Graph of the trends of the maximum and minimum temperature over 15 min.*

Time setting 3) and results The third simulation is on 45 minutes (2700 seconds), with the activity of 3 pulses of 1 s each. 84 time-steps constitute the simulation.
The results are visible in the graph of fig. 8.9 and in tab. 8.1. As expected the mirror increases its temperature with each pulse. The first increment is of 16°C and the second one of 13°C. Also the temperature reached at the end of a cycle (after 15 min) increases, first of 14°C and then of 10°C. Such increments seem to be decreasing, suggesting that they will tend to stabilise. With these considerations the fourth simulation was born.

Time setting 4) and results The fourth simulation is on 20 pulses (5h, i.e. 18000 seconds), 702 time-steps, finer during the pulses.
The result is visible in graph of fig. 8.10. It is visible that the increment of the peak temperature and the end-cycle temperature decreases reaching

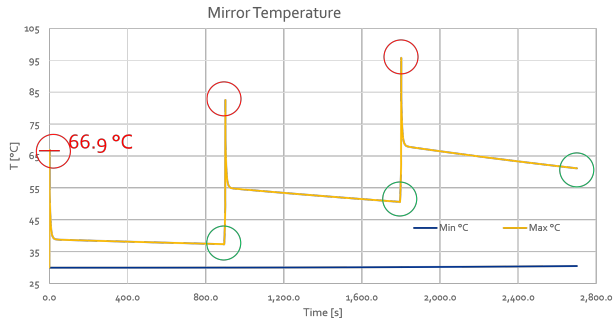

Figure 8.9: *Graph of the trends of the maximum and minimum temperature over 45 min. Red circles are for the peak temperature of each pulse. Green circles are for the maximum temperature at the end of each cycle.*

Table 8.1: *Peak and end-cycle temperatures for 3 consecutive pulses.*

Peak	T max [°C]	End	T max [°C]
1st shot	67	1st cycle	37
2nd shot	83	2nd cycle	51
3rd shot	96	3rd cycle	61

a sort of stabilization, a steady-state condition. The maximum temperature reached with the last pulse is 136.7°C. The trend of the maximum temperature per cycle is visible in fig. 8.11.

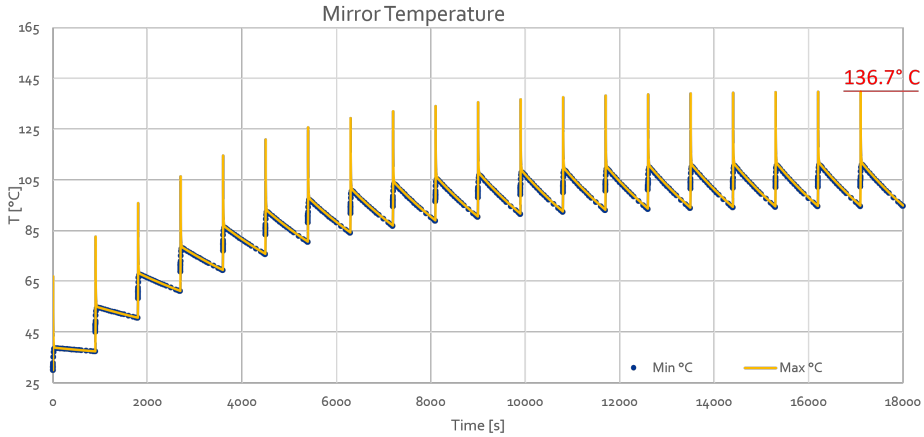

Figure 8.10: *Graph of the trends of the maximum and minimum temperature over 5h.*

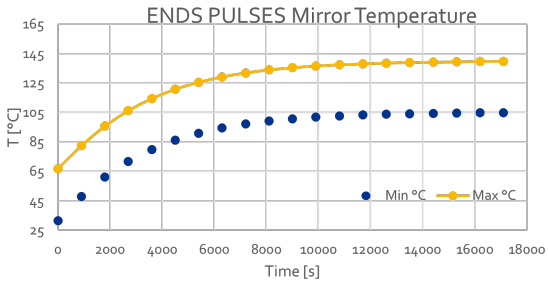

Figure 8.11: *Graph of the trend of the peak temperatures over 5h.*

8.2 Summary for the work on ST40 HFS launcher mirror

An analysis of the HFS mirror of the ST40 launcher was carried out. This was a preliminary study of a mirror subject to three types of thermal loads. Since the ECRH is under development, many simplifying assumptions were made. For example, the mirror was considered flat, even though it is a polariser, the CAD model was not optimised, it is a first design option, the microwave beam was considered constant, and the other thermal inputs are preliminary values from the physics group. Considering all the assumptions, preliminary analyses were carried out, with different timing cases, increasing the number of pulses under analysis. The mirror is not cooled, only radiation and conduction (internal inside the mirror) are active for now. Due to a very short pulse, only 1 s, the mirror does not reach high temperatures. After the first pulse, it reaches $\sim 67°C$, but without active cooling, it does not return to the initial thermal condition before the next pulse. Therefore, after each pulse the maximum temperature increases. By simulating 20 consecutive pulses, at 15-minute intervals, it is possible to see that the mirror reaches a stable condition and the peak temperature stabilises at $\sim 137°C$. This value is interesting for this type of application. Of course, the mirror needs many optimisations, starting with less approximate input data. However, this is an optimal basis that shows that with some improvements, for example some external thermal connections, the mirror can reach temperatures that guarantee the necessary structural and optical performance.

Chapter 9

Summary and conclusions

This thesis has moved into the field of Nuclear Fusion, in which, among the many challenges to overcome, one concerns the heating of the plasma to reach very high temperatures. In this context the Electron Cyclotron Resonance Heating (ECRH) plays an important role, being one of the first choices among the additional heating systems for the plasma. One of the main components of the system are the mirrors, structures for the reflection of the microwave beams. Being the reflection not perfect, a little part of the power transported by the beams is absorbed by the mirror, increasing its temperature. It leads to deformations of the mirror, causing inefficiencies in its optical performance, resulting in losses of the power at the plasma. So, it is necessary to design the mirrors preserving its optical characteristics as much as possible, reducing the temperatures and thus the deformations.

The application of already known solutions in combination with the study of the effects of alternative design choices, cooling systems, materials, geometries, adapting them to new requirements, has been the objective of this thesis, to give a contribution to the research, finding eligible solutions for the next-generation tokamaks.

The technical approach used foresees the definition of CAD models and FEM simulations, using tools based on well-known thermal and structural analyses methodologies. These analyses guided the choices and directed the study that lays the foundations for tomorrow's developments.

The study methodology has been applied to different tokamaks and mirror topologies; in the following, a summary of the main results is presented.

The most part of the application concerned DTT facility. The study started with the development of the design of the launcher mirrors M1 and M2. Such mirrors must be actively cooled, so, alternative cooling channel shapes have been proposed and compared to find the most promising solution. It resulted in a shape with elongated spiral, which well covers the whole mirror, but also the area most thermal loaded. This configuration permits to reach, in steady-state condition, a maximum temperature on M2 of 157°C. Its design became the base of the present M2 development. On the other hand, the first studies about the cooling design and the mirror temperatures as function of cooling parameters brought to definition of the mirror M1 design, that, in steady-state condition, reaches a maximum temperatures of 124°C.
These studies are reported totally or in part in the journal publications [52], [48] and [56].

Then, the methodology was extended to transient thermal and structural analyses, to be applied to MBTL mirrors, bigger than the previous ones and subjected to higher microwave load. The study started from the parabolic mirror internal to the corridor, with the generation of its CAD model and the study of different materials and different cooling system configurations. The main outcome is that a copper mirror is the best solution among the proposals and that the best channel configuration is a double spiral, with the inlet near the peak of the load and two outlets at the edges of the mirror. In this way the mirror reaches the maximum temperature of $\sim$ 55°C at the end of the pulse. Considering the temperature distribution, transient structural simulations were carried out, to estimate the maximum total deformation of the mirror, that in this case occurs $\sim$ 34 s after the pulse start, with a value of 0.177 mm.
The resulting deformed geometry at the critical instant has been verified with optical codes by DTT researchers, to study its effect on the beams' propagation. Initial results of the study about the coupling losses produced by this kind of mirror deformation are reported in article [21], but are not yet concluded.
To enable researchers to calculate the total losses due to mirror deformations, the entire line was designed, considering not just one mirror, but the complete set of mirrors in a line. Thus, flat mirrors were designed on the basis of parabolic mirrors and show higher deformations.
In addition, the thermal conditions have been improved, reducing some

conservative assumptions. Thus, more realistic constraint, showed a decrement of the maximum total deformation by $\sim 54\%$.
The final results are very interesting: the maximum temperatures for all the mirrors are in the range of (27-32)°C and the maximum total deformations at the end of the pulse is in the range of (0.065-0.100 mm). These are promising results in view of the researcher's optical verifications on the beams.
The same need to analyse losses due to mirror deformations arose for similar mirrors of DTT line, located external to the corridor. As these mirrors are smaller than the internal ones, their maximum temperatures are higher, resulting in an increment of the maximum total deformation by $\sim 26\%$.
The studies for the DTT MBTL mirrors are partially reported in the journal publication [21] and are submitted for publication [60].

The knowledge acquired with DTT mirrors has been exploited for preliminary study about DEMO focusing mirror of the transmission line. Considering a higher load, a new design was proposed, maintaining the concept of the spiral channel, but increasing the stiffness of the mirrors with a honeycomb-shaped bulk structure in stainless steel, covered by a copper layer. Preliminary thermal and structural analyses have been carried out. They showed that, cooling the mirror with high mass flow rate, it reaches in steady state condition a maximum temperature of 42°C, similar to DTT applications. But, in this case the total deformations are higher, with a maximum value of 0.237 mm. The positive aspect is that the main part of the deformation is not outside the plane of reflection, so it can have less influence on beam propagation. However, further studies are needed to improve the shape of the channel and the overall design.
The DEMO activity has covered also another technical part: a conceptual mechanical design of the mirror supporting structure and its enclosure. Three proposals of supporting structures for the handling of the mirror have been modelled and a first design of the enclosure of a couple of mirrors has been done. Its creation led to some adjustments of the mirror shape and the verification of the possibility to adjust the mirror position inside the enclosure within a required angular range.

Finally, a preliminary study of the HFS mirror of the ST40 launcher was carried out. The ECRH in this case is at a pre-conceptual stage, so

many simplifying assumptions were made. The study wanted to evaluate the behaviour of the mirror in the absence of active cooling. Due to the very short pulse duration (1 s), considering only radiation, the mirror reaches a temperature of ~ 67°C at the end of the first pulse, but before the next pulse the mirror cannot reach the initial condition again, so its temperature increases with each pulse. Simulating 20 pulses, it can be seen that the mirror reaches a stable condition and the peak temperature stabilises at ~ 137°C. Without active cooling, the mirror has a favourable condition and an optimal base from which to work out some improvements to ensure the necessary structural and optical performance.

The final designs achieved in the various applications of this thesis may not be the final solutions that will be adopted in the various tokamaks, especially since some of them are at the conceptual stage, but they will provide an important basis for improving and constructing the final mirrors that will be mounted in future tokamaks.

Bibliography

[1] H. Ritchie, M. Roser, and P. Rosado, "Energy," *Our World in Data*, 2022, https://ourworldindata.org/energy.

[2] IAEA and I. A. E. Agency, *Energy, Electricity and Nuclear Power Estimates for the Period up to 2050*, ser. Reference Data Series, 2022, no. 1.

[3] M. Ariola and A. Pironti, *Magnetic control of tokamak plasmas*, 2008, vol. 187.

[4] Unfccc, "Adoption of the paris agreement—paris agreement text english," 2015.

[5] J. P. Freidberg, *Plasma physics and fusion energy*. Cambridge university press, 2008.

[6] EUROfusion, F. Electricity, and M. Donnè, "European Research Roadmap to the Realisation of Fusion Energy," 2018.

[7] F. C. Francis, "Introduction to plasma physics and controlled fusion," 2016.

[8] ISTP and Istituto per la scienza e tecnologia dei plasmi. Fusione termonucleare. Https://www.istp.cnr.it/it/fusione-termonucleare/.

[9] F. Romanelli, *Fusion Electricity, A roadmap to the realization of fusion energy*. European Fusion Development Agreement, EFDA, Nov. 2012.

[10] EUROfusion. Realising fusion energy. Https://euro-fusion.org/.

[11] A. Sykes, A. Costley *et al.*, "Compact fusion energy based on the spherical tokamak," *Nuclear Fusion*, vol. 58, no. 1, p. 016039, 2018.

[12] T. J. Dolan, R. W. Moir, W. Manheimer, L. C. Cadwallader, and M. J. Neumann, *Magnetic fusion technology.* Springer, 2013.

[13] ITER. External heating systems. https://www.iter.org/mach/Heating.

[14] M. Tran, P. Agostinetti *et al.*, "Status and future development of heating and current drive for the eu demo," *Fusion Engineering and Design*, vol. 180, p. 113159, 2022.

[15] S. Granucci, G Ceccuzzi *et al.*, "The DTT device: System for heating," *Fusion Engineering and Design*, no. 122, p. 349–355, 2017.

[16] Max Plank Institute of Palsma Physics. Microwave heating - ecrh. Https://www.ipp.mpg.de/3871954/ECRH.

[17] F. Gandini *et al.*, "The ec h&cd transmission line for iter," *Fusion Science and Technology*, vol. 59, 2011.

[18] P. F. Goldsmith *et al.*, *Quasioptical systems*, 1998.

[19] A. Balakin *et al.*, "Quasi-optical calculations of ecrh power deposition," in *Electron Cyclotron Emission And Electron Cyclotron Resonance Heating (Ec-15).* World Scientific, 2009, pp. 383–390.

[20] Á. Fernández *et al.*, "Quasioptical transmission lines for ecrh at tj-ii stellarator," *International Journal of Infrared and Millimeter Waves*, vol. 21, pp. 1945–1957, 2000.

[21] A. Bruschi *et al.*, "Conceptual design of the dtt ecrh quasi-optical transmission line," *Fusion Engineering and Design*, vol. 113727, no. 194, 2023.

[22] S. Garavaglia *et al.*, "EU DEMO EC equatorial launcher preconceptual performance studies," *Fusion Engineering and Design*, vol. 156, p. 111594, 2020.

[23] M. Joanny *et al.*, "Thermo-mechanical analysis of ITER first mirrors and its use for the ITER equatorial visible/infrared wide angle viewing system optical design," *Review of Scientific Instruments*, vol. 83, no. 10, 2012.

[24] F. Sanchez *et al.*, "Design and manufacturing of the ITER ECRH upper launcher mirrors," *Fusion Engineering and Design*, vol. 84, no. 7-11, pp. 1702–1707, 2009.

[25] P. Santos Silva *et al.*, "Design concept and thermal-structural analysis of a high power reflective mm-wave optical mirror (M2) for the ITER ECH-UL," *Fusion Engineering and Design*, vol. 146, no. December 2018, pp. 618–621, 2019.

[26] M. Vagnoni *et al.*, "Thermo-mechanical analysis of an ITER ECH&CD Upper Launcher mirror," *Fusion Engineering and Design*, vol. 136, no. April, pp. 766–770, 2018.

[27] P. Erckmann, V Brand *et al.*, "Electron cyclotron heating for W7-X: Physics and technology," *Fusion Science and Technology*, vol. 52, pp. 291–312, 2007.

[28] W. Kasparek *et al.*, "Mirror development for the 140 ghz ecrh transmission system on the stellarator w7-x," *Fusion engineering and design*, vol. 53, no. 1-4, pp. 545–551, 2001.

[29] H. Hailer *et al.*, "Mirror development for the 140 ghz ECRH system of the stellarator W7-X," *Fusion Engineering and Design*, no. 66-68, pp. 639–644, 2003.

[30] I. ANSYS, *Workbench User's Guide*. ANSYS Europe.

[31] G. Belingardi, *Il metodo degli elementi finiti nella progettazione meccanica*. Levrotto e Bella Torino.

[32] ANSYS and Inc., *Element Reference, Release 12.1*. November 2009, Canonsburg.

[33] A. Salvitti, "Preliminary Mechanical Design and Thermal Analysis of the Electron Cyclotron Resonance Heating (ECRH): Mirrors for the Divertor Tokamak Test Facility," *Master Thesis, Università degli Studi della Tuscia*, 2019.

[34] Y. A. Cengel, *Termodinamica e trasmissione del calore*. McGraw Hill.

[35] K. Nam, W. Chung, C. H. Noh *et al.*, "Thermal analysis on detailed 3D models of ITER thermal shield," *Fusion Engineering and Design*, vol. 89, no. 7-8, pp. 1843–1847, 2014.

[36] Kasparek *et al.*, "Measurements of ohmic losses of metallic reflectors at 140 ghz using a 3-mirror resonator technique," *Int. Journal of*

Infrared and Millimeter Waves, vol. 112678, no. 22, pp. 1695–1707, 2001.

[37] R. Martone, R. Albanese, F. Crisanti, F. Martin, and A. Pizzuto, "Divertor tokamak test facility interim design report ("green book")," ENEA Internal Report, Tech. Rep., 2019.

[38] R. Albanese *et al.*, "The DTT proposal. a tokamak facility to address exhaust challenges for demo: introduction and executive summary," *Fusion Engineering and Design*, no. 122, pp. 274–288, 2017.

[39] Albanese *et al.*, "DTT: a divertor tokamak test facility for the study of the power exhaust issues in view of DEMO," *Nuclear Fusion*, vol. 57, no. 1, p. 016010, 2016.

[40] F. Crisanti *et al.*, "The divertor tokamak test facility proposal: physical requirements and reference design," *Nucl. Mater. Energy*, no. 12, p. 1330–1335, 2017.

[41] R. Albanese *et al.*, "Design review for the italian divertor tokamak test facility," *Fusion Eng. Des.*, no. 146, pp. 194–197, 2019.

[42] T. Donné and W. Morris, "European Research Roadmap to the Realisation of Fusion Energy," *EUROfusion*, September 2018.

[43] G. Federici, R. Kemp *et al.*, "Overview of EU DEMO design and R&D activities," *Fusion Engineering and Design*, vol. 89, no. 7, pp. 882 – 889, 2014.

[44] F. Crisanti, R. Martone, G. Mazzitelli, and A. Pizzuto, "The DTT device: Guidelines of the operating program," *Fusion Engineering and Design*, no. 122, p. 382–386, 2017.

[45] Enea. Divertor tokamak test facility. Https://www.dtt-project.it/.

[46] G. Granucci, S. Ceccuzzi *et al.*, "The DTT device: System for heating," *Fusion Engineering and Design*, vol. 122, pp. 349–355, 2017.

[47] P. Agostinetti, T. Bolzonella, M. Gobbin, P. Sonato, G. Spizzo, M. Vallar, and P. Vincenzi, "Conceptual design of a neutral beam heating & current drive system for DTT," *Fusion Engineering and Design*, vol. 146, pp. 441–446, 2019.

[48] S. Garavaglia *et al.*, "Progress of DTT ECRH system design," *Fusion Engineering and Design*, vol. 168, p. 112678, 2021.

[49] S. Ceccuzzi *et al.*, "Conceptual definition of an ICRF system for the italian DTT," *Fusion Engineering and Design*, vol. 146, pp. 361–364, 2019.

[50] S. Garavaglia *et al.*, "Preliminary conceptual design of the DTT EC heating system," *Fusion Engineering and Design*, vol. 146, pp. 203–206, 2019.

[51] F. Fanale *et al.*, "Progress on the conceptual design of the antennas for the DTT ECRH system," *Fusion Engineering and Design*, vol. 192, p. 113797, 2023.

[52] A. Salvitti *et al.*, "Preliminary design and thermal analyses of the steerable mirror cooling channel of the DTT ECRH," *Fusion Engineering and Design*, no. 161, p. 111880, 2020.

[53] D. Busi, "Design of an ECRH steering launcher for Divertor Tokamak Test machine," *Master Thesis, Politecnico di Milano*, 2019.

[54] NIST. Chemistry WebBook: Thermophysical Properties of Fluid Systems. Https://webbook.nist.gov/chemistry/fluid/.

[55] R. D. Larrabee, "Spectral emissivity of tungsten," *JOSA*, vol. 49, no. 6, pp. 619–625, 1959.

[56] A. Allio *et al.*, "Assessment of the performance of different cooling configurations for the launcher mirrors of the ecrh system of the dtt facility," *IEEE Transactions on Plasma Science*, vol. 50, no. 11, pp. 4054–4059, 2022.

[57] D. Busi *et al.*, "In-vessel piezoelectric actuation system for DTT ECRH launchers: Conceptual design," *Fusion Engineering and Design*, vol. 180, p. 113196, 2022.

[58] Busi *et al.*, "Study of magnetic effects on DTT ECRH front-steering mirror," *Fusion Engineering and Design*, vol. 191, p. 113550, 2023.

[59] S. Garavaglia, A. Bruschi *et al.*, "Development of the multi-beam transmission line for dtt ecrh system," in *EPJ Web of Conferences*, vol. 277. EDP Sciences, 2023, p. 04006.

[60] A. Salvitti, A. Bruschi *et al.*, "Preliminary thermal and structural analyses on the parabolic mirror of the multi-beam transmission line of the DTT ECRH system," *submitted to Fusion Engineering and Design*.

[61] G. Federici, C. Bachmann *et al.*, "Demo design activity in europe: Progress and updates," *Fusion Engineering and Design*, vol. 136, pp. 729–741, 2018.

[62] C. Bachmann, S. Ciattaglia *et al.*, "Key design integration issues addressed in the EU DEMO pre-concept design phase," *Fusion Engineering and Design*, vol. 156, p. 111595, 2020.

[63] A. Bruschi *et al.*, "Conceptual design of a modular EC system for EU-DEMO," *Synopsis for IAEA Fusion Energy conference.*, 2023, available online: https://conferences.iaea.org/event/316/contributions/27964/.

[64] G. Granucci *et al.*, "Conceptual design of the EU DEMO EC-system: main developments and R&D achievements," *Nucl. Fusion*, no. 57, p. 116009, 2017.

[65] SKF. Skf website. Https://www.skf.com/uk.

[66] M. Gryaznevich, O. Asunta, and T. E. L. Team, "Overview and status of construction of ST40," *Fusion Engineering and Design*, vol. 123, pp. 177–180, 2017.

[67] S. McNamara *et al.*, "Overview of recent results from the st40 high-field spherical tokamak," in *APS Division of Plasma Physics Meeting Abstracts*, vol. 2021, 2021, pp. UO08–011.

[68] M. Gryaznevich *et al.*, "Faster fusion: ST40, engineering, commissioning, first results," in *AIP Conference Proceedings*, vol. 2179, no. 1. AIP Publishing, 2019.

[69] V. F. Shevchenko *et al.*, "2 MW ECRH system for ST40 spherical tokamak," in *2021 46th International Conference on Infrared, Millimeter and Terahertz Waves (IRMMW-THz)*. IEEE, 2021, pp. 1–2.

[70] E. du Toit and V. Shevchenko, "Development of an electron cyclotron resonance heating and electron bernstein wave current drive system

on ST40," *Plasma Physics and Controlled Fusion*, vol. 64, no. 11, p. 115015, 2022.